5-2024

Novel designs of soft tactile sensor and robot finger manipulator based on optical fibers.

Seokyoung Han
University of Louisville

NOVEL DESIGNS OF SOFT TACTILE SENSOR AND ROBOT FINGER
MANIPULATOR BASED ON OPTICAL FIBERS

By
Seokyoung Han
B.S., Kookmin University, 2013
M.S., Gwangju Institute of Sciecne and Technology, 2015

A Dissertation
Submitted to the Faculty of the
J.B. Speed School of Engineering of the University of
Louisville
in Partial Fulfillment of the Requirements
for the Degree of

Doctor of Philosophy
in Mechanical Engineering

Department of Mechanical Engineering
University of Louisville
Louisville, Kentucky

May 2024

NOVEL DESIGNS OF SOFT TACTILE SENSOR AND ROBOT FINGER
MANIPULATOR BASED ON OPTICAL FIBERS

By

Seokyoung Han

Dissertation approved on

March 19, 2024

by the following dissertation Committee:

_____

Dissertation Director
Cindy Harnett

_____

Dan Popa

_____

Kevin Murphy

_____

Kunal Kate

_____

Yash Chitalia

DEDICATION

This thesis is dedicated to my loving family.

ACKNOWLEDGEMENTS

ABSTRACT

NOVEL DESIGNS OF SOFT TACTILE SENSOR AND ROBOT FINGER

MANIPULATOR BASED ON OPTICAL FIBERS

Seokyoung Han

March 19, 2024

Robotic manipulation is one of the main types of automated labor that humans want to achieve in order to free ourselves from mundane and hazardous tasks. The range of realizations could be very broad, from massive industrial robots to highly advanced medical devices for human healthcare. Given the critical nature of these application spaces, they require robust, safe, and most of all versatile designs. In that direction, one of the most interesting topics is the anthropomorphic robotic manipulator. Since it is inspired by human hands' function and structure, it is able to achieve the aforementioned system requirements. However, the perfect realization of the human-inspired design will take time, because there is still room for advancement in mechanical design, material, control strategy, computation performance, and more. Therefore, in this dissertation, we cover a comprehensive overview in the development of anthropomorphic robotic hand starting from subcomponents of skin, bones, tendons and nerves, and look into biological inspirations that can be implemented with the current state of technology.

Another interesting topic regarding robotic manipulation is the sensing ability of robots, which is critical to processing information in situations involving human interaction. Safety is especially vital when it comes to Human-Robot Interaction (HRI). Thus, many recent studies prioritize soft materials and highly conformable systems. Soft designs with bio-inspired aspects have intrinsic advantages in safety as well as

robustness. Therefore, integrating both manipulation and sensing within a soft design is a promising path to safe and capable automated labor.

In this work, we have developed a new type of soft tactile sensor, notably one that can detect both normal and lateral forces having 0 - 5 N range, 3 Hz sensitivity. Beyond that sensor development, an adaptive control method is demonstrated that adjusts the robotic manipulator's grasping force to counteract slipping forces on the object being handled in the real-time control manner. In contrast to most soft sensor research involving resistive or capacitive electronic sensors, here a soft optical fiber is utilized to measure the force within a soft silicone housing.

Ultimately, we developed a human-inspired robotic finger manipulator incorporating soft tactile sensing. The finger manipulator is not only sensed, but driven by a soft optical fiber tendon which is able to detect finger motion and applied force according to the physical deformation of the tendon fiber. Maximum loading force measured in this study is 3 N on the tactile tip. The final design of the manipulator has 3-joint, 4-link structure so that makes human finger-like motion($70°/70°/80°$, DIP/PIP/MCP). Through this novel design of the manipulator and sensor, we have overcome numerous technical hurdles including spatial limitation, cost-efficiency, and complexity of control, coming one step closer to realizing human-like functional robotic manipulation. Therefore, in each section the main contributions of this work can be itemized as below.

- Create a new soft tactile sensor design capable of detecting both normal force and lateral motion, including stick-slip phase.

- Introduce an adaptive grasping control system using the developed soft sensor and standard robotic grasper to prevent slipping. This controller ensures stability and robustness through analysis and implementation.

- Explore human hand anatomy extensively, focusing on structure and sensing

features, to inspire the development of robotic hands.

- Propose a human finger-inspired robotic finger design with anthropomorphic features and an optical fiber tendon.

- Utilize the optical fiber tendon for both force transmission and finger posture measurement in a single unit.

- Leverage the optical fiber to estimate finger posture and detect contact force on the fingertip by analyzing its physical deformation.

TABLE OF CONTENTS

LIST OF TABLES

CHAPTER I

DEVELOPMENT OF A NOVEL OPTOELECTRONIC

SOFT TACTILE SENSOR

1 Introduction : Human Skin and Soft Sensor

Human hands' adaptability and dexterity stem from not only the anatomical frame-
work, but also from sensory neural receptors at the skin surface and below [1]. Figure
1 shows the structure of thick (palmar side) skin, which is distinguished by the thick-
ness of the epidermis. The function of skin is not just limited to obtaining tactile
information, but to deforming around objects.

There are three layers of the skin (epidermis, dermis, hypodermis) as shown in Fig-
ure 1. Epidermis itself has low mechanical strength, yet it plays a key role to protect
underlying skin layers from abrasion. Furthermore, due to the unique ridges (fin-
gerprints) on the outer surface of the epidermis, hand manipulation exerts contact
friction that leads to a more stable grip. The dermis is the dominant underlayer
of the skin, and it determines the skin's overall mechanical properties. Because the
dermis has high elasticity and tensile strength, it serves as an absorber of external
shock along with the hypodermis. Thus, thanks to the physical properties of each
stratum, the skin helps human hands conform to objects during grasping and spring
back to their original shape by absorbing shock and elastically restoring.

Meanwhile, most of the tactile sensory receptors (mechanoreceptors) lie in between
the epidermis and dermis section to accept mechanical deformation of the skin easily,
while staying protected by surrounding layers [2]. Interestingly, many current artifi-
cial skin studies have tried to implement and exploit this human skin stratum [3–6].

1
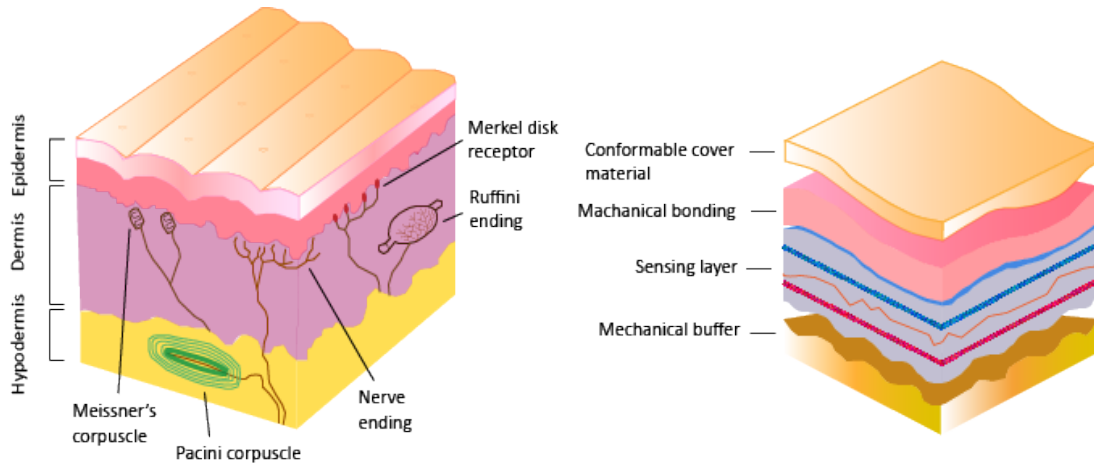
Figure 1. (Left) Illustration of human skin structure and mechanoreceptors for tactile sensing, (Right) Example of artificial skin

As mentioned earlier, human hands' dexterity comes from the interplay of frame structures, actuators, and sensory receptors. Sensor systems for measuring tactile information have been developed not only to meet demands of robotic hands, but also for other applications including medical devices and pressure mapping surfaces [6, 7]. Table 1 collects recently developed tactile sensors, focusing on those inspired by the structure of human skin. Most use soft and flexible materials so that they can conform to the objects being touched, as well as interact with external inputs within the force range of human hand manipulation tasks [5, 8–12].

While the inspiration and physical properties of various projects are aligned, Table 1 highlights distinctly different transduction mechanisms, materials, and components. The majority of soft-type sensors commonly detect changes in electrical signals, such as alterations in resistance, capacitance, or electrical charge in response to mechanical deformation [12–14]. These sensors can be seamlessly embedded onto elastomers in compact sizes, facilitating attachment to surfaces with flexible and stretchable features. While electric sensing mechanisms boast high accuracy and sensitivity, they may be susceptible to a high signal-to-noise ratio (SNR) or interference.

In contrast, optic-based sensing mechanisms are less susceptible to electrical or mag-

netic field interference and offer water resistance. Many optical sensors employ flexible optical fibers, enabling interfacing with soft-type polymers for use as skin sensors. Although these sensors are cost-effective and easy to fabricate, they may encounter issues related to optical attenuation due to ageing or analog signal calibration [15].

A more sophisticated version of optical sensors employs a vision-based sensing mechanism, exemplified by systems like TacTip [16], GelSight [17], and DIGIT [18]. In these systems, an image-capturing camera or optic-based vision sensor embedded within elastomeric material facilitates the detection of objects' shape and texture. While such systems were initially bulky, they have undergone continuous refinement in recent years. Additionally, magnetic sensing mechanisms have garnered attention, especially with the integration of magnetic particles into polymeric materials to design soft, thin, skin-type tactile sensors [19].

The main concern of these studies is obtaining normal force, detecting lateral motion, surface contact information and collecting other signals within the capability of human skin such as temperature. The skin sensor community assesses and compares projects on their force resolution, minimum and maximum measurable force, and tactile sensor element size [20].

Especially, researchers in the "soft optics" field have developed optoelectronic techniques for tactile sensing, measuring and detecting light intensity variation passing through optical lightguides [22–24]. Soft optical sensing modalities have proven a good match to bio-mimetic, innervated neural-like designs for afferent sensing. These systems deliver a photon intensity, wavelength [25, 26], or optical time-of-flight [27] signal for processing tactile inputs. Elastomeric optical fibers and waveguides have adequate transparency on the 1 m length scale and their intrinsic stretchability meets the mechanical properties of soft robotic and wearable systems. Their insusceptibility to electric interference, and their water resistance will aid with designs for environments having electromagnetic motors and strong magnetic fields that induce noise in
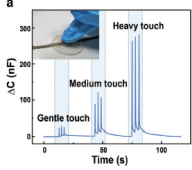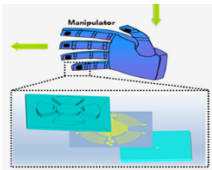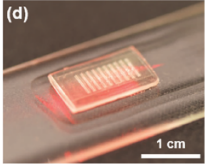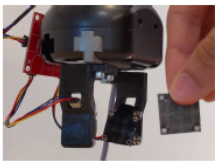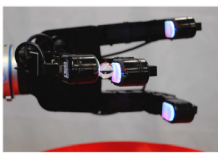
Name(Year)	Mechanism	Component	Sensitivity	Highlight
Shen(2021)	Capacitive [13]	Ionic hydrogel, Fabrics, Elastomers	$1.5kPa^{-1}$	Fast response (18ms), Materialized an array of cutaneous mechanoreceptors
Liu(2021)	Piezoelectric [14]	PDMS	$0.5N$	Pressure, roughness, sliding detection
Jiang(2021)	Optic [21]	PDMS, Resin, Optical microfiber	$0.2N$	Emulation of human fingerprint ridges, Normal and lateral motion detection
Bhirangi(2021)	Magnetic [19]	Polymer, Magnetic microparticles	$< 0.1N$	Compact, Replaceable, Compression and shear force detection
Lambeta(2020)	Vision [18]	Elastomer, plastic	640x480 (image)	High spatial resolution, Miniaturizable

Table 1. Recent skin-mimetic sensors use an array of mechanisms to produce tactile sensor elements.

electronic signals, and aqueous environments that corrode metals.

Given these advantages of the soft optical approach, groups have investigated an array of stretchable, light-transmitting materials for sensing stretching, bending, and contact forces [28–34]; recent work in this area was reviewed in [35]. Comparatively

Table 2. Comparison of soft optical lightguide sensors

Sensor type	Dynamic range	Bandwidth	Highlights	Reference
Normal force, Stick-slip phase detection	5 N (around 1 N Sensitivity)	3 Hz	Inter-fiber gap geometry leading to optical intensity changes	This study
Tactile sensor	20 N	-	Mechanics of surrounding structure causing deformation of optical path	[22]
Length sensor	Detects 1% changes	30 Hz	Time-of-Flight method	[27]
Normal force, Location	2.5 N	-	Fiber Bragg Grating in a soft structure	[26]
Normal force, Slip detection	10 N (0.2 N Sensitivity)	1 Hz	Emulating human finger skin with optical microfiber	[24]

few have used soft optics specifically to identify lateral forces or contact friction information. The general problem of slip detection for robotic object manipulation is reviewed in [36]. Researchers have used tactile sensors to obtain relative contact positions and directions, which can provide tangential forces when slip occurs, using resistive [37,38] and optical [9] transduction principles. The latter sensor is in a family of open-source TacTip optical imaging sensors [39] that rely on displacement of an array of internal, optically-contrasting pins on a soft and deformable contact surface. Other marker-array based schemes for slip and shear detection include imaging of soft contact pillars [40] or contrasting dots on a contacting elastomeric surface [41]. Motion at the edges of the marker region [41] or throughout the marker array [42] indicates incipient slip. A marker-free method, Gelsight [43], detects contact deformation by imaging the back side of a thin, side-lit elastomeric membrane touching objects and has been recently upgraded to detect slip [44]. While they are capable of high speed and resolution without complex wiring, these imaging methods require a camera view of internal gripper surfaces and are not compatible with thin robotic or

wearable sensing skins. Non-imaging approaches include dynamic tracking of wavelength changes for measuring slip along a dye-patterned waveguide [25], interrupting a waveguide path with optoelastic contact materials whose transmission properties change with shear [45], and geometric approaches that use shear-induced deformation to change the coupling of a waveguide pair, the approach we investigate in this paper. Since the soft optical sensor proposed in this paper has a simple, versatile, and cost-effective design, it is expected to outweigh the high resolution and sensitivity of other sensors for certain applications. Specifications of several similar optical-based sensors having mm range of scale are organized in Table 2. Therefore, in this work, a skin-like soft silicone sensor is presented to measure normal forces and assess the stick-slip behavior of objects contacting the silicone surface in a classifiable way through a static state test.

2   Concept of Development

The basic idea of the sensor design comes from classical frictional mechanisms and Hooke's law. Figure 2 shows how the soft silicone sensor design is inspired by a bristle model. Illustrated in Figure 2(a) through Figure 2(d), the friction surface and its parameters are based on the LuGre friction model [46–48], which represents the contact interface as flexible bristles that are deformed while lateral force is applied and an object is sticking on the surface. Since the bristles are flexible, if a soft material is designed as a finger-sized individual bristle, its deformation is likely to provide friction information relevant to stick-slip motion based on the structure's spring constant, geometry, and damping characteristics. Our finger-sized soft silicone sensor includes an optical lightguide as innervated fiber. When the silicone ridge is deformed by a lateral force, it causes an amount of lateral deformation z as shown in Figure 2(d) and Figure 2(e). In addition, since the bristle has spring behavior, one edge of the silicone structure is elongated and the other edge is squeezed while the

force is applied. This spring mechanism contains a soft optical fiber that amplifies and detects its deformation. The structure is designed with a gap that opens during deformation, making a clearance δ at the elongating edge as shown in the Figure 2(e). Because the soft optical fiber is opened by the gap while the force is applied, the light intensity is changed. Larger lateral displacements cause larger openings, increasing δ and causing a decrease in transmitted light intensity. In other words, due to the design based on the bristle friction model, this soft silicone sensor can give interpretable friction information when lateral force is exerted. This is demonstrated through static and dynamic experiments using a loading machine and robotic gripper later. We find that sensors made from different materials produce identifiable patterns that help discern the stick-slip phase from light intensity transmitted through a unique inter-fiber gap design. Also, because this sensor has a symmetric structure, it is capable of bilateral detection, which means it can measure normal pressure and slip motion changes regardless of their sign. Finally, based on its construction from easy-to-find and comparatively economical materials, we show that the fabrication process for this novel design is fast and simple (curing time 30 min and annealing time 20 - 30 min).

3 Fabrication and Mechanical Experiment

In order to implement the main design idea, an opening gap that modulates transmitted intensity in response to lateral forces, we first investigated intensity variation as a function of the distance between two separated optical fibers. As mentioned above, because the innervated fibers are closed and opened by the external force, one should expect that the light intensity can be mapped to a range of gap distances and thereby detecting lateral forces. In Figure 3(a) to Figure 3(d), one end of the fiber is connected to a red light-emitting diode (LED) while the other end is connected to a light intensity meter to measure how its brightness is changed by the external forces.
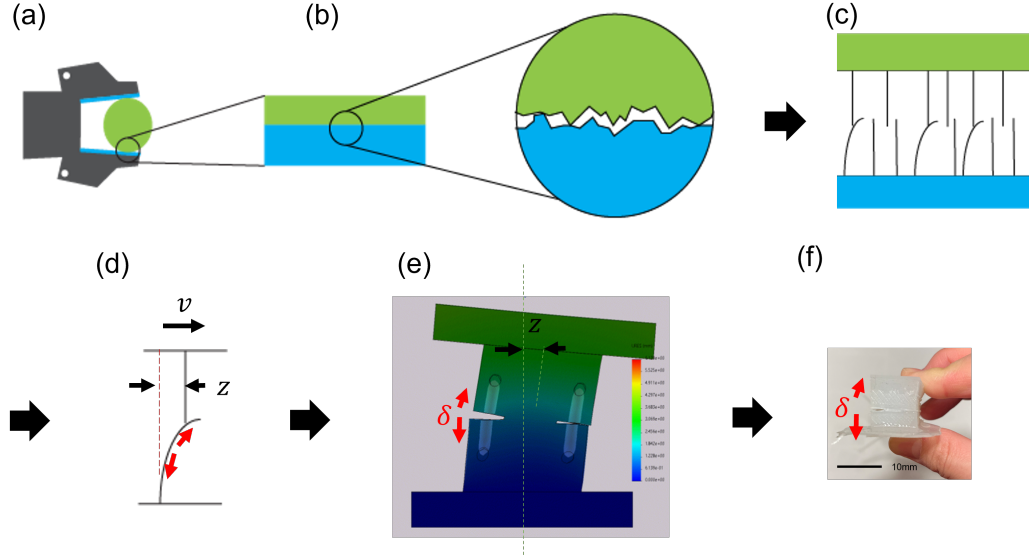
Figure 2. Development of soft tactile sensor based on bristle friction model a) Robot gripper illustration holding an object. b) Expansion view of contact surface between the object and gripper. c) Bristle model example of contact surface. d) One bristle model with deformation amount z when moving with the relative velocity v. e) SOLIDWORKS cross-sectional image of silicone sensor design stemmed from the bristle model. The feature in this design is to transform the relative deformation amount z to δ, which is the displacement between inter-fibers. Through SOLIDWORKS simulation, it is identified that 1 N normal force with 5 mm lateral motion in x-axis leads to about 2.2 mm displacement in z-axis during a stick phase. f) Finger-sized soft silicone sensor.

Also, Figure 3(e) provides the results from a ray optics simulation (COMSOL) and actual light intensity data through a photodiode receiver. Both simulation and experiment indicate that the light transmittance is diminished by increasing the distance between fiber faces. To obtain a high initial signal strength (flat part of Figure 3(e)), the design keeps the initial gap between the aligned 1.75 mm diameter fiber faces at less than 4mm. During a stick-slip event, transmission is modulated by light loss as the gap distance increases and the fiber faces become non-parallel.

The final design of the sensor is presented in Figure 4(b) and Figure 4(c). It uses clear thermoplastic poly-urethane (TPU) 3D printer filament as an optical lightguide inside of the finger-sized silicone material. As materials' information is explained in detail in the experimental section, they are both off-the-shelf products and low-
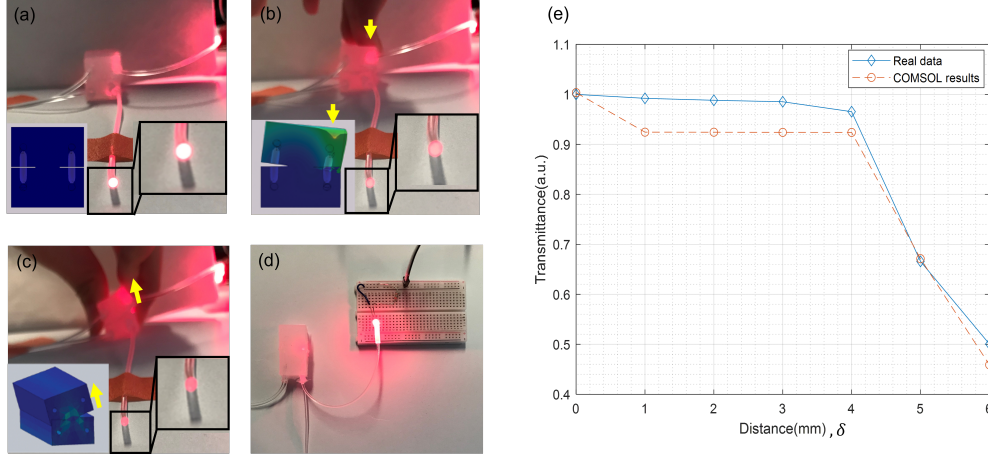
Figure 3. Red LED light intensity change with TPU lightguide according to external forces. a) Output end light intensity of TPU lightguide without external forces(Left end shows the simulation image of the silicone). b) Output intensity when pressing the silicone. c) when the silicone is tilted by hand. d) 5V red LED input. e) Transmittance rate in response to linear distance between two aligned fibers.

cost materials.(Dragon Skin 10 Very Fast, Mold Star 20T) Moreover, the fabrication process is straightforward because mold parts can be easily 3d-printed, cured, and annealed relatively fast in several minutes. Due to the simplicity of the design, it is easy to reproduce, modify and apply. This is demonstrated through the robotic gripper test showing the sensor is able to be redesigned according to the gripper's dimension.

Sensor materials determine the bristles' physical characteristics such as spring constant and damping coefficient. Before doing lateral motion experiments, we investigated the normal force case, which is directly linked to the material's softness. As seen in Figure 4(d), the ends of the optical fiber are connected to an IR emitter and photodiode receiver in order to detect deformation-induced changes in transmitted light intensity. As the loading machine compresses the silicone vertically on the left side Figure 5(a), the structure deforms the light intensity through the fiber, which decreases linearly with applied normal forces across the 1N to 5N range Figure 5(b), (c). While this linear tendency is shown in both materials (Dragon Skin 10 and Mold Star 20T), Dragon Skin 10 is chosen for further experiments since it shows wider range

9
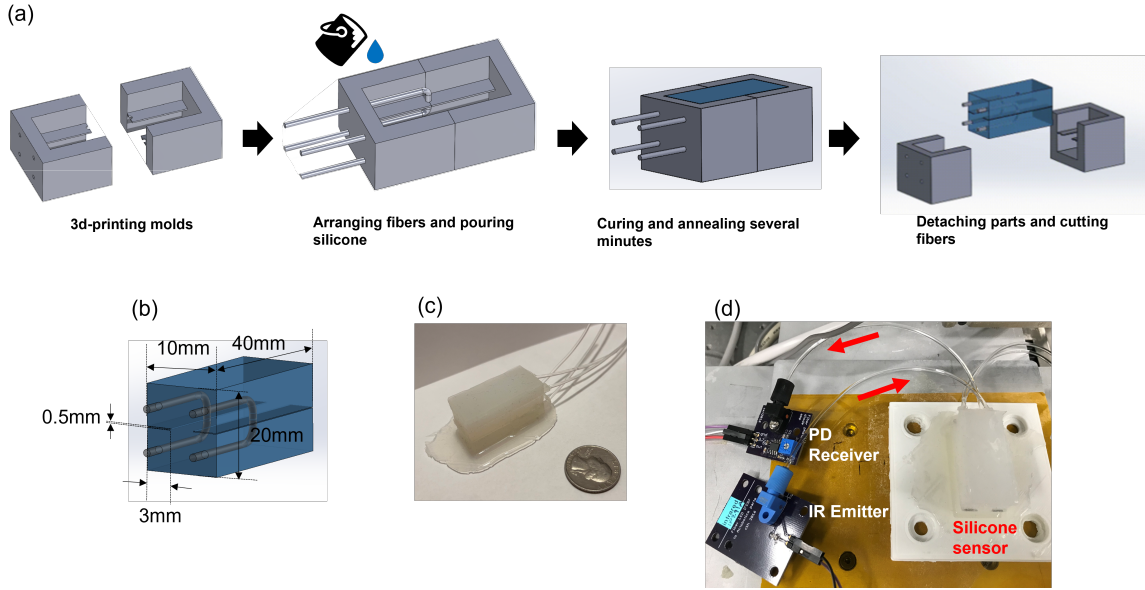
Figure 4. 3D printing and fabrication process of soft sensor. a) Silicone molding process. b) Structure design and dimensions. c) Actual size of the sensor. d) Soft silicone sensor with infrared (IR) emitter and photodiode receiver.

of output and sensitivity with respect to the normal force. Because the intended use for this sensor is in grasping control, it is important to assess its response speed, especially because the TPU and silicone materials used in this design have viscoelastic properties that lead to hysteresis. We investigated the normal force sensor's response to periodic loading and unloading in Figure 5(d) through Figure 5(f) at frequencies up to 3 Hz. The hysteresis phenomenon between loading and unloading process is shown in Figure 5(e) for 0.5 Hz. While there is hysteresis, the loading and unloading curves are reproducible and relatively linear.

After investigation of the sensor performance with respect to the normal force, the main experiment in this work is to verify stick-slip detection. The loading machine used in this test is the same as the one used in the normal force test. It can do x-axis (horizontal) movement as well as z-axis (vertical). In this initial work, we focused only on 1-D slip along the direction of maximum sensor response. Although detecting slip direction would enable more sophisticated control, 1-D slip detection is useful for preventing vise-style grippers from dropping objects vertically. Slip motion
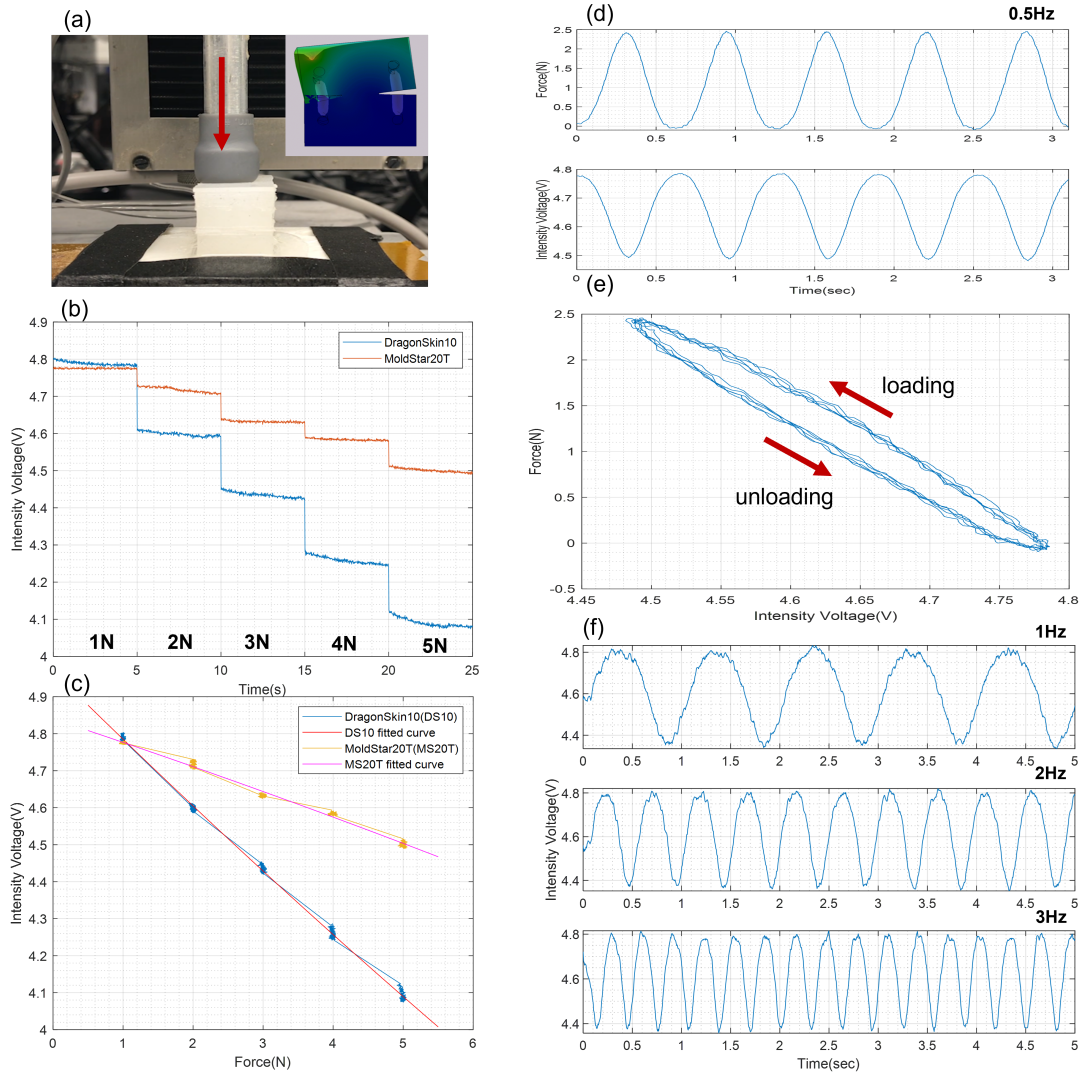
Figure 5. Physical characteristics of silicone sensor in terms of normal force. a) Loading machine setup with the silicone sensor (simulation figure on the right upper side). b) Light intensity data of two different materials(Dragon Skin 10, Mold Star 20T) according to static normal force change. c) Intensity in response to the normal force which shows a linear relation between them. Further tests are conducted with Dragon Skin 10 material, since it shows more sensitive response along the relatively wider range of intensity output. d,e) The sensor hysteresis test with 0.5 Hz sine wave normal loading. It presents relatively uniform intensity data for the loading and unloading process, with a linear intensity-vs-force relationship in the sub-5N force range. f) Sensor bandwidth results from 1 Hz to 3 Hz of sine wave.
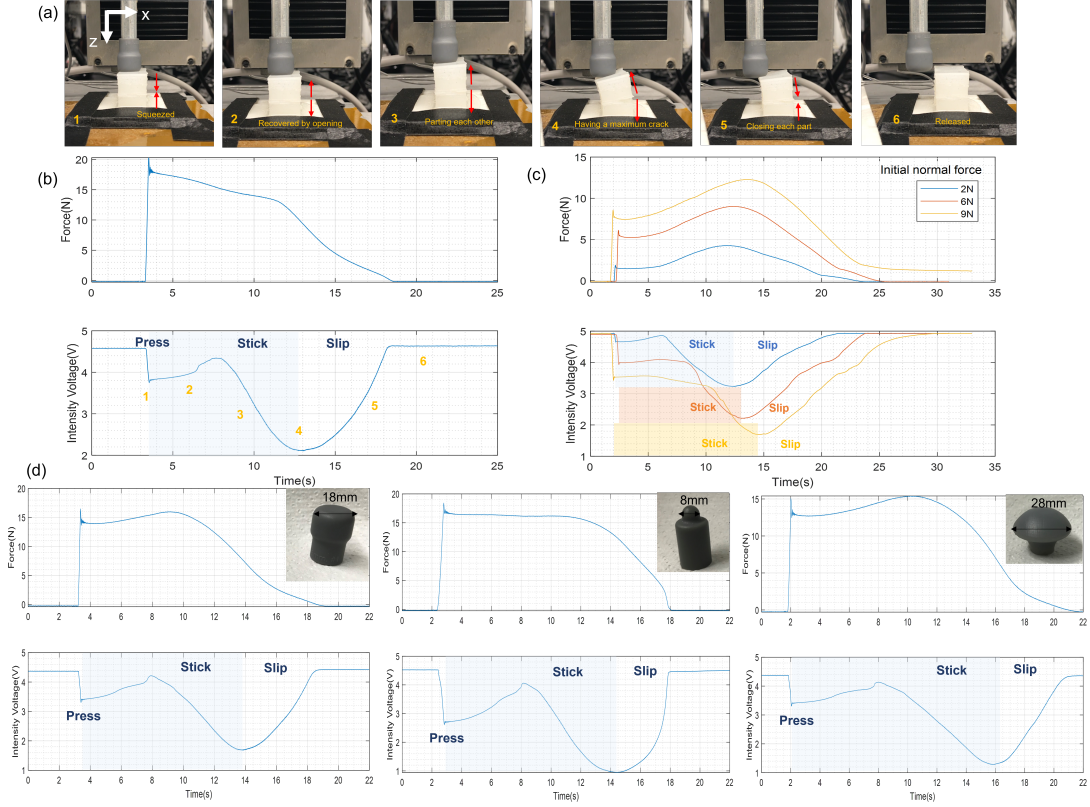
Figure 6. Stick-slip phase test. a,b) Soft silicone sensor deformation process while slipping. Each number on the photographs corresponds to the numbers on the intensity voltage data. This result is obtained from Mold Star 20T. Since it has different physical characteristics, it has different slope and duration in terms of stick-slip phase. However, it shows analogous pattern of stick-slip phase due to its mechanical design regardless of its physical properties. c) Slip performance in terms of normal force and light intensity according to different initial normal forces.(Dragon Skin 10) d) Slip motion with different indenters' shape. While contact surfaces are varied, stick-slip phase remains as a certain pattern with respect to optical intensity.

is made by pressing the silicone along the z-axis to an initial normal force, then starting a slow x-axis motion. As the silicone sensor moves along the x-axis, the light intensity changes as does the normal force data. As the sensor moves through the test procedure (Figure 6(a)) from step 1 (loading) to step 4 (maximum x-displacement without slip), the rod indenter is still stuck onto the sensor. After that, slip occurs and the measured normal force decreases to 0, which is illustrated in the procedure from step 4 to step 6. Through this experiment, two things can be verified. First, the sensor gives a recognizable pattern in terms of stick-slip phase regardless of the
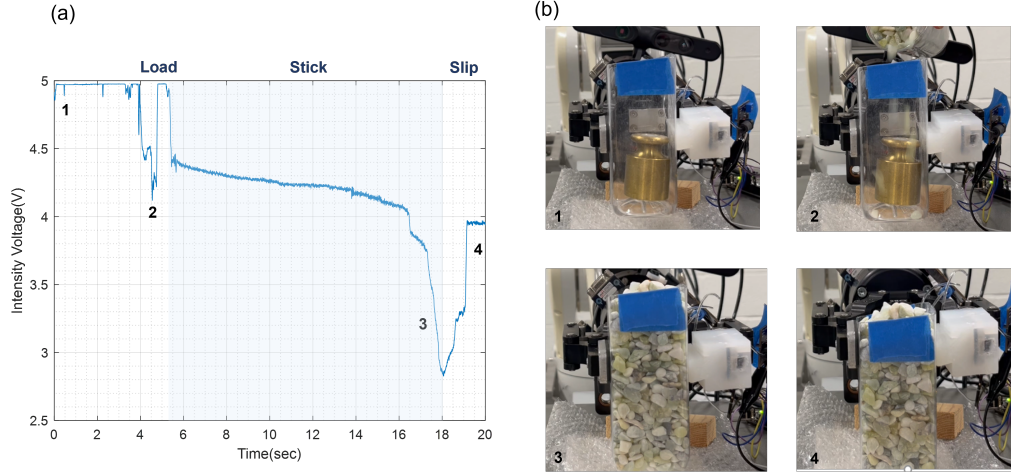
Figure 7. Intensity variation under dynamic stick-slip situation (a robotic gripper holding a container during loading with pebbles). a) Light intensity changes according to the weight of the bottle grasped by the robot gripper. The intensity data is relatively constant (no.1) until the pebbles hit the bottom of the bottle, making a transient impulse signal (no.2). Then the weight is incrementally increased by the experimenter. The intensity data shows a gradual decrease while the bottle is gripped by the sensor without slipping. At a critical weight, slip occurs and the bottle is rapidly dropped (no.3). Then the signal is restored when the object slips until the bottom touches the floor (no.4). b) Photos of stick-slip events 1 through 4. The initial weight is 300g. As pebbles are poured into to the bottle, the gripper experiences increasing lateral force until slip occurs.

type of soft materials(Figure 6(b), (c)) and indenter contact surfaces (Figure 6(d)), because of its unique bristle design with inter-fiber gap. Also, we observe that these physical differences lead to varied stick and slip phase duration and slope in the intensity signal. Second, it is identified that even if different initial normal forces are applied(Figure 6(c)), the stick-slip phase still can be discerned. Thus, the light intensity data show these characteristic and reproducible features during a stick-slip event.

The discussion around Figure 6 focused on characterizing slip motion with uniform velocity. We also investigated the sensor's response to a dynamic situation by installing it on a robotic gripper. In Figure 7(a), as well as in the lower parts of Figure 6(b), (c), (d) which are plots of transmitted intensity voltage signal vs. time during stick-slip events, one can identify a "pre-slip" condition where an object is gripped

by the silicone surface, but the intensity data slowly decreases before the object actually slips from the surface. Therefore, a simple scheme to maintain grasp control in slipping situations might be to keep the sensor signal uniform once the signal begins its slow decrease. Based on the idea, a basic compensation test is implemented to verify grasping adjustment.(Figure 8) The difference between previous and current feedback intensity data is used for error, with a goal of making the error go to zero. Since the gripper width adjustment command is the only input to the system when the signal starts to decrease (for example, between the middle and the right images in Figure 8(b)), the control scheme prevents the object from slipping.

This design was thin enough to integrate onto an existing robot gripper by sliding it over the gripper face. Further integration with multi-fingered and conformal grasping systems will bring demands for miniaturization, multiplexing, and mapping lateral forces over flexible gripper surfaces. Methods for extracting spatial information from soft and polymeric waveguide networks are not as mature as those developed for fiber Bragg gratings. However, several groups have injected spatial data into the optical signals carried by soft waveguides. These include color filtering using a stretchable dyed window to determine the location of deformations [25], time-of-flight analysis of an optical pulse traveling in a branched soft waveguide network [49] to map pressures, and image processing of signals coming from a waveguide array to classify 3D shapes of a soft actuator [50].

4   Discussion

In conclusion, this novel bristle-based design gives rise to information on normal forces and friction-driven lateral forces during a stick-slip event. The physical performance of the sensor is illustrated through the static state experiment, which shows the linear relationship between sensor output and pressure force over the 0-5 N range, and the frequency test, which shows how the sensor can respond with the maximum 3 Hz
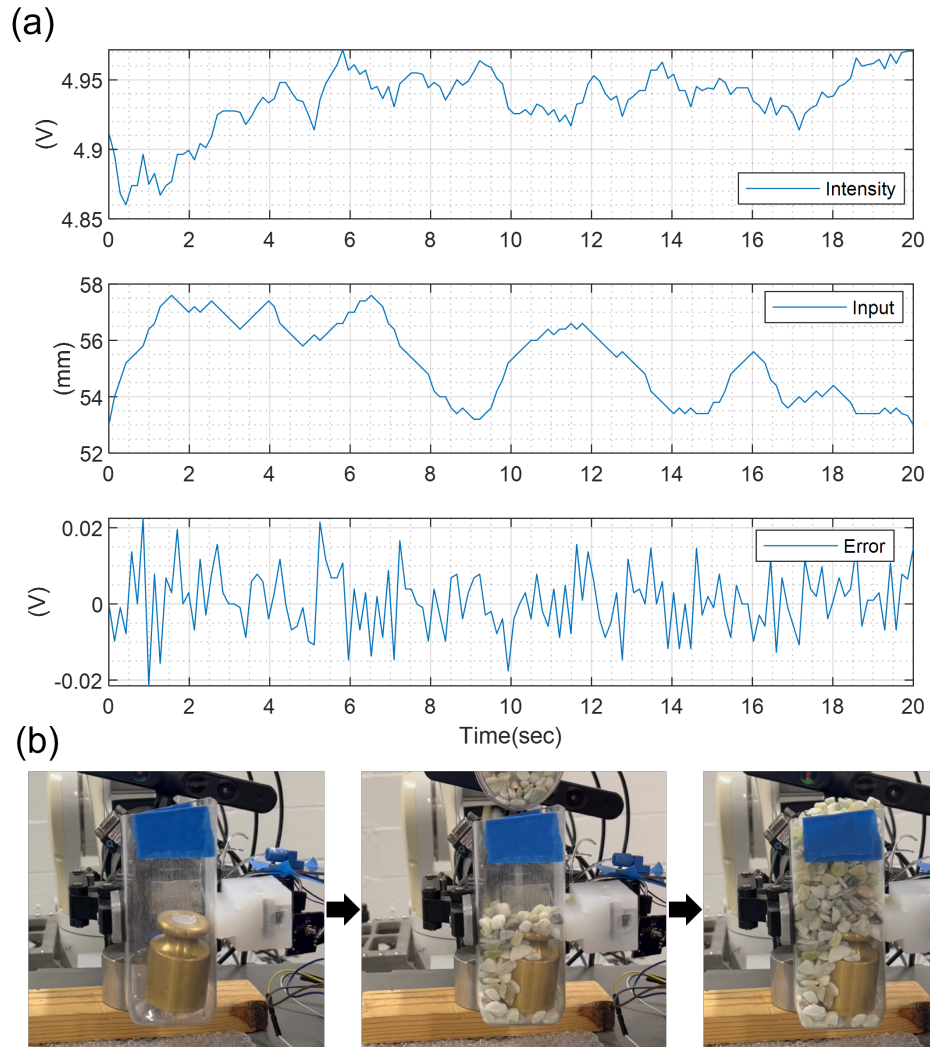
Figure 8. Compensated results based on light intensity feedback data in response to slipping amounts caused by increasing weights in the bottle. a) The intensity voltage level is maintained in a small range (0.1 V). Input command is calculated according to the difference between previous and current feedback intensity data, which is an error that stays in a small range (0.05 V). b) The gripper adjusts its grasping degree properly when slipping occurs. It shows anti-slipping by successful grasping as weight is increased.

frequency. Moreover, by collecting intensity data from the sensor during uniform slipping velocity tests, we verified that the soft sensor can provide classified stick-slip data regardless of its type of material, indenter shape, and initial normal force. Stick-slip detection without direct normal force measurement or external imaging recognition is then demonstrated through the robotic gripper experiment, where it is shown that a basic error compensation method can be applied to control the gripper separation and prevent slip in a real-time manner. Also, it is verified that the sensor can be versatile for the gripper application according to its different dimensions. Therefore, because of the straightforward fabrication method and intuitive mechanical characteristics, this novel skin-like soft silicone design is a good candidate to measure frictional information as well as normal force in grasping applications such as wearable tactile sensors for robotic grippers and human hands.

CHAPTER II

ANTI-SLIPPING ADAPTIVE GRASPING CONTROL

WITH THE SOFT TACTILE SENSOR

1 Introduction

In robotic manipulation, grasping control is still considered challenging because of
the absence of sufficient feedback, combined with uncertainties from unknown model
parameters and nonlinearities caused by deforming soft objects. If robots are to
emulate human hands, grasping must be adjusted while manipulating random objects,
all without human intervention. For these reasons, it is necessary to modulate the
degree of grasping based on high quality feedback data and using models optimized for
different situations. As mentioned in the previous chapter, since human hand contact
facilitates touching, grasping, and picking based on tactile sensory information, many
previous researches have tried to imitate humans' soft skin features to make robots
sense contact force information as well. Soft, flexible features enable hands to grasp
delicate objects and conform according to surface roughness. This is the main reason
why most of the recent works choose soft and flexible materials as tactile sensors.
[5,13,17,19,51–56] Optical sensing devices made from elastomers and highly compliant
polymer fibers also have been highlighted recently since they are soft, flexible, and
experience less electromagnetic interference, while their performance is on par with
electronic capacitor or resistor-based e-skins. [22,57] When it comes to slipping, since
the normal force is not sufficient to detect, these soft tactile sensors provide not only
normal force but also lateral force information as tactile data. [24,38] Especially, in

17

our previous work [58], a soft-type optical tactile sensor has been introduced to obtain not only grasping normal force but also lateral friction information.

Despite the good performance of tactile sensors in providing information about contact surfaces, there is still a disparity between these sensors and grasping control. The use of tactile sensor feedback has led to the proposal of strategies such as slipping detection, friction compensation, and minimum force to enable proper control of grasping degree. [59–61] Since slipping detection and minimum force grasping are directly related to knowing friction information, especially the friction coefficient, between object and tactile sensor surfaces, it is considered critical to estimate accurate friction forces and compensate proper amounts of force according to them. Moreover, robots need to perform adaptively for new situations. Different objects have different weights, textures, shapes, and some exert external forces; these features may even change rapidly during manipulation of active objects. For these reasons, researchers aim to make the system more robust to unknown parameters and uncertainties. Advanced control strategies have been presented to make robotic manipulators more flexible and responsive to new situations. [62, 63]

In this study, we demonstrate that the optical intensity variation of the soft tactile sensor data can be translated into an indication of the amount of slipping deformation. Furthermore, based on the sensor mechanical design and soft property, it is presented that the sensor adopts the LuGre friction model, which is able to calculate friction force. Therefore, it leads to control the slipping states directly unlike the other works shown that control grasping force through additional normal force feedback or complex extraction of friction force. [64, 65] Although a gripper system model with the soft sensor is suggested, still there are uncertainties and inaccuracy caused from distinction between system parameters of the model and real hardware. Secondly, we develop a model reference adaptive control(MRAC) [66, 67] system to avoid slipping with gain adaptation, which can follow reference inputs without requiring accurate

parameters information of the system.

2 Problem Statement and Modeling

2.1 Problem Statement

To implement anti-slip grasping control, the tactile information is obtained when there is lateral contact motion. The soft sensor has been created that detects changes in optical intensity based on its physical deformation. Additional information about this sensor's function can be found in [58]. In summary, this sensor gives feedback data about the external forces causing its deformation. Through experiments, it is observed that the light intensity tends to change linearly corresponding to the angle of the soft sensor. Since physical changes in the sensor can be calculated in terms of geometrical analysis, the angle variation gives a reading of the lateral movement distance of the sensor surface when an object sticks on it and experiences forces. This soft sensor is inspired by and connected to the LuGre model [68], which envisions friction originating from the lateral motion of "bristles" as lateral force is applied. This model is considered to reproduce and capture not only static situations but also dynamic friction effects such as the Stribeck effect [47]. While in many previous works, the LuGre model has shown good agreement with experimental results, still parameters estimation of the model has been discussed and control strategies have suggested overcoming unknown numbers of the system. [48,69] Thus, since the LuGre model is based on the soft elastic bristle motion, it is assumed the soft sensor in this work comply with the model as one soft body to estimate friction forces and design a proper controller for robot grasping. As for the controller in this system, because objects are random in terms of texture, shape, hardness and other features, we don't know their exact friction-relevant information in advance. This implies that the system includes unknown parameters and needs to estimate the parameters. While the MRAC requires some prior information of the system to follow ideal internal

states, it can give a good performance over a certain range of parameters.

2.2 System Modeling

As previously stated, changes in the intensity of light correspond to the level of deformation in the soft sensor. When the sensor deforms, it creates a gap in the optical waveguide, which increases the magnitude of the intensity change. In order to transform the light intensity data to the soft material's deformation amount, geometrical and empirical analyses are conducted. As shown in Figure 9, the lateral deformation amount z can be geometrically modeled so that the function of θ is simply written like (1). To obtain the empirical relationship between tilt angle and transmitted intensity, sensor data points are collected by tilting the sensor to one side. As a result, Figure 10 shows linear curve fitting with $f(\theta) = p_1\theta + p_2$, where $p_1 = -0.03871, p_2 = 1.002$ having RMSE 0.007148. It is presented that the intensity is inversely proportional to tilting angle of the sensor between 0 to 10 degree. So, now the lateral deformation amount z can be acquired from light intensity data.

$$z = \frac{l}{\theta}(1 - cos\theta) \tag{1}$$

Furthermore, it is assumed that the friction force F_c on the contact between the sensor and an object follows the LuGre model (2), which includes bristles' deformation as a system state:

$$F_c = \sigma_0 z + \sigma_1 \dot{z} + \sigma_2 v \tag{2}$$

where lateral deformation amount z is measured data and where contact stiffness, contact damping, and viscosity coefficients are σ_0, σ_1 and σ_2, respectively, and v is a relative velocity between the object and sensor.

When it comes to a gripper system equipped with the soft sensor, the model can be described as a mass(m)-spring(k)-damper(c) system like Figure 11. To simplify the system, it is assumed that the gripper moves with uniform velocity, which is a
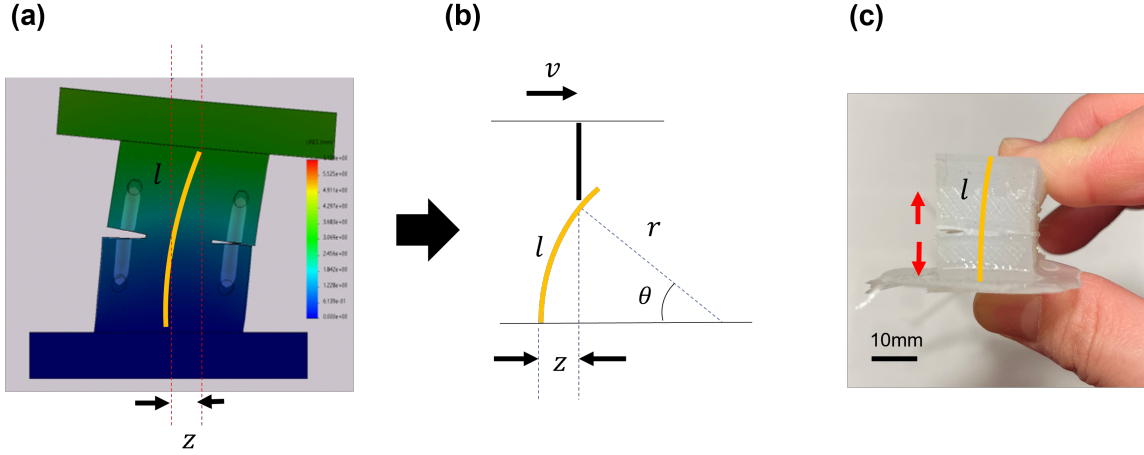
Figure 9. Simplified geometry and actual size of the soft sensor when it is tilted. (a) Solidworks motion study simulation. When the soft sensor is subjected to the lateral motion(1 N pressure 5 mm slip), it is deformed.(Colorbar shows 0-6 mm longitudinal deformation.) (b) Schematic drawing of the soft sensor design from the bristle model. (c) The actual soft sensor size.

constant. Thus, the normal force F_n can be expressed by addition of a spring term and a constant (Equation 3). Figure 11, from left to right, is a series of successive zooms showing the friction as described by the LuGre bristle model. A random object is subjected to F_n by the robot fingers, which is a function of constant α caused from the assumption of uniform gripper velocity, spring constant k, and the y-displacement. The object also experiences the slipping friction force F_c with the friction coefficient μ. When the object's gravitational force mg is bigger than the friction force, slipping occurs with the acceleration $\dot{v}$ along the z direction. As a result, the equations of motion can be written as below.

$$F_n = ky + \alpha$$
$$m\dot{v} = mg - F_c \tag{3}$$
$$F_c = \mu F_n$$

Before taking into account the state space model, several assumptions need to be considered for facilitating the controller design. As mentioned earlier, a soft sensor is supposed that keeps track of the motion of a single large bristle, with the object in

21
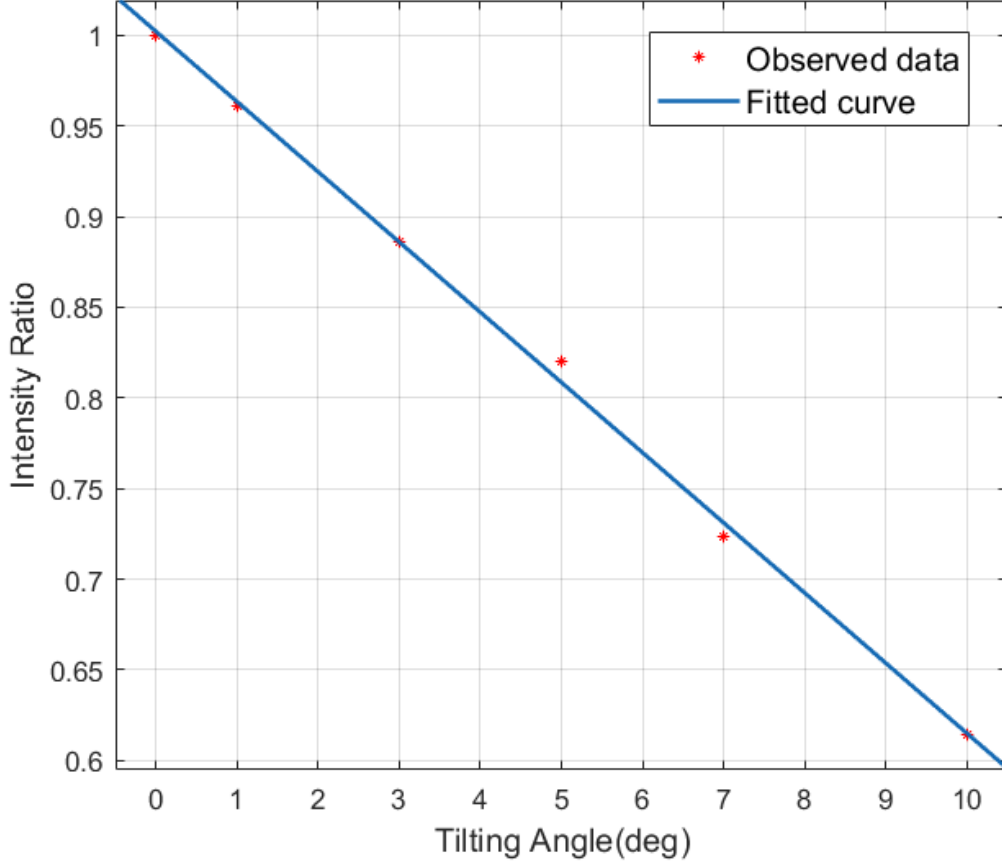
Figure 10. Linear curve fitting result based on the measured intensity data

a stiction state on top of the bristle. This assumption is feasible because the sensor is finger-sized and its material has relatively low Shore hardness (10A, DragonSkin10 from Smooth-On Inc., Macungie, PA, USA), which means it offers little resistance to indentation or torque. Basically, the object moves slowly enough for the optical sensor to track while it is sticking onto the soft surface. Consequently, this assumption leads to simplification of the system model. The relative velocity v between the object and gripper contact surface in Figure 11 can be approximated as the time derivative of the deformation amount $\dot{z}$. Therefore, the equation (2) takes the form

$$F_c = \sigma_0 z + \sigma_3 \dot{z} \tag{4}$$

where $\sigma_3 = \sigma_1 + \sigma_2$. Then, combining (3) and (4), the system dynamics simply

22
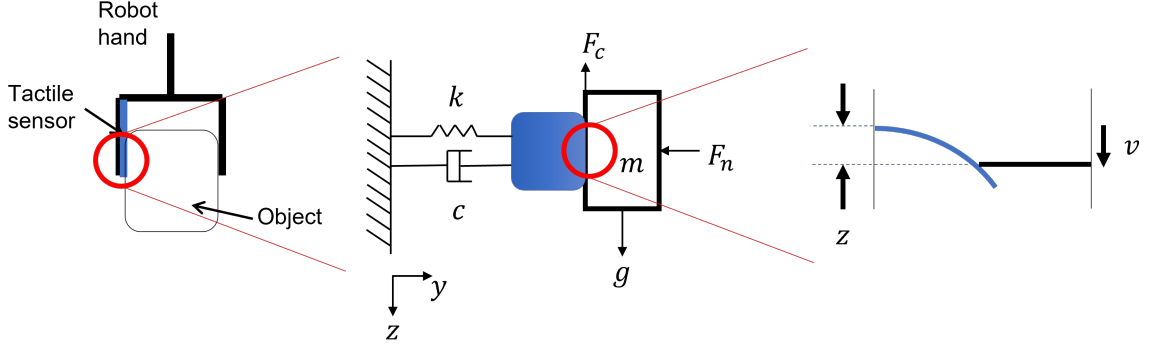
Figure 11. Free body diagram of gripper system. The soft sensor is indicated in blue. On the right side, the bristle mechanism is illustrated, representing the LuGre model of friction between the sensor and contact surface.

become

$$\dot{z} = -\frac{\sigma_0}{\sigma_3}z + \frac{\mu k}{\sigma_3}y + \frac{\mu \alpha}{\sigma_3} \tag{5}$$

3   Control Synthesis and Stability Analysis

3.1   Adaptive Control Design

Since the control objective is to avoid slip while grasping, the time derivative of soft sensor deformation $\dot{z}$ should go to zero. Furthermore, as long as system parameters are estimated properly, it is expected that grasping normal force is generated to keep the equilibrium, which is between the friction force and the lateral force. Therefore, in this section an adaptive controller is designed such that $\dot{z} \to 0$.

From the equation of motion in (5), to estimate the unknown terms according to uncertainties and disturbances, which are assumed unknown constant a, b, and Θ, it can be rewritten as a state-space representation like below.

$$\dot{x} = ax + b(u - \Theta^T) \tag{6}$$

where the system state $x := z$, the control input $u := y$, which is applied to grasping distance for the gripper system. Then, a and b stand for coefficients of z and y in (5) respectively. Also, $\Theta \in \mathbb{R}^{1 \times 1}$ denotes the constant unknown parameter to account for

$\frac{\alpha}{k}$ according to (5). This term will be accounted for by choosing the proper adaptive control law.

Unlike traditional MRAC [70], no external reference command exists in this system, because object grasping does not need to follow a reference path, in contrast to other tasks like a specific trajectory tracking. Instead, to satisfy the control objective, which is to avoid slip while grasping, an integral term of the error between the slipping velocity and zero reference input is added. Thus, the MRAC reference model is presented as

$$\dot{x}_m = a_m x_m + b_m x_I \tag{7}$$

with the reference state x_m and the additional integral state x_I. Since one of the control objectives is to eliminate slipping, which is to make $\dot{z} \to 0$, the integral term can be presented such that x_I with $\dot{x}_I = r - \dot{x}$ where $r = 0$. Based on the input error term and feedback data, in order to make the system converge, the control input can be chosen as follows:

$$u = \hat{k}_x x + \hat{k}_I x_I + \hat{\Theta} \tag{8}$$

where $\hat{k}_x, \hat{k}_I$, and $\hat{\Theta}$ are adaptive gains determined in the forthcoming stability analysis. Then, the closed-loop system dynamics of (6) can be described as below.

$$\dot{x} = (a + b\hat{k}_x)x + b\hat{k}_I x_I + b\Delta\Theta \tag{9}$$

where $\Delta\Theta = \hat{\Theta} - \Theta$. Here, the system error e is defined such that

$$e = x - x_m. \tag{10}$$

To ensure the trajectories of the system states follow the desired trajectories of the reference model, the following matching condition must be met

$$a_m = a + bk_x$$
$$b_m = bk_I \tag{11}$$

24

where the nominal ideal gain k_x and k_I can be designed using pole-placement, LQR, or other modern control methods [70] to make the $a_m < 0$ and $r - \dot{x} \to 0$.

Then now, the error dynamics can be obtained as follows:

$$\dot{e} = (a + b\hat{k}_x)x + b\hat{k}_I x_I + b\Delta\Theta$$
$$- a_m x_m - b_m x_I \tag{12}$$

Substituting the reference model, (12) can be simply rewritten as below

$$\dot{e} = a_m e + b(\Delta k_x x + \Delta k_I x_I + \Delta\Theta) \tag{13}$$

where $\Delta k_x = \hat{k}_x - k_x$, and $\Delta k_I = \hat{k}_I - k_I$.

To ensure that the error convergence to zero, a positive definite Lyapunov function is chosen as

$$V(e, \Delta k_x, \Delta k_I, \Delta\Theta) =$$
$$e^2 + b\gamma_1^{-1}\Delta k_x^2 + b\gamma_2^{-1}\Delta k_I^2 + b\gamma_3^{-1}\Delta\Theta^2 \tag{14}$$

where $\gamma_1 > 0, \gamma_2 > 0$, and $\gamma_3 > 0$.

Thus, (14) can be differentiated as follows:

$$\dot{V}(e, \Delta k_x, \Delta k_I, \Delta\Theta) =$$
$$2\dot{e}e + 2b(\gamma_1^{-1}\Delta k_x \dot{\hat{k}}_x + \gamma_2^{-1}\Delta k_I \dot{\hat{k}}_I + \gamma_3^{-1}\Delta\Theta \dot{\hat{\Theta}}). \tag{15}$$

Substituting (13) into (15), the differential of Lyapunov function is rewritten as below.

$$\dot{V} = 2a_m e^2 + 2b(\Delta k_x(ex + \gamma_1^{-1}\dot{\hat{k}}_x)$$
$$+ \Delta k_I(ex_I + \gamma_2^{-1}\dot{\hat{k}}_I) + \Delta\Theta(e + \gamma_3^{-1}\dot{\hat{\Theta}})) \tag{16}$$

Choosing

$$\dot{\hat{k}}_x = -\gamma_1 ex$$
$$\dot{\hat{k}}_I = -\gamma_2 ex_I \tag{17}$$
$$\dot{\hat{\Theta}} = -\gamma_3 e$$

Then, $\dot{V}(e, \Delta k_x, \Delta k_I, \Delta\Theta)$ becomes globally negative semi-definite

$$\dot{V}(e, \Delta k_x, \Delta k_I, \Delta\Theta) = 2a_m e^2 \tag{18}$$

Based on (14) and (18), it is shown that $V > 0$ and $\dot{V} \leq 0$, and that leads to bounded $e, \Delta k_x, \Delta k_I$, and $\Delta\Theta$. In order to make sure that the system error e converges to zero, (16) is differentiated along the trajectory of $\dot{e}$ again and presented as the below equation by substituting (17).

$$\ddot{V} = 4a_m e\dot{e} \tag{19}$$

Since $x_I, x_m \in L_\infty$, it is considered that $\dot{e} \in L_\infty$ and $e \in L_2$ resulted from (13) and (18) So, this leads to $\ddot{V} \in L_\infty$ from (19). Therefore, using Barbalat's Lemma [71], the state error e asymptotically goes to zero as $t \to \infty$.
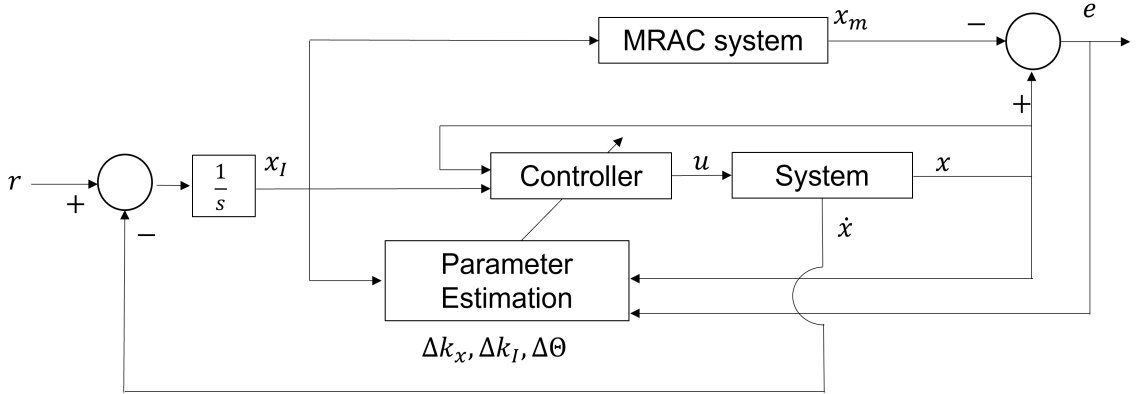
Figure 12. Adaptive control scheme with reference input error integral term

4 Results

4.1 Simulation

Before implementing the MRAC on the real hardware, a simulation is conducted in MATLAB using the analytical soft sensor model with the parameters listed in Table 3. The initial state is set to $x(0) = 0.001$, indicating a 1 mm slip distance at the gripper's start. The control objective is to make the time derivative of slipping distance $\dot{x}$ converge to zero, so the reference input is set to zero. In addition, the system should follow the reference model, as determined by stability and parameter

estimation analysis. As shown in Figure 13, the time derivative of the distance reaches zero at around 3 seconds, and the system state x tracks the reference model state x_m at the same time.

Table 3. System parameters for simulation

LuGre model parameters			
σ_0	15 N/m	σ_3	10 N·s/m
Gripper system parameters			
k	14 N/m	μ	1.5
Controller parameters			
$\hat{k}_x(0)$	-0.7619	$\hat{k}_I(0)$	1
$\hat{\Theta}(0)$	0	$\gamma_{1,2,3}$	10.5
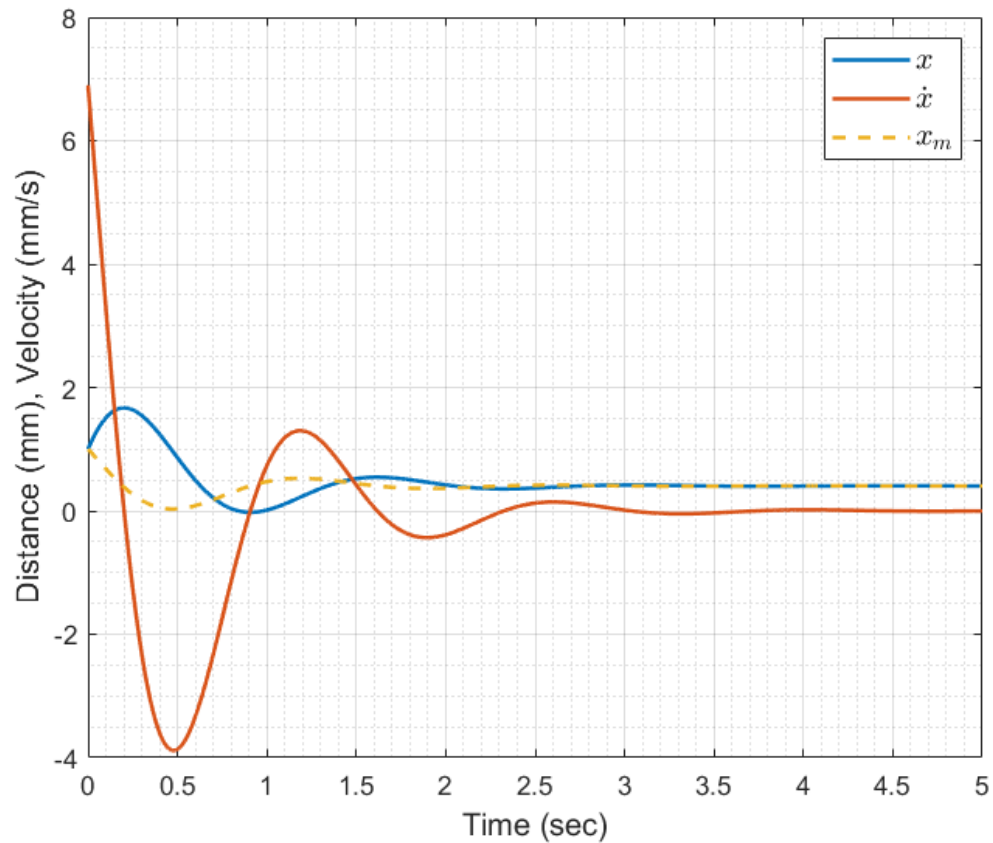
Figure 13. MRAC simulation result

4.2   Hardware Experiment

To implement the proposed control scheme, a two-finger robotic gripper (Robotiq Inc, Canada) was used, and the soft sensor was installed on one side of the gripper, as shown in Figure 14(a). The control input u was applied to regulate the gripper distance at a frequency of 6 Hz. The sensor detects changes in light intensity resulting from external input and sends a calibrated analog signal to a micro-controller board, which smooths the signal using a moving average method at a sampling rate of approximately 200 Hz before transmitting the digitized signal to a PC, as depicted in Figure 14(c). As the speed of the gripper control signal is slower than the sensor sampling rate, Python algorithm is developed to synchronize the I/O. The sensor and gripper are connected using a serial communication interface (RS-232).

Preliminary tests were carried out to observe the occurrence of slipping when holding a bottle with a non-controlled gripper, where pebbles were gradually added to increase the object's weight up to a maximum of 500g. The slipping distance increased until the bottle was dropped in the non-controlled case, as shown in Figure 16. However, the proposed MRAC (shown by the blue curve in Figure 17) demonstrated that the time derivative of the slipping distance remained near zero (between ± 0.2 mm/s) after the initial impact caused by pouring the pebbles. The orange curve represents the simple feedback compensation method, where the gripping distance is compensated by the difference between current and previous sensor feedback data when the static slipping occurs. This compensation method ensures that the gripping distance is adjusted to the slipping displacement generated, as this soft sensor can detect slipping distance. However, it cannot guarantee that the velocity will always remain zero as disturbances are added. The yellow curve represents the non-controlled gripping case, where the object slips, and in approximately 20 seconds, actual slipping occurred, leading to the object being dropped.
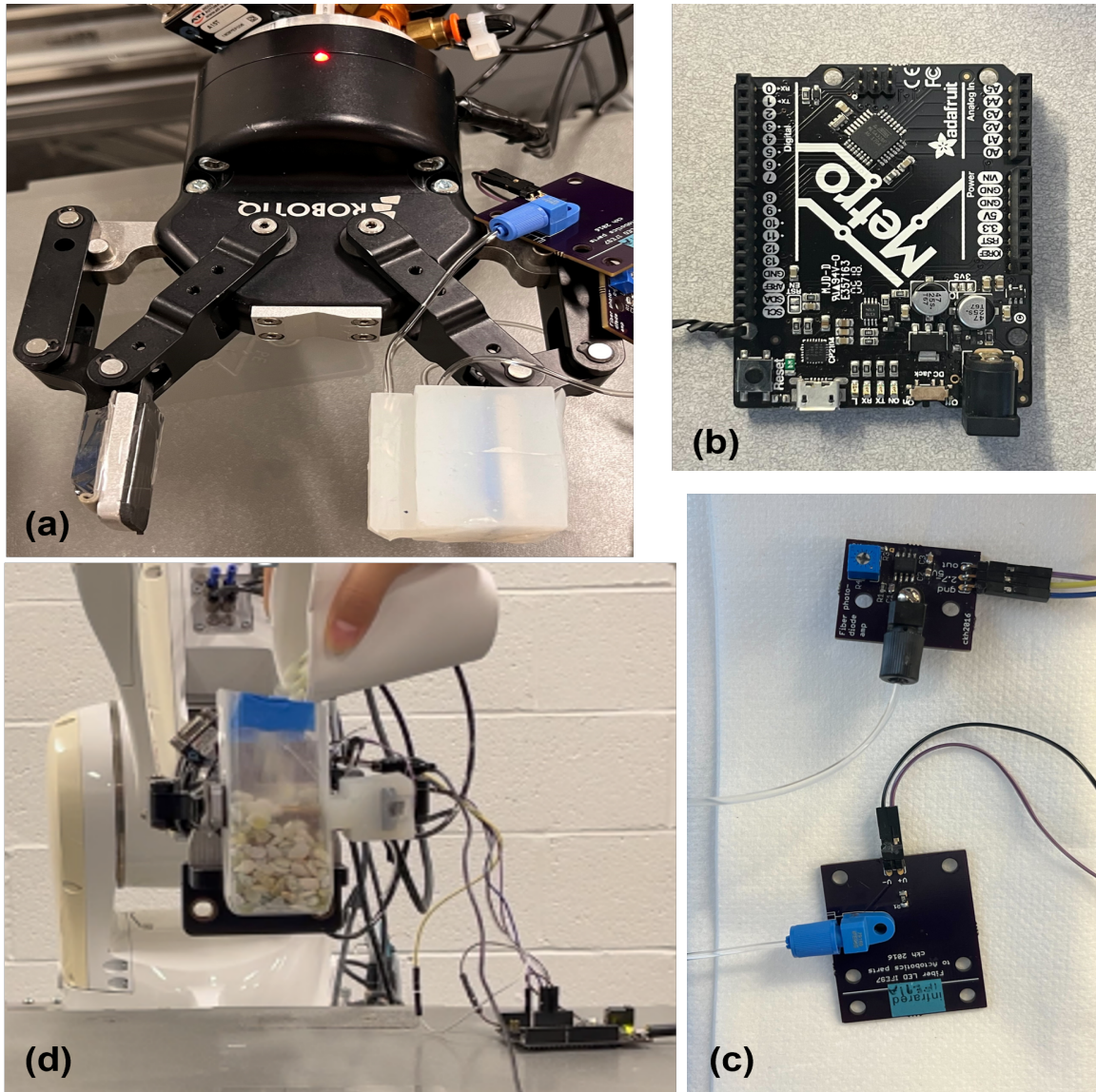
Figure 14. Hardware implementation setup (a) Soft sensor with robotic two-finger gripper (2F-85 from Robotiq Inc., Canada). (b) Light intensity analog signal comes in Adafruit Metro board and gets converted to the main PC through the serial port. (c) Photo receiver (photodiode) and emitter (950nm infrared) with TPU fiber as a lightguide. (d) Pouring pebbles into the bottle so that the object weight is increased little by little.

5 Conclusion

In conclusion, the adaptive grasping control is implemented to avoid the object slipping with a new type of soft sensor based on optical information. Especially, in simulation, it is shown that the system follows the reference model, which means
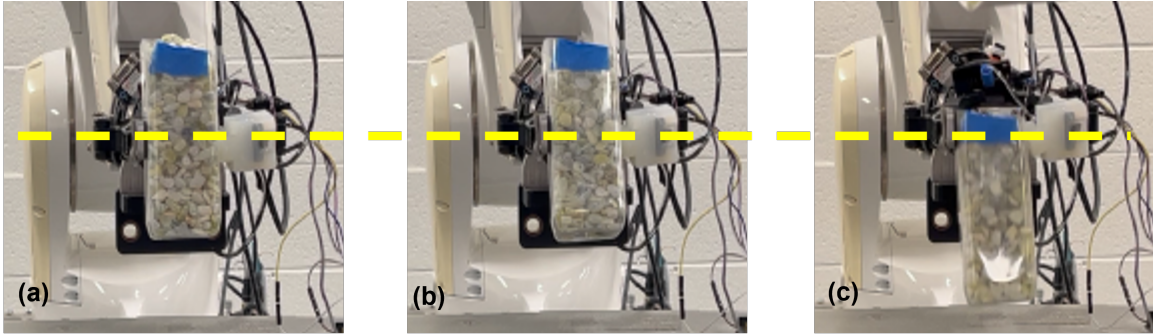
Figure 15. Grasping control test at the same flow of time(19 sec). (a) MRAC (b) Slipping distance compensation method. (c) Without any control method.

that the system input parameters will be updated to make the system error zero even if the system parameters are not given correctly. Moreover, the integral term is added to send the time derivative of the slipping distance to zero thereby immobilizing the object. In the hardware experiment, by comparing the MRAC with the others, it is presented that the MRAC is more robust than the others, as the weight keeps being added, since the velocity stays near zero relatively well. However, since this work doesn't cover more various types of objects in terms of shape, texture, etc., future works could include showing robustness against different grasping objects.
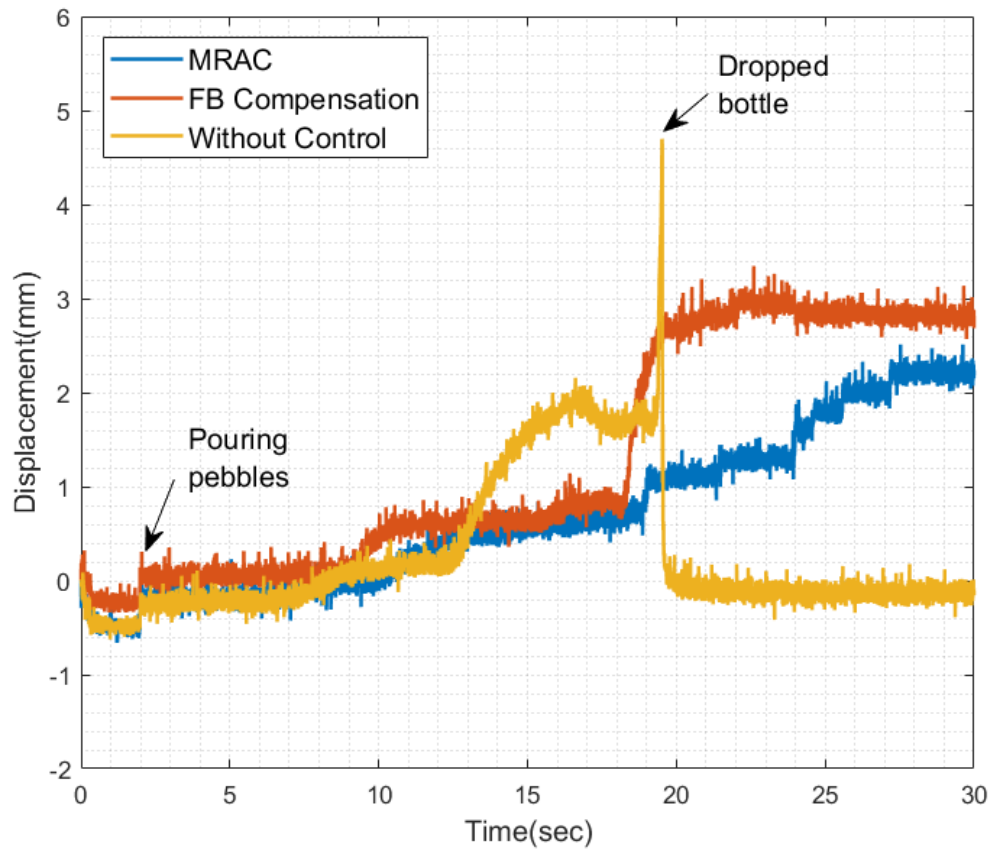
Figure 16. Slipping distances according to situations
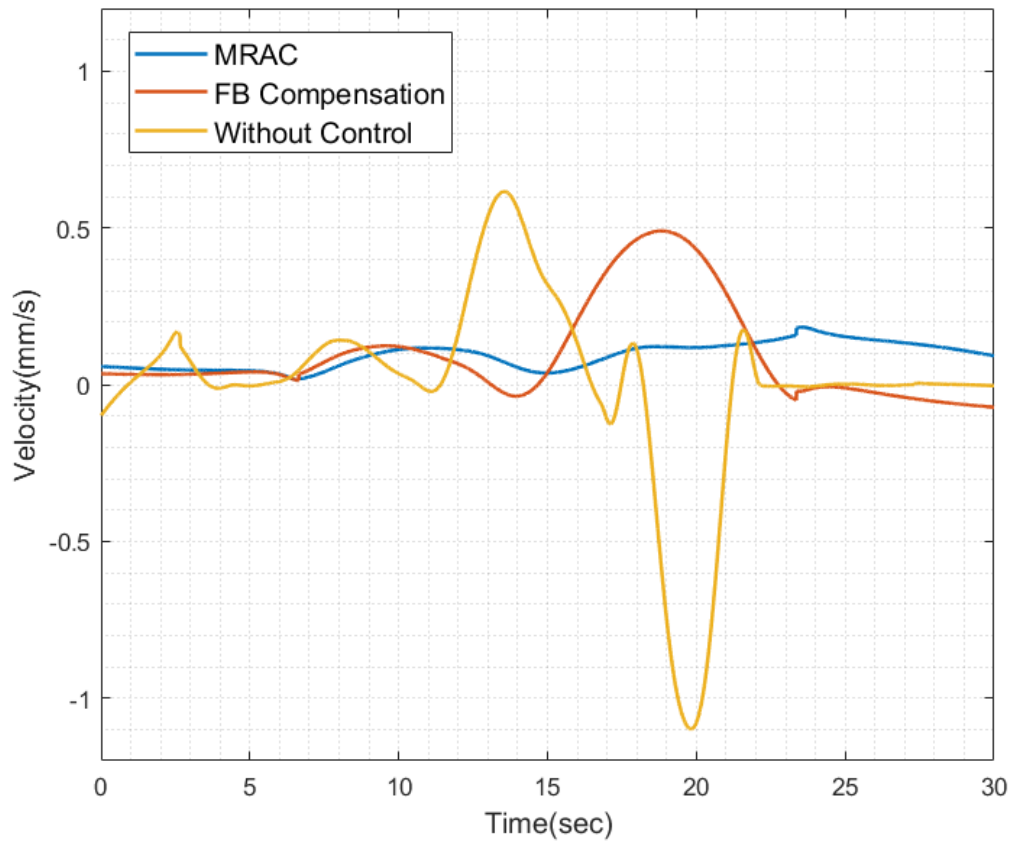
Figure 17. Time derivative of slipping distances after smoothing

CHAPTER III

INSPIRATION OF HUMAN FINGER ANATOMY

1 Trends in Anthropomorphic Hand Development

This chapter reviews previous efforts toward biomimetic robotic hands. Because the interest in robotic hands has been growing steadily for a long time and includes non-biomimetic approaches, "robotic hands" is too broad of a search term for this review, which focuses on biomimetics, materials, and integration. Our initial search methodology used the keywords "biomimetic robotic hand", "anthropomorphic robotic hand", and "bionic hand" with an "OR" operator, collecting articles for sorting within the scope of this review. As shown by the gray bars in Fig.18-(1),(2), the publication rate on these topics has increased across the years. The largest number of publications is in robotics journals, but articles also appear across multiple engineering domains and in neuroscience.

Although there were attempts to emulate human hands as iron prosthetics in the early Roman era [72] and other studies on robotic hands in the 1960s [73], research into robotic hands with human-like shapes intensified in the 1980s. The most well-known examples are the Salisbury hand (1982) from Stanford [74] and the Jacobsen hand (1984) from Utah/MIT [75]. Fig.18-(3) illustrates how those initial studies, shown as large dots on the upper left of the citation map, influenced subsequent research, with lines indicating citations between works.

Moreover, Fig.18-(3) displays colors representing each study's focus. Major focus areas include design, mechanism, and control.

In the 1980s and 1990s, a sophisticated design framework evolved, based on an
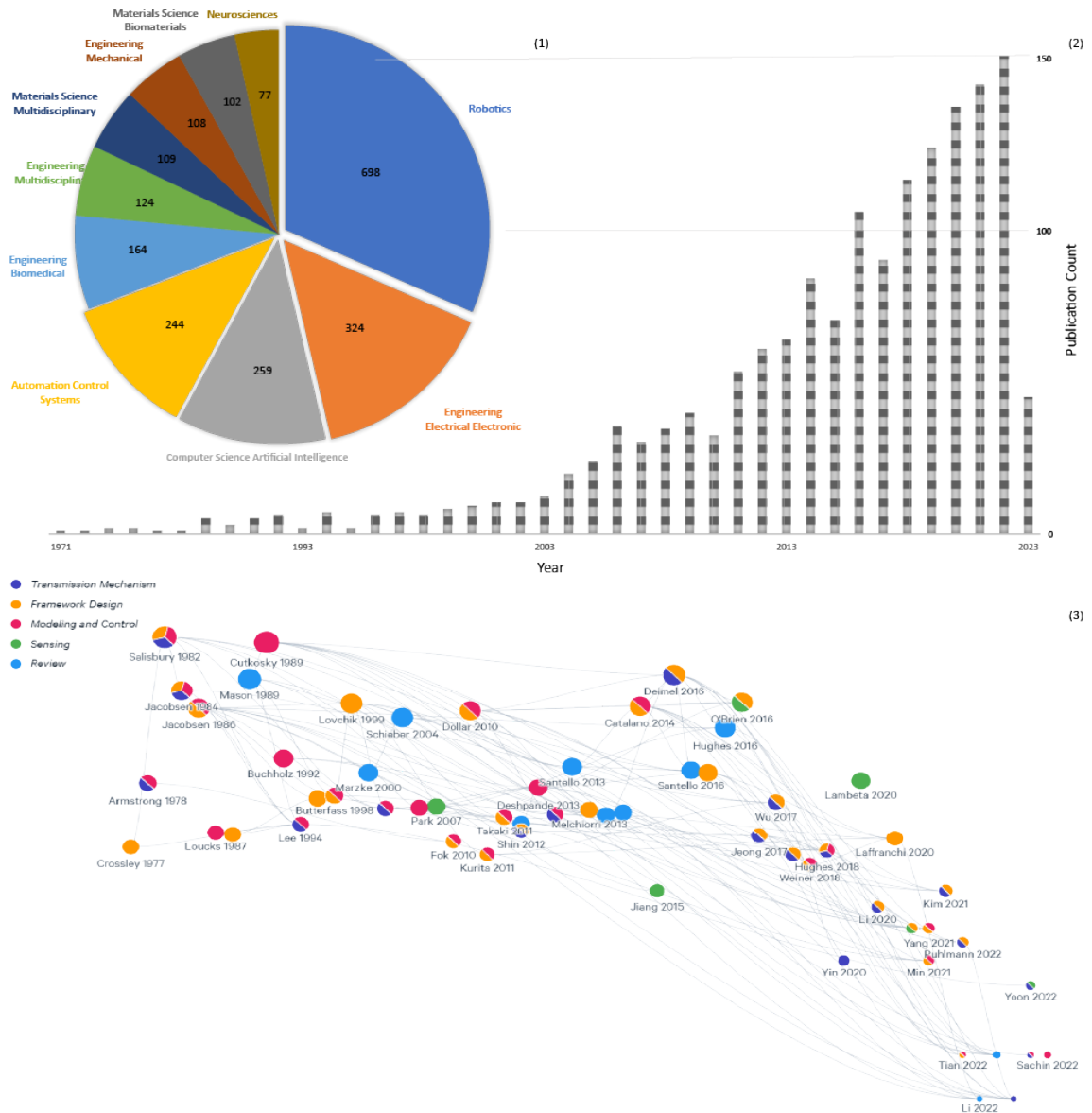
Figure 18. (1, Top left) Fraction of publication count in top 10 selected research areas from Web of Science (publications in two or more areas are counted in multiple wedges). (2, Top right) All 1,517 publications in this analysis, distributed across years 1971-2023 (Web of Science, WoS). (3, Bottom) Development trend for 60 selected publications including the Salisbury hand and Jacobsen hand (two large dots at upper left). Publications are organized from left to right by year (1977-2022), and organized top to bottom by number of citations (also indicaed by dot size), plotted using Litmaps. Dots are color coded to indicate one or more focus areas.

anatomical point of view. The intention was to make the system more dexterous. [76–79]. In recent years, advances in materials science, sensor technology, and

artificial intelligence have continued to drive the development of more advanced and sophisticated robotic hands [80–85]. Today, there are a wide variety of robotic hands and prosthetic devices that are capable of mimicking the complex movements and dexterity of the human hand, and these devices are being used in a variety of applications, from manufacturing and logistics to healthcare and rehabilitation [86]. Despite these significant advancements in design, fabrication, control, and dexterity, there still exists considerable room for improvement. Furthermore, Fig.18-(3) demonstrates a paucity of research that integrates three or more distinct areas of focus, indicating that there are untapped opportunities to explore in this multidisciplinary field. This analysis underscores the potential for new breakthroughs and further acceleration of progress.

2 Overview of Human Hand Anatomy - Biological Inspiration

Alongside development of prosthetic hands and robotic hands, there have been concurrent studies of human hand anatomy, functions, and mechanisms geared toward a better understanding of how our hands work. This topic is crucial to improvement of biomimetic artificial hands [87–89]. Therefore, in this section, human hands' structure is briefly reviewed in terms of the bone-tendon-muscle framework as well as the skin. We also cover previous research into understanding human hands' motion in both functional and mechanical aspects.

3 Bone-Tendon-Muscle Structure

Each human hand consists of 27 bones: 3 in the thumb, 8 in the wrist and, 16 in the rest of four fingers. Bones are the physical support for our hands [90]. These bones are connected with other bones and muscles by tendons. One of the main anatomical patterns is paired main tendons to open (extensor) or close (flexor) each finger, with the muscles connected to both extensor and flexor tendons located in the

35
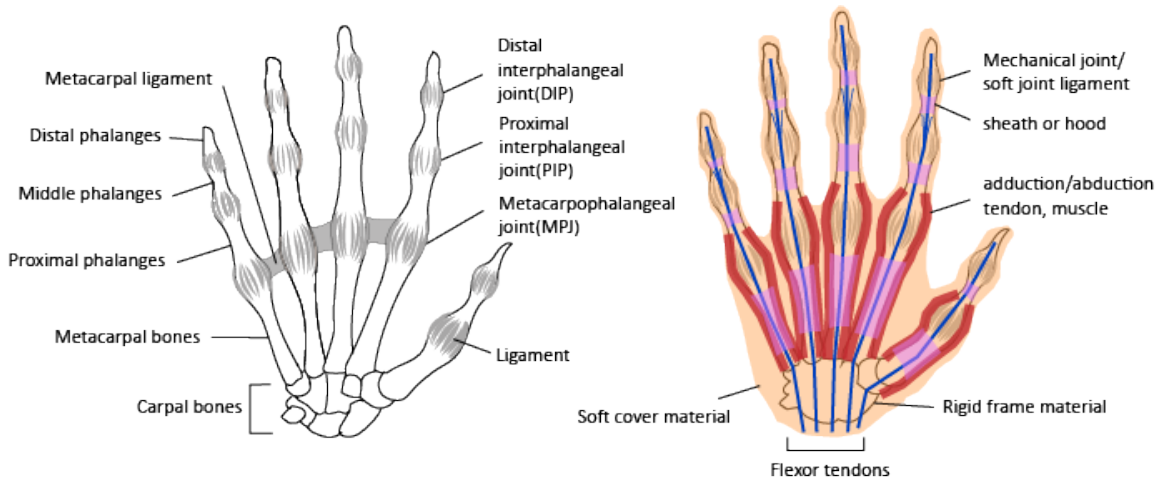
Figure 19. (Left)Illustration of human hand bone structure, (Right)Example of a possible artificial hand component arrangement, inspired by human hands.
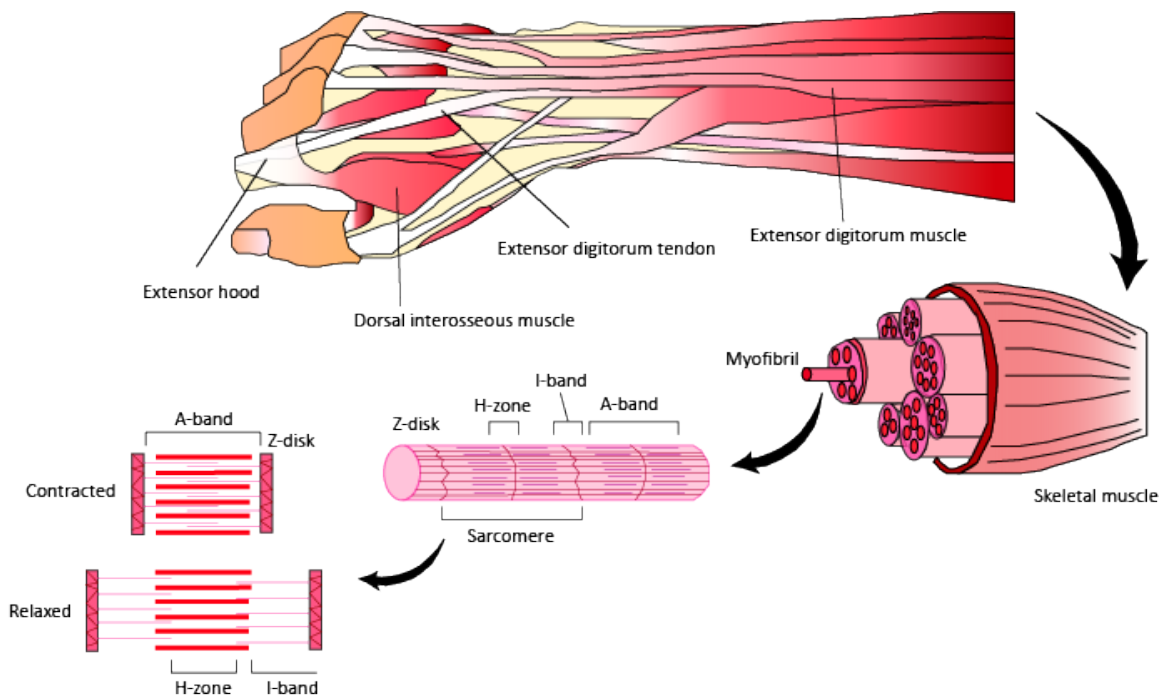
Figure 20. (Top)Illustration of tendon-muscle structure of human hand. Partially reproduced from [90]. (Bottom) Sequential zoom on the "belly" structure of a skeletal muscle. Motion generation starts from the molecular unit (bottom left). Motion is reinforced by multiple units that form larger skeletal muscle units and ultimately drive the whole hand.

forearm. Interestingly, however, the muscles for side to side finger motions (adduction, abduction) lie in the palm [91]. By distributing those muscles and tendons in the right

position with respect to tendons and bones, each finger joint is capable of its full range of motion.

In order to better mimic human hand motion, there have been mechanical and clinical investigations to measure tendon excursion and moment arm of finger muscles since those motions and forces define finger dynamics and explain internal forces and joint torques [89, 92–94]. It's not just a matter of pulling on a tendon by distance X and getting a fingertip displacement of Y, because of the elastic properties of biological materials. An interesting feature specific to hands is that finger tendons are a bit more viscoelastic and less elastic compared to other tendons in our body such as legs, allowing for precise control of movement and passive motion against external disturbances [95]. On top of that, the synovial sheath covers and guides tendons' path so that tendons and muscles are able to move smoothly and efficiently with natural lubricant [96]. Likewise, the bone and tendon of the human hand have specific physical properties in terms of their location, material, shape, and even texture which makes for integrated versatile motion. Therefore, it is essential to understand those mechanical characteristics and mechanisms in human hands and expand the features to modern biomimetic robotic hands. This subject will be expanded in later sections. The end of the tendon is connected with the muscle as mentioned before. In Fig. 20, the skeletal muscle located in the hand and forearm is composed of a bundle of muscle fibers. The function of the human muscle is obviously making motion. Researchers have developed sliding filament theory to describe the microscopic mechanism by which muscles move [97,98]. Sliding filament theory is summarized in the bottom left of Fig. 20, which illustrates how human muscle contracts and relaxes in molecular units. Described in a further main section, methods to actuate robotic hands are one of the major research topics in anthropomorphic robotic hand design.

3.1 Motion Mechanism

In the pursuit of highly versatile robotic hands, the fundamental question is how to effectively grasp, manipulate, and interact with objects. Consequently, researchers often describe the remarkable versatility of the human hand function by classifying its various prehensile actions [99–101]. However, it is important to note that human prehension is a complex process that integrates the intricate interplay of the bone-tendon-muscle structure, the sensory system embedded in the skin, and even cognitive processing including planning for multiple tasks. Napier points out that power grasping and precision manipulation are not mutually exclusive [101], implying that not only can human hands make separate postures for different tasks, but they can also perform multiple postures at once like in Fig.21. The overall classification system shows clearly the versatility and range of human hands. Based on this physiological standpoint, many current researches present posture versatility of artificial hands as a performance standard similar to the grasping classification in Fig.21 [102–106].

Non-prehensile	Circular sphere	Circular disk	Circular tripod	Lateral pinch
Wrap	Small wrap with thumb press	Thumb and 2,3-finger precision grip	Thumb and 3-finger precision grip	Thumb and 2-finger precision and power grip
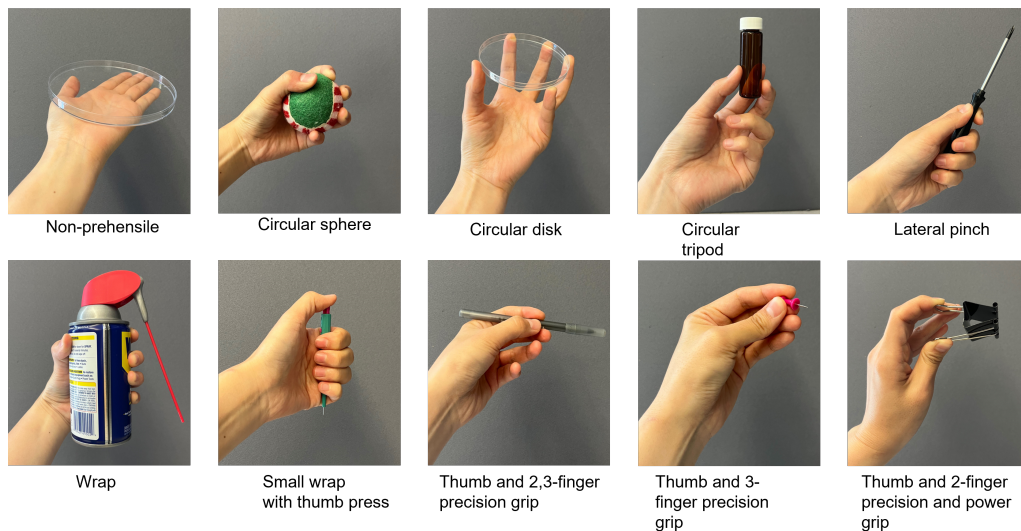
Figure 21. Selected grasping taxonomy from simple and complex daily life motions; subset of a larger taxonomy presented in [100].

4 Robotic Hand Functional Realization

The examination of human hand anatomy assumes pivotal significance in advancing robotic manipulators due to the inherently human-centric design of our daily tasks. This paradigm extends beyond commonplace implements like kitchen utensils to encompass industrial equipment and research instruments. These tools are meticulously crafted with ergonomic considerations, ensuring compatibility with the average human hand in terms of size and shape. Ranging from delicate fine-tipped tweezers to robust hammers and cordless power tools, the diversity of tasks necessitates a multifaceted approach. While the robot's adherence to dexterity and versatility is paramount, safety considerations become equally crucial in handling fragile and heavy devices, requiring the ability to modulate between soft and strong grips, as well as subtle and forceful touches.

Moreover, the interconnection of signals from tools with sensory feedback assumes key importance in manipulation control. These signals, encompassing pressure, temperature, and vision feedback, enable humans to seamlessly interact with their environment, establishing benchmarks for evaluating the success of manipulation tasks. In essence, understanding of human hand anatomy not only informs the design of robotic manipulators but also underscores integrating safety features and sensory feedback mechanisms to improve their overall effectiveness in many operational contexts.

The ultimate objective is to transfer human labor to robot labor, prevent workplace injuries, and move beyond human physical limitations. With industries such as food & beverage, aerospace & defense, and energy & power emphasizing "smart factories" where supplies and outputs are tracked throughout the manufacturing process, a highly sophisticated robotic manipulator could also raise the manufacturing performance, for example by sensing increases in assembly forces of injection-molded parts that indicate a mold is wearing out.

Therefore, inspired by human hands, there have been efforts to endow robotic manip-

ulators with human-like design, motion and function without completely duplicating all features of human hands. Different implementations geared toward different objectives have come out, including factory automation, clinical prosthetics, humanoid robots, and exploration robots, with various design features emphasized depending on the system's purpose [107]. Since cataloging the full diversity of these manipulators is beyond the scope of this article, this section is bounded to review highly anthropomorphic designs of robotic hands.

Recent developments often focus on new materials to implement state-of-the-art designs. Compared to 1980s-1990s designs, the 2010s-2020s designs are concerned not only with solid structures but also the softer components of robotic hands. This development is made possible by advanced fabrication processes, improved computing performance and multidisciplinary collaboration [108, 109]. In this section, by investigating robotic counterparts of human hands from a mechanical point of view, we show how anthropomorphic hands have been advanced in terms of design, material, modeling and, control.

5   Main Framework

Analogous to human bones, hard frames in robot hands provide support for other structures, sensors, and actuators. Such frames are able to perform highly coordinated movements as well as retain their own shape. Several early stage developments relied on frames, mainly focusing on simple manipulating functions with only rigid bodies [78, 89, 110]. In order to make the system adapt to the environment, active control strategies based on concrete modeling analysis have been investigated [111, 112]. Although these previous approaches led to fairly straightforward and intuitive drive and control methods, in some industries such as those dealing with delicate or fragile materials, robotic hands need to perform tasks in a conformable, passive manner [113, 114]. Accordingly, there is a trend to adopt shapes, sizes, and structures that resemble hu-

man hands' yielding the bone, tendon, sheath, ligament, and skin [115–117]. This trend is shown in Table 4, where the majority of the highly anthropomorphic designs feature elastomers in one or more components to realize active and passive mechanism mutually.

In applications where precision and accuracy of motion are critical, typically rigid body materials are more commonly utilized such as metals, hard plastics, strong fibers or cables. This choice facilitates the analysis of kinematics and dynamics, allowing for the isolation of linear terms while neglecting nonlinear factors like friction, hysteresis, and viscoelastic features. [118, 119]

In contrast to the somewhat human bone-shaped structures, recent investigations indicate that joint structures in robotic systems tend to be simplified, featuring 1 or 2-axis rotational joints to connect and mobilize individual phalanges. Additionally, innovative designs incorporating pulleys, either within or external to the hand, have been proposed. These designs not only guide tendons and reduce friction but also address underactuation challenges, occasionally at the expense of sacrificing one degree of freedom in the finger joint. Notably, some prosthetic hands continue to adhere to rigid bodies and relatively stiff cable wires for reasons of simplicity in control setups, cost efficiency, and compactness [119–121].

However, a paradigm shift is observed in biomimetic robotic manipulators and end-effectors, where a departure from rigid materials is embraced. Leading the way, these systems explore the use of softer, lighter, and safer materials. This strategic move towards compliant materials not only promotes biomimicry but also holds promise for enhanced adaptability and safety in various applications. [122, 123] These soft materials whose motion is coupled to rigid bodies can expand the range of function of existing robotic hands. Several works have gone even softer, adopting a compliant and passive framework instead of rigid bones so that the manipulator can have a higher degree of freedom (DOF) [84, 124]. On top of that, some studies in soft robotic hands

show more flexible sensors-embedded designs or smart-materialized designs, which are able to control the finger position or stiffness straightforward. [125, 126] But, in those cases, a certain level of pressure inside the finger is required to maintain its stiffness corresponding to rigid structures. In addition, understandably, the higher the DOF, the more complex the control system.

Therefore, many recent researches has shown how to interlace active and passive motion by selecting rigid and soft materials properly according to its main objectives. Besides, advanced 3D printing and laser cutting technologies excel sophisticated human finger design. [123, 127]

6 Actuation and Transmission

Once the main framework of the hand is established, it is time to generate motion. Depending on the objective of the system, the force transmission method, force generation method, and actuator placement will vary. Table 5 describes the major force transmission methods and their pros and cons. Some of these transmission categories are closely integrated with force generation methods (for example, artificial pneumatic or polymer muscles that actuate in place), while tendon and linkage based systems may be driven by a variety of force generators.

As illustrated in the Fig. 22, the prevailing architecture for robotic hand mechanisms, particularly in biomimetic applications, is predominantly tendon-driven. In the tendon-driven system, tendon cables placed in tightly confined spaces transmit the force to move the digits at the user's command. Since the multiple tendons can be connected directly to each phalange, it is also able to be applied to comparatively precise position control likewise the linkage-driven types. Due to weight, compliance and size limitations, however, the linkage-driven mechanism is less popular these days even though it has easy-to-design and higher motion accuracy features than other methods.
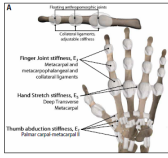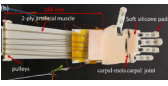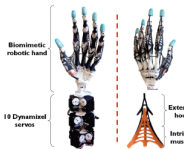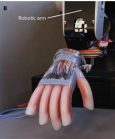
Name(Year)	Actuation	Component	DOF	Highlight
RBO Hand 3 (2022)	Pneumatic [124]	Fabrics, Silicone rubber, Plastics	16	high versatility and dexterity, Pull-out force 39N
Kim Hand (2021)	Linkage-driven [118]	Aluminum, Metal alloy, Silicone(fingertip)	15	Accurate motion, In-hand tactile sensor, Bending pressure force 34N
The Hannes Hand (2020)	Tendon-driven [119]	-	14	Prosthetics, Highly underactuated motion, Power grasping peak force 150N
Hughes Hand (2018)	Passive finger motion based on wrist actuation [128]	3D printed bones and ligaments	-	Anthropomorphic passive finger design
Wu Hand (2017)	Tendon-driven [85]	3D printing plastics, Silicone, Nylon fiber,	16	Twisted and coiled polymeric muscle
Xu Hand (2016)	Tendon-driven [106]	3D printed bones, Rubber, High-strength fiber	22+	3D scanned human hand design
Zhao Hand (2016)	Pneumatic [126]	Optical fiber, Nylon fabric, Silicone elastomer	-	Optoelectronic sensor for touching and grasping

Table 4. Recent developments in anthropomorphic robotic hand design by years

Conversely, the tendon-driven method offers a measure of system compliance owing to the elastic properties of tendons. While this introduces complexities in control and imposes limitations on maximum force transmission due to elongation and hysteresis, the benefits often outweigh the drawbacks. In recent times, advancements within the tendon-driven category have seen the integration of soft and robust materials. Twisted cables, commonly referred to as twisted string actuators (TSA), and twisted-coiled polymers (TCP) have emerged as innovations combining force generation and transmission. These materials exhibit superior power or weight efficiency compared to traditional tendon systems [85, 105, 129]. Given that this actuation and transmission system mirrors the muscle and tendon interplay in the human hand, tendon-driven mechanisms have been explored with alternative power sources, including motors and hydraulics/pneumatics [130].

Moreover, recent researches suggests the potential for replacing essential components such as main bodies, linkages, joints, and even tendons with alternatives employing pneumatic systems, and shape memory alloy (SMA)/shape memory polymer (SMP) [131]. These materials serve not only as mediums for force transmission but also as integral elements of the power source [125, 132]. As interest in human-machine interaction intensifies, there is a growing focus on soft and conformable bodies. These adaptive structures have the capability to encompass a broad spectrum of forces, ranging from delicate grips to power grasps, while dynamically adjusting to the shape and stiffness of various objects.

Likewise, each force generation method brings a new control challenge as well as advantages due to distinct physical properties as mentioned previously. Precise control of these soft, continuous, high-DOF actuation methods leads to another challenge: proprioception, or internal detection of the actuators' state, for closed-loop control. [133, 134] Therefore, in the next section, it is introduced how researchers are addressing the challenge using embedded sensors.
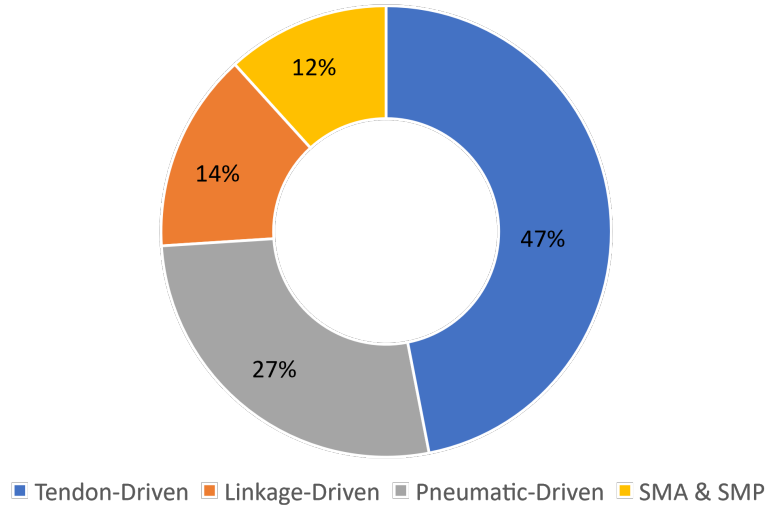
Figure 22. Proportion of transmission methods out of 196 research articles dealing with the development of the anthropomorphic robotic hand. Search keywords example : "anthropomorphic" AND "robotic" AND "hand*" AND "tendon*" from WoS

Mechanism	Advantage	Disadvantage	References
Tendon-Driven	Biomimetic motion, Compliance	Friction, Complicated control	[77, 81, 85, 106, 119, 135, 136]
Linkage-Driven	Straightforward design, Elevating control accuracy	Limited compliance and compactness	[118, 137–141]
Pneumatic-Driven	Safe, Soft, Robust interaction	Difficult miniaturization and control	[84, 124, 126, 142]
SMA & SMP	Lightweight, High force	Hysteresis, response latency	[143–145]

Table 5. Advantage and disadvantage of each force transmission method

7 Modelling and Control

The primary focus of robotic hand modeling and control lies in emulating human hand unit motions, encompassing the regulation of contact touch force, grasping force, finger stiffness, response speed, and fingertip positions within constrained workspaces. Researchers pursuing anthropomorphic robotic hands have made notable strides in novel frame designs, diverse actuation mechanisms, and skin-type sensor systems, as previously discussed. However, substantial challenges persist, with each section

exhibiting significant advancements yet lacking cohesive system integration and the attainment of seamless motions. Like Fig.23, a biomimetic scheme for motion control might be intricate as much as the human nervous system.

According to the classic engineering concept, a controller is constructed by starting with a solid model of the system. Indeed, such attempts have been made to control robotic hands accurately, with active control concepts added to make the system more robust [102, 146]. Based on a thorough forward and inverse kinematic analysis, the position and orientation of the system can be successfully controlled. Dynamic modelling allows researchers to go further, simulating the hand's behavior under different loading conditions and aiding in the development of control strategies [147]. These modeling processes involve techniques of not only dynamics and kinematics algorithms based on geometric and numerical optimization, but also data-driven approaches based on experimental measurements [86, 148–150].

Such data-driven approaches are the current trend. As the system gains components with different physical properties, such as when semi-rigid frameworks are combined with soft tendons and actuators, the variables multiply and the system becomes too complex for exact description. Thanks to advanced imaging technologies and improved computing performance, partial data-driven modeling methods have been actively researched to make the system more accurate without becoming computationally intractable [151, 152].

On the design side, underactuated designs help researchers reduce the system complexity because they have fewer actuators than DOF [121, 153]. And on the controls side, a concept called "synergies" has been studied in the context of achieving dexterous and efficient movements. [136, 154, 155] Synergies provide coordinated patterns of joint movements that allow the hand to perform grasping and manipulation tasks effectively. Since the underactuated design allows for shared mechanical elements, and since synergies give a simplified variable of motion, researchers have connected

46
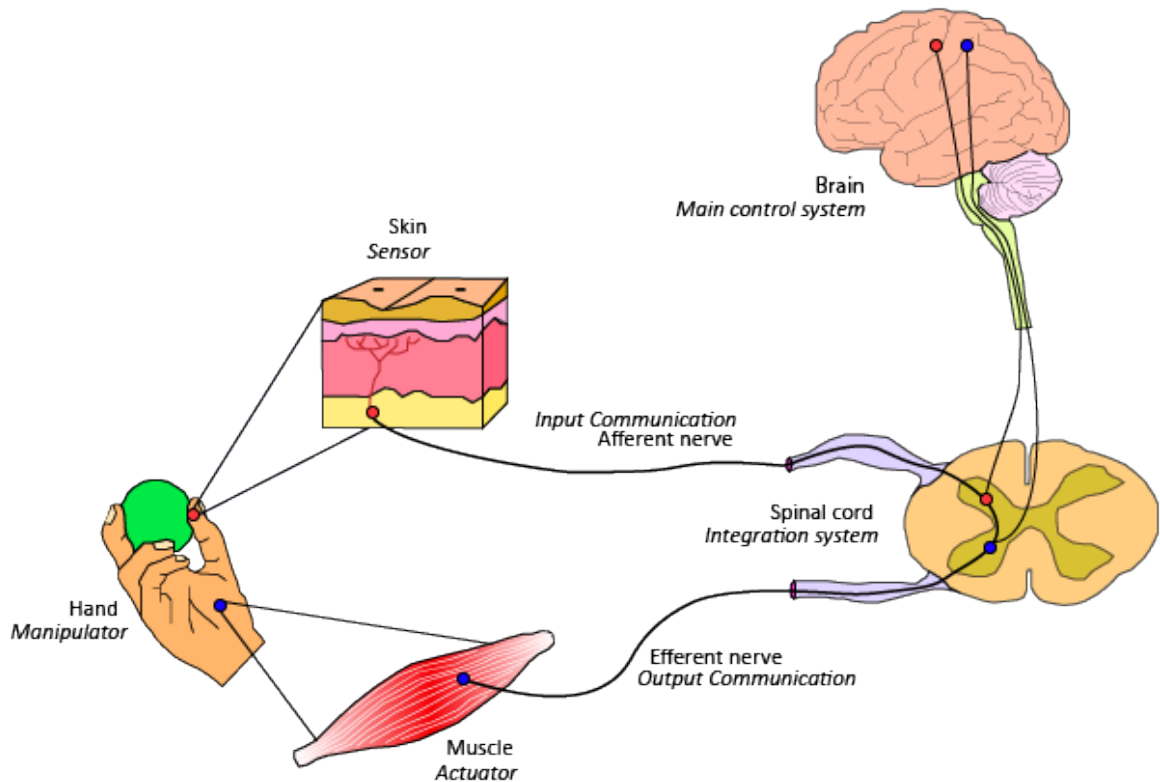
Figure 23. Human response control process from skin to muscle. Brain and spinal cord response time are around 200ms and 30ms respectively. [157] Each possible robot system counterpart is presented with Italic font.

the two concepts closely to improve robotic hands' capabilities [84, 156].

8 Discussion

Over the past 50 years, advancements in materials science, sensor technology, and artificial intelligence have propelled the field of biomimetic hands, producing a wide variety of robotic hands and prosthetic devices. Key advances in the past 10 years include soft sensors and actuators, machine learning coupled with sensors, and a new appreciation for the mechanical intelligence of compliant and underactuated mechanisms.

However, despite significant progress, there are still areas that require improvement, including design, fabrication, control, and practicality. Notably, there remains a dearth of research on the seamless integration of disparate technologies for the pur-

pose of effective sensing, processing, and dexterous motion. For instance, as previously discussed, while significant progress has been made in the development of anthropomorphic design, tactile skin sensors, and various types of actuation, there is still a need to explore their intimate and natural connection between those systems not only mechanically but also computationally in order to advance the field of robotic manipulators to the next level.

Evolution has shaped our current hand structure, while humans have subsequently created the diverse environments that we interact with on a daily basis. The need to manipulate objects in varied settings has necessitated the transfer of this dexterity to robots, allowing for the delegation of mundane and repetitive tasks.

Ongoing research focuses on understanding the anatomy and functions of the human hand to guide the development of robotic counterparts. Fueled by emerging materials, fabrication methods, and computing techniques, one day we may develop manipulators that can mimic or even outperform the complex movements and capabilities of the human hand.

In conclusion, the journey from human hands to robot hands has been marked by steady progress, but there is still much room for improvement. By studying and understanding the human hand's structure and capabilities, researchers and engineers can continue advancing robotic hand technology, aiming for even greater dexterity, functionality, and integration with human users.

CHAPTER IV

DEVELOPMENT OF ANTHROPOMORPHIC ROBOTIC INDEX

FINGER

Given the insights from the previous chapter, there is merit in developing a robotic manipulator inspired by the human hand. Such a design offers both versatility and safety in functionality, while potentially improving efficiency from an engineering standpoint. However, comprehending and analyzing the mechanism and motion of the finger to design and control such a manipulator may not be straightforward. Hence, this chapter undertakes a review of general manipulator kinematics in accordance with the design considerations of the developed system. Incorporating system constraints enables a more realistic scenario for robot manipulation to be considered. Through simulation, an example of scenario cases is implemented utilizing a simple PD controller. Finally, a novel robotic finger design is introduced, detailing materials, dimensions, and other hardware information. Eventually, in the following chapters, it is also shown the idea of how the hardware can be utilized and implemented.

1   System Modeling

The forward kinematics of a manipulator represents the mapping $T_{st} : Q \to SE(3)$, which describes the relationship from joint variables $\theta \in Q$ to the position and orientation of the end-effector $SE(3) = \{(p, R) : p \in \mathbb{R}^3, R \in SO(3)\}$ in the base frame. In this project, it is assume that the finger manipulator consists of 4 revolute joints and 4 links. Then, the kinematics can be described based on the product of exponentials

formula:

$$T_{st}(\theta) = e^{\hat{\xi}_1 \theta_1} e^{\hat{\xi}_2 \theta_2} e^{\hat{\xi}_3 \theta_3} e^{\hat{\xi}_4 \theta_4} T_{st}(0) \tag{20}$$

where ξ_i represents the twist corresponding to the ith joint axis in the reference configuration, which is $\theta = 0$ and can be found as below.

$$\hat{\xi} = \begin{bmatrix} \hat{\omega} & v \\ 0 & 0 \end{bmatrix}, \hat{\omega} = \begin{bmatrix} 0 & -\omega_3 & \omega_2 \\ \omega_3 & 0 & -\omega_1 \\ -\omega_2 & \omega_1 & 0 \end{bmatrix} \tag{21}$$

where the axis of rotation $\omega \in \mathbb{R}^3$, $\|\omega\| = 1$ with $v = -\omega \times q$ and $q \in \mathbb{R}^3$ is a point on the axis.

Now the relationship from the joint space to the workspace can be decided as follows:

$$g_{st}(\theta) = \begin{bmatrix} R(\theta) & p(\theta) \\ 0 & 1 \end{bmatrix} \tag{22}$$

Then, basically the position and orientation of the end-effector can be calculated as well as the posture of the manipulator from the joint angle input like the Figure 24. But further consideration is needed because the manipulator is driven by the actuators, which generate torques for the revolute joints. Therefore, the force and torque should be taken into account so that the dynamics of the manipulator can represent how the finger moves in response to the actuators. In order to write the equation of motion, the Lagrangian analysis is used in this derivation. In the meantime, the kinematics formulation is also utilized to describe the Lagrangian with respect to the joint angles and joint velocities. However, the full derivation is explained in the Appendix section so that in this section it is directly brought to the equation of motion in terms of the joint angles as below.

$$M(\theta)\ddot{\theta} + C(\theta, \dot{\theta})\dot{\theta} + N(\theta, \dot{\theta}) = \tau \tag{23}$$

The matrices M, C and, N represent the inertial properties, Coriolis matrix and, gravity terms of the manipulator, respectively. τ is the vector of joint torques.
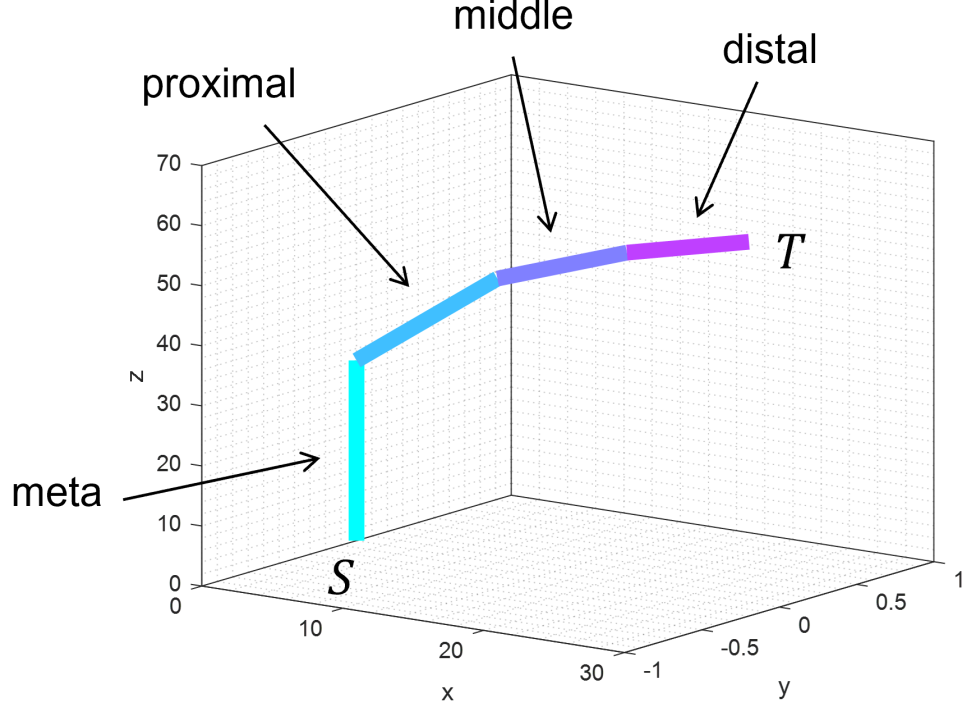
Figure 24. 4-link, 4-joint simple manipulator system based on the kinematics calculation. $\theta_1 = 0, \theta_2 = 30°, \theta_3 = 20°, \theta_4 = 10°$. From S(base) frame to T(tool/end-effector) frame, metacarpal, proximal, middle, distal phalange

Based on this second-order vector differential equation for the motion of the manipulator, one simple example can be considered like the Figure 25. There is a constrained surface, which the end-effector of manipulator should follow with generalized forces against this surface. Mathematically, this restriction can be represented with a holonomic constraint as follows:

$$h(\theta, x) = 0$$

$$\underbrace{\frac{\partial h}{\partial \theta}}_{J} \dot{\theta} = -\underbrace{\frac{\partial h}{\partial x}}_{G^T} \dot{x} \tag{24}$$

where $x \in \mathbb{R}^3$ indicates the allowable motions of the manipulator in the 3-D space. By using the velocity constraint from the equation 24, it is needed to rewrite the equation of motion of the overall system because the previous equation of motion 23 only presents joints' motion by actuator torques. Therefore, the relationship between the joint space and task space should be considered. The full equation derivation is

51
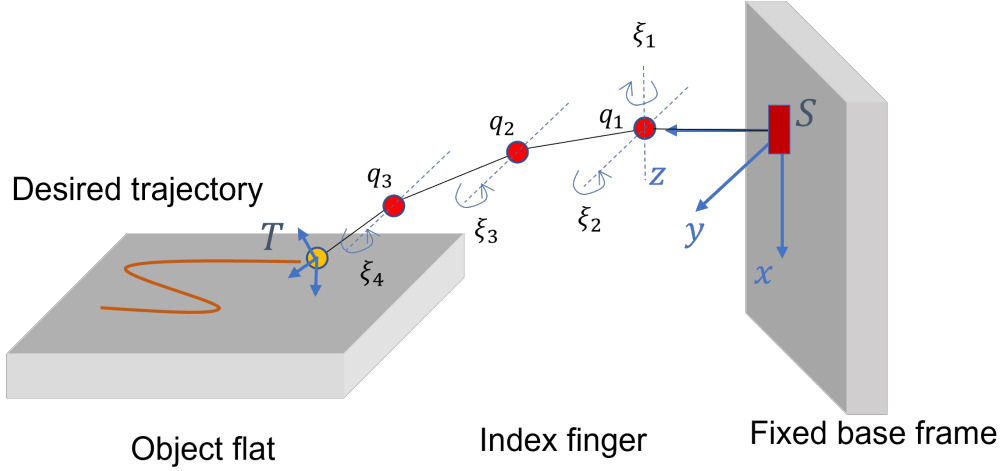
Figure 25. Illustration of finger manipulator with the simple surface constraint.

also written in the Appendix chapter. Then, the final dynamics of the system can be given by

$$\tilde{M}(q)\ddot{x} + \tilde{C}(q,\dot{q})\dot{x} + \tilde{N}(q,\dot{q}) = F \tag{25}$$

where $q = (\theta, x)$ is the generalized system configuration.

One thing that should be noted is how to set the constraint surface. If the surface is not approachable by the manipulator, it will lead to another problem. Thus, in this project, one allowable surface is picked from the workspace and we see if it can be followed by the manipulator through the controller. In the next section, based on the system model, the simple controller is designed and the simulation implementation is presented.

2 Simulation Results

Now, it is ready to figure out if the mathematical model can make a proper motion with controller and constraints. Starting from the simple motion control in the joint space, in this section, it is shown that the task space position control with the surface restriction, thereby the system model can be verified.

When it is assumed that the manipulator is actuated by joint torque and it is able
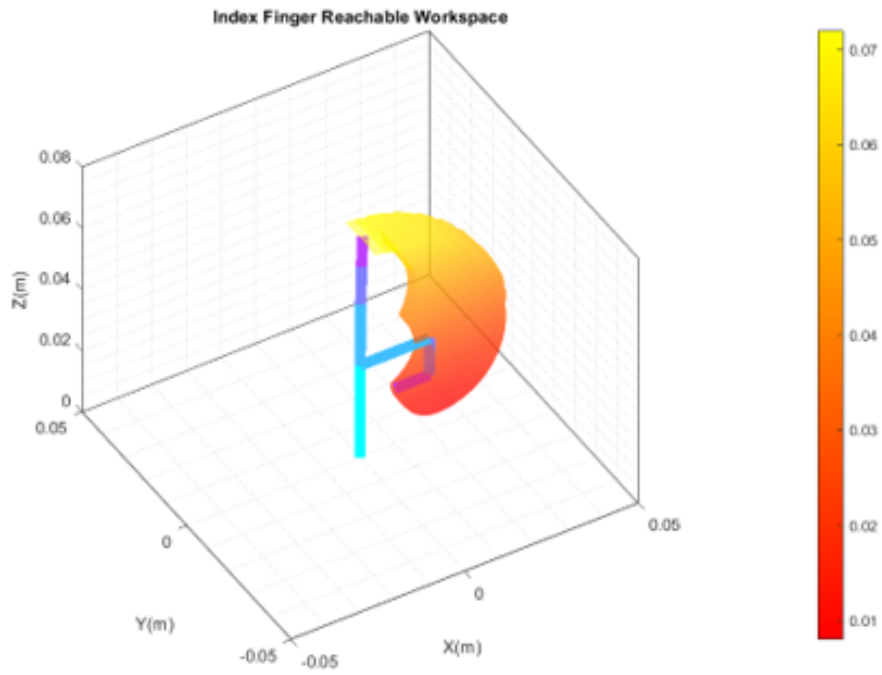
Figure 26. Approachable workspace of the manipulator system in the 3D. The minimum and maximum of the each joint angle are $[-10°, 10°]$ for θ_1 and $[0°, 90°]$ for θ_2, θ_3 and, θ_4.
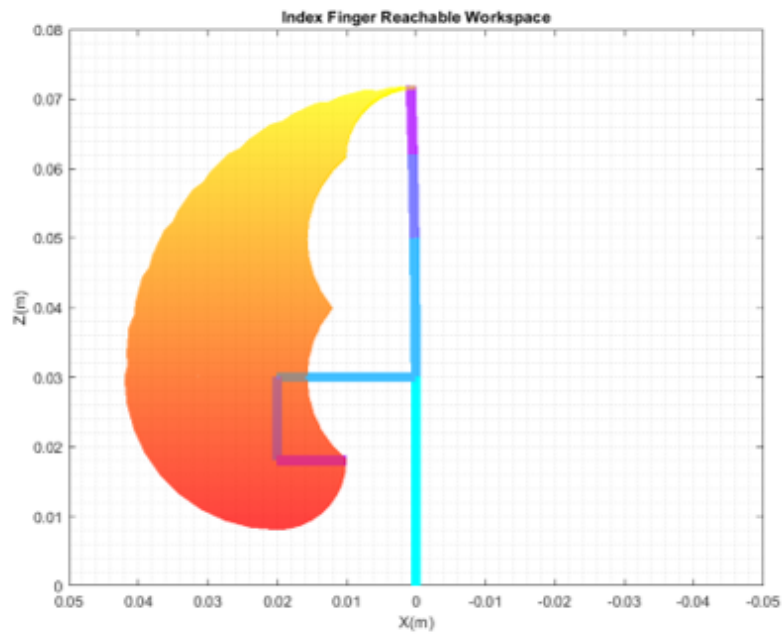
Figure 27. Approachable workspace of the manipulator system in the XZ plane.
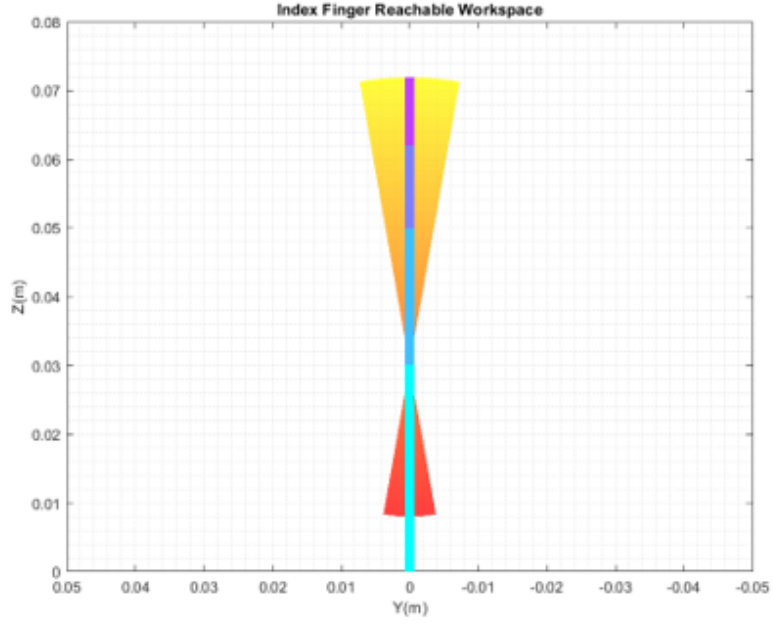
Figure 28. Approachable workspace of the manipulator system in the YZ plane.

to control the torque, the simplest application that can be considered is joint angle control. Given the desired trajectory of the joint angle θ_d, the error can be written as below.

$$e = \theta - \theta_d \tag{26}$$

In order to follow the desired trajectory, the control input u should be designed based on the basic equation of motion 23. In this example, the computed torque controller is considered which is basically calculate the system input torque based on the feedback and feedforward terms of the system [157]. Then, the control law can be designed as in Figure 29 and as follows:

$$u = \ddot{\theta}_d - K_v \dot{e} - K_p e$$
$$\tau = M(\theta)u + C(\theta, \dot{\theta})\dot{\theta} + N(\theta, \dot{\theta}) \tag{27}$$

Like Figure 30, the manipulator follows well with the error less than 0.1 degree. Therefore, the system modeling with the joint configuration is verified through the simple computed torque controller.
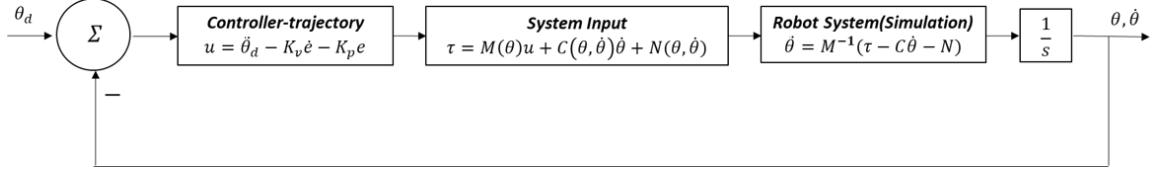
Figure 29. The block diagram of the computed torque controller
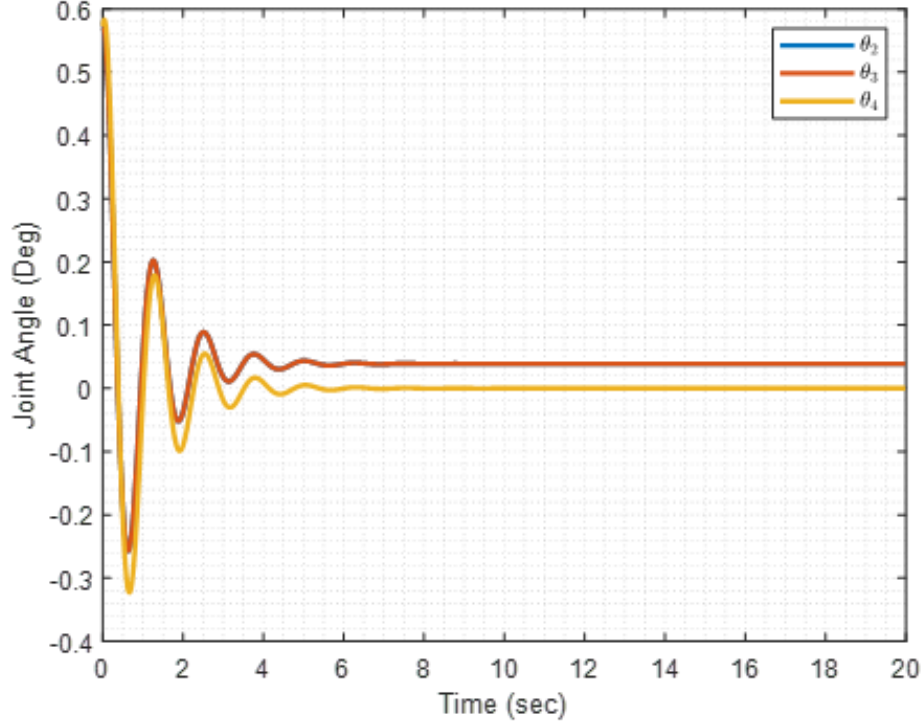
Figure 30. Simulation result of the joint angle error based on the computed torque controller. The desired trajectory is $\theta_1 = \theta_4 = 0°, \theta_2 = \theta_3 = [0°, 10°]$.

When it comes to the end-effector's position control, the modified equation of motion 25 in terms of the generalized configuration $q = (\theta, x)$ is already found in the previous section. In this case, the control input u is redesigned to follow the desired trajectory x_d in the task space with the error $e = x - x_d$. Then, the virtual force F can be calculated as below.

$$u = \ddot{x}_d - K_v \dot{e} - K_p e$$

$$F = \tilde{M}(q)u + \tilde{C}(q, \dot{q})\dot{x} + \tilde{N}(q, \dot{q})$$

(28)

55

The system input torque can be calculated by the virtual force F as follows :

$$\tau = J^T G^+ F + J^T f_N \tag{29}$$

where f_N is the internal force of the finger. While f_N can be utilized for the finger force control given the desired force f_d, in this example it is assumed that f_N is zero to simplify the system. Then, like the Figure 32, the manipulator motion is simulated with the one example of the surface constraint. It is necessary to find the proper surface, which includes approachable path of the manipulator tip position in order to conduct the task like the Figure 31. The error results are also shown in the Figure 33, 34, 35. Therefore, in this section, through system identification and simulation in the mathematical way, it is shown that the manipulator can be operated to make a desired motion with respect to the robot torque input.
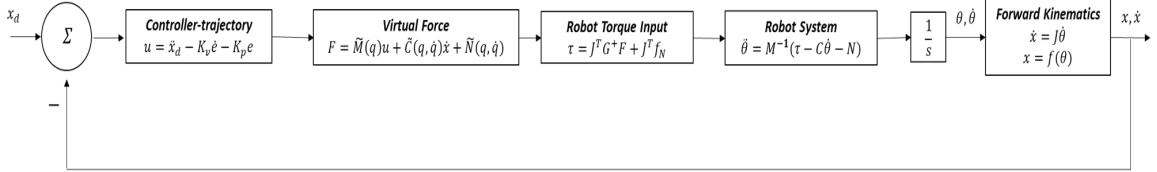
Figure 31. The block diagram of task space control with the surface constraint

3 Prototype Design

As mentioned earlier, to make versatile and subtle motion of the manipulator, it is necessary to refer to the human finger structure and mechanism, which are the most intricate exemplification. While the analytical examination is conducted in the previous section, the empirical study is mainly concerned in this section and further. Starting from the concept design like the Figure 36 which is inspired by the human index finger, it is shown that the robotic finger manipulator consists of 4-link, 4-joint with the rigid plastic material, flexor, extensor tendons and, the sheath with the soft and flexible polyurethane and resin material.
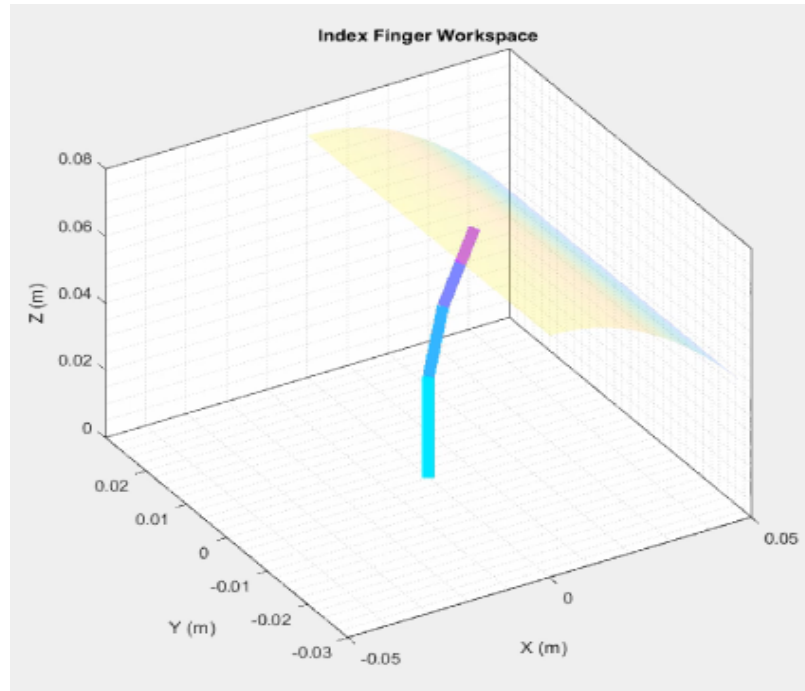
Figure 32. Animation of the task space control following the trajectory on the allowable surface. The trajectory is $z = p_1x^2 + p_2x + p3$ where $p_1 = -13.7, p_2 = 0.003053, p_3 = 0.072$.
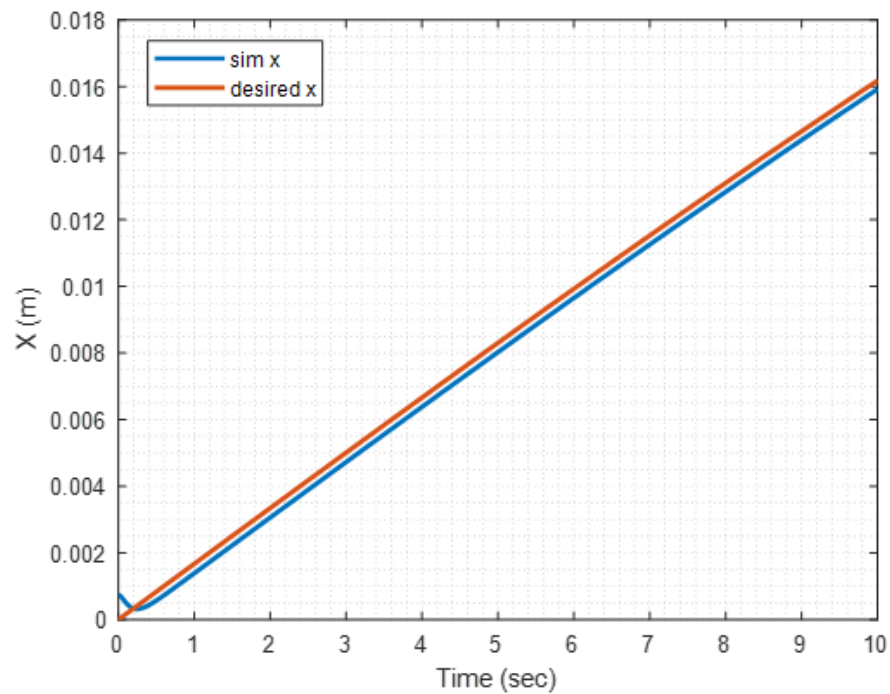
Figure 33. Simulation result of the position tracking in X-axis
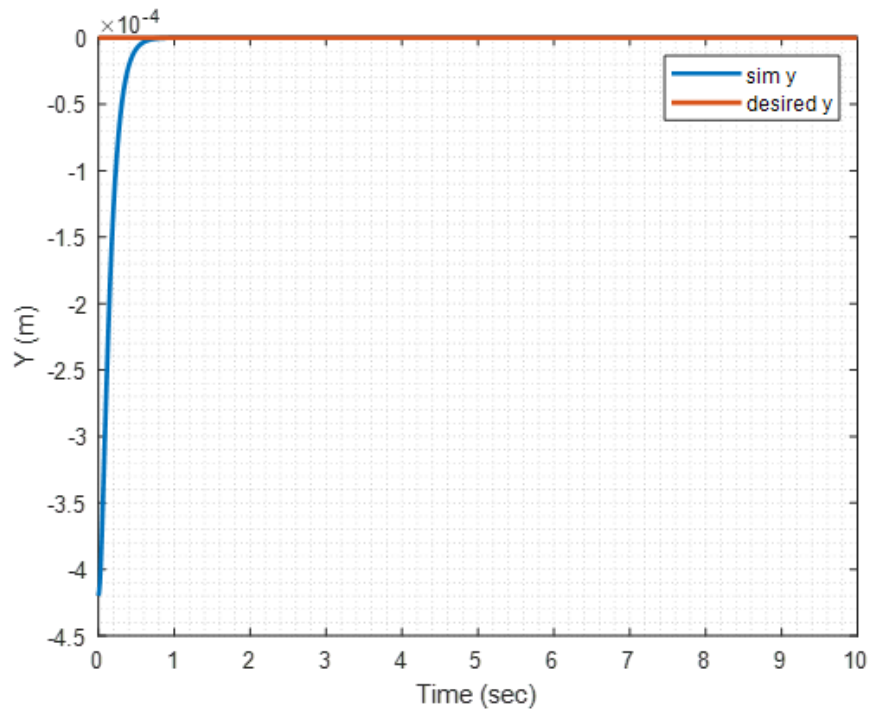
Figure 34. Simulation result of the position tracking in Y-axis
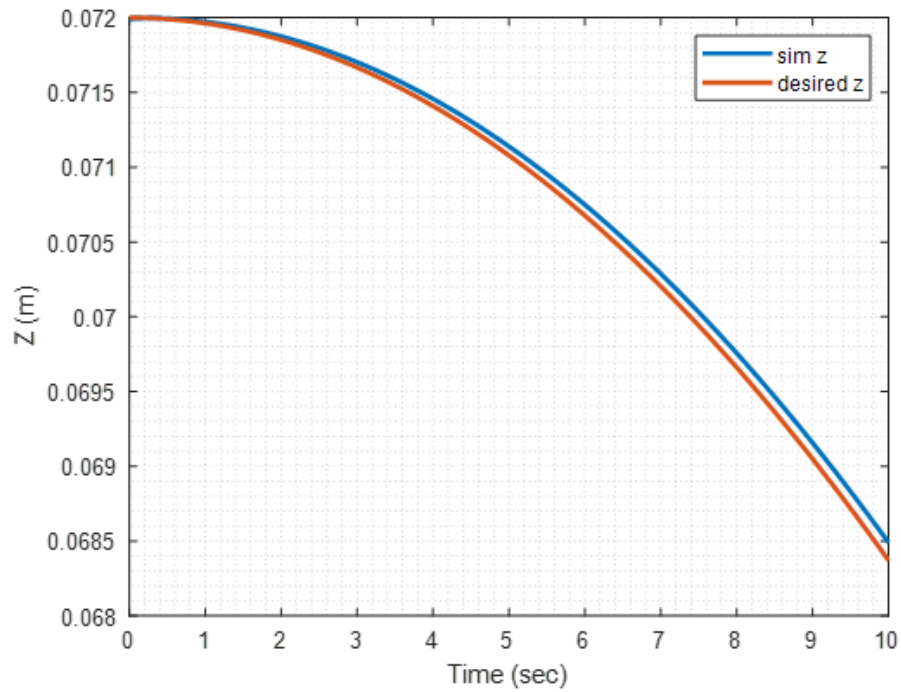
Figure 35. Simulation result of the position tracking in Z-axis

As the developing stage goes further, the main design structure is maintained except for some dimensions and the finger tips material. Figure 37 and 38 show the very first prototype of the finger manipulator, which are human finger-sized. However, this design doesn't include proper sheaths or pulleys, which are necessary to guide the tendons' path and protect them.

Figure 39, 40 shows a more organized version of design. In order to make a consistent and reliable path of tendons, the sheath is designed and 3d printed with the flexible material(Elastic 50A resin, Formlabs Inc.) so that it prevents tendon wear-out from the rigid edges and is able to interact more safely and softly.

One notable thing in this design is the clear, transparent tendon, which lets the light travel inside the fiber. In short, this optical fiber is able to be utilized as a measurement system as well as the tendon structure in this finger. Therefore, the next chapter explains how the optical fiber is used as the measurement tool as well as the driver of finger motion.

4   Conclusion

In this chapter, we examined the modeling process for the finger manipulator, which mirrors the structure of the human index finger with 4 revolute joints and 4 links. Leveraging kinematics, we successfully portrayed the finger's position and orientation within the workspace via simulation, extending our analysis to derive the equation of motion. With this foundational understanding, we explored how the manipulator can be controlled in terms of its joint configuration.

Moreover, we addressed the crucial aspect of incorporating object-touching constraints, which led to a transformation of the system dynamics into terms of task configuration, specifically representing the finger tip's position. This adaptation enables the manipulator to adhere to desired trajectories even within constrained surfaces, enhancing its practical utility.
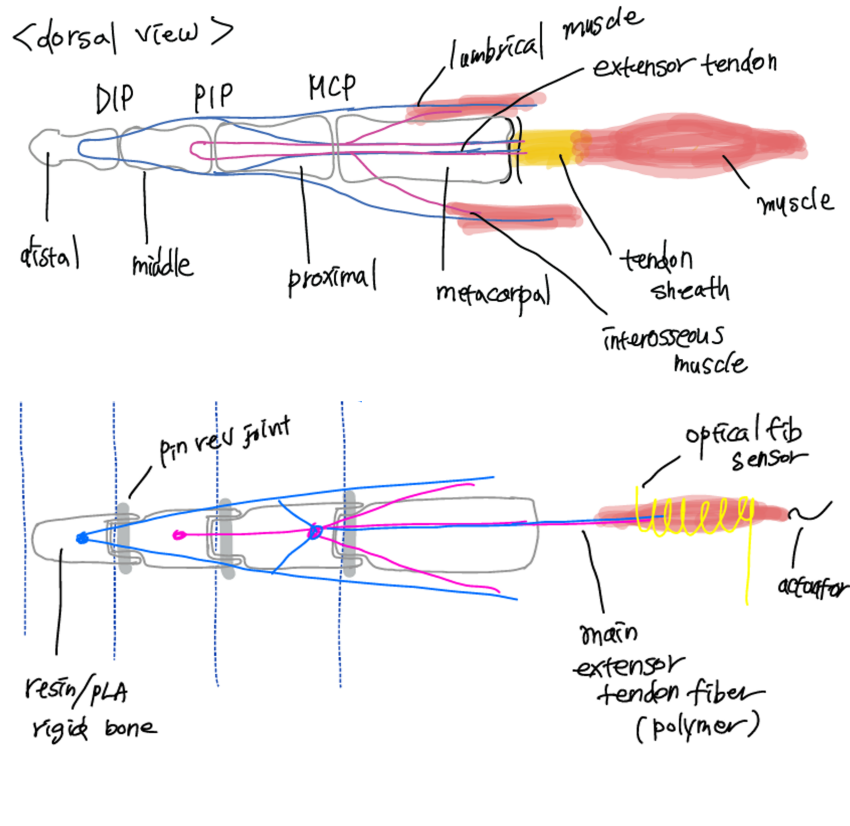
Figure 36. Initial concept design of the finger manipulator inspired by the human index finger structure.
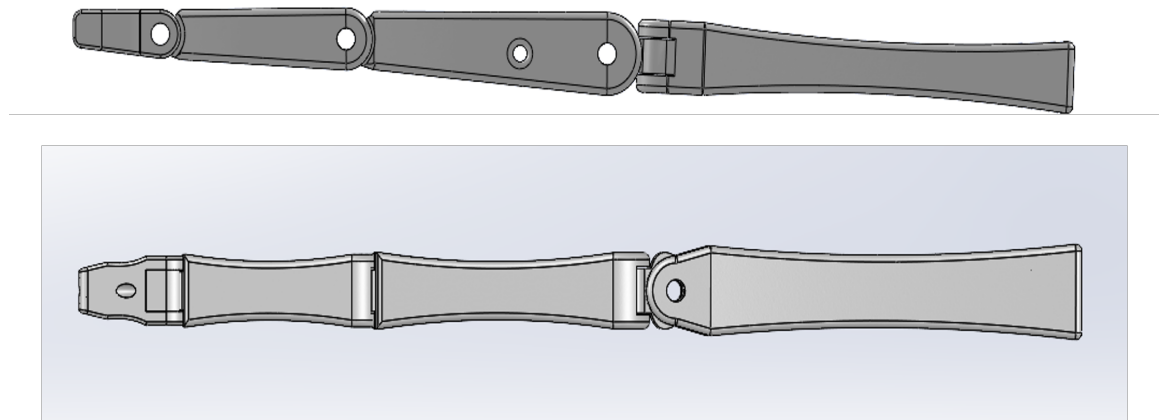
Figure 37. First version of the prototype 3D design.

Beyond theoretical exploration, our work progressed to the practical realm with the introduction of a novel prototype design and material for the finger manipulator. Drawing inspiration from the intricate structure of the human finger, our selection of
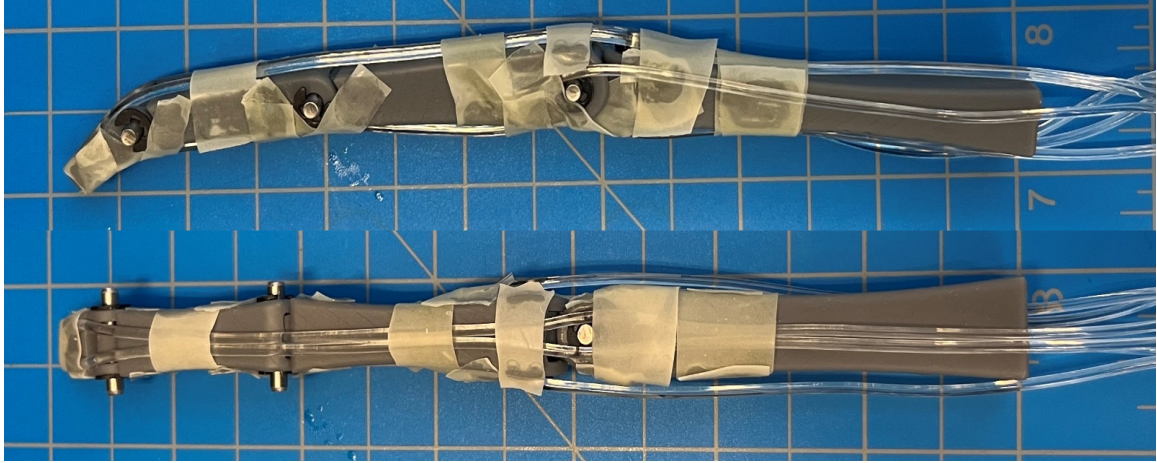
Figure 38. First version of the prototype printing with temporary finger pulleys and sheaths.
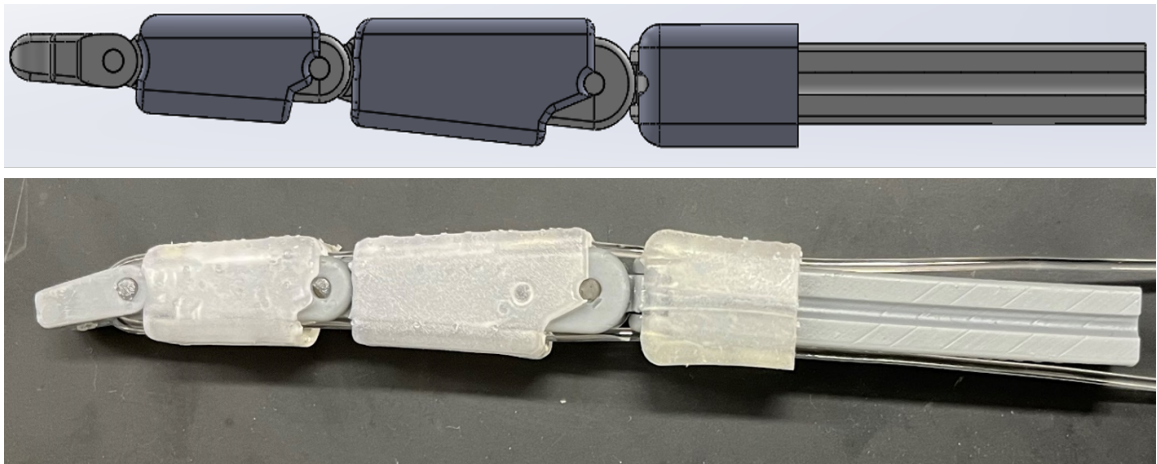
Figure 39. Second version of the prototype manipulator.

design, dimensions, and range of motion was considered.

Moving forward, the subsequent chapters will spotlight the evolution of our prototype, showcasing its capabilities through the second and third iterations. We will demonstrate how the finger can execute motions and seamlessly integrate with a new sensor system, thereby advancing the manipulator's functionality and applicability in real-world scenarios.
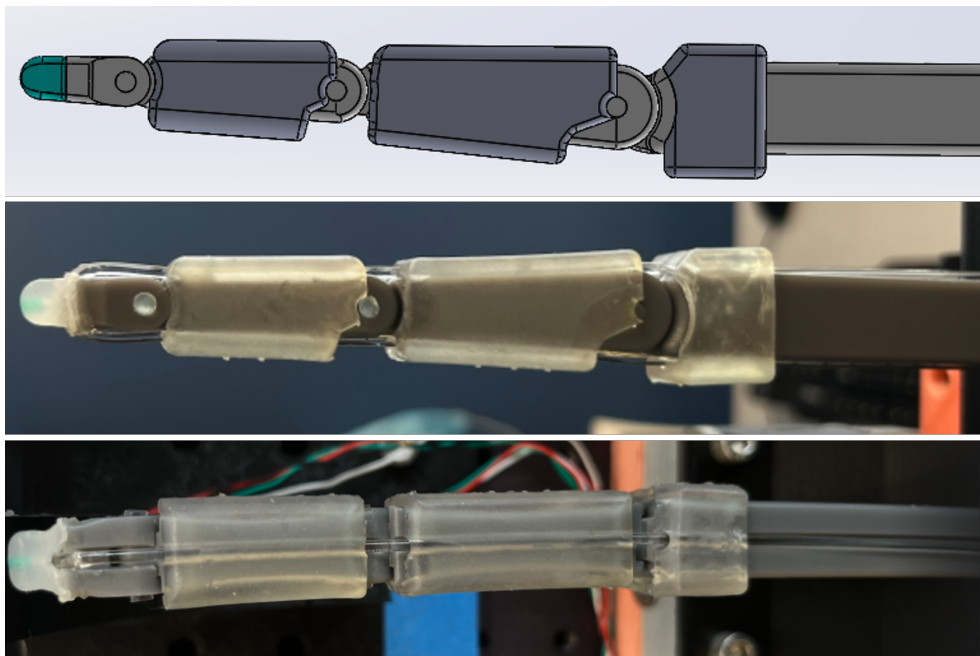
Figure 40. Third version of the prototype manipulator. This finger comes with the silicone pad finger tip for amplifying contact force sensing.

CHAPTER V

INTEGRATION OF POSTURE ESTIMATION
WITH THE ROBOTIC FINGER

1 Motivation

Within the framework of the tendon-driven system, this project strives to effectively incorporate human finger design in a straightforward manner. The strategic use of both rigid and soft materials aims to create a synergistic effect. Specifically, we employ stiff plastic resins for the bone structure, while flexible resins find their place in the finger pulleys and sheaths. A noteworthy departure from previous researches lies in our approach to tendons, where we utilize a soft and flexible optical fiber running from the fingertip to the actuator side. This fiber serves a dual purpose, not only transmitting force but also offering valuable measurement data. A key distinguishing feature of our system is the departure from conventional sensing approaches. Whereas most shape-sensing applications rely on Fiber Bragg Grating (FBG) sensors [158, 159], our system employs a straightforward and compact arrangement of LED and photodiode sets to capture variations in light power intensity. Although we will delve into more intricate details later, this innovation promises a novel, cost-effective, and user-friendly design for implementing a bio-inspired robotic finger system.

2 Kinematics

To facilitate the intricate motion of the finger, a comprehensive understanding of its kinematics is imperative. Our primary emphasis within this system is on comprehending the tendon input-to-joint output mechanism and how optical measurement
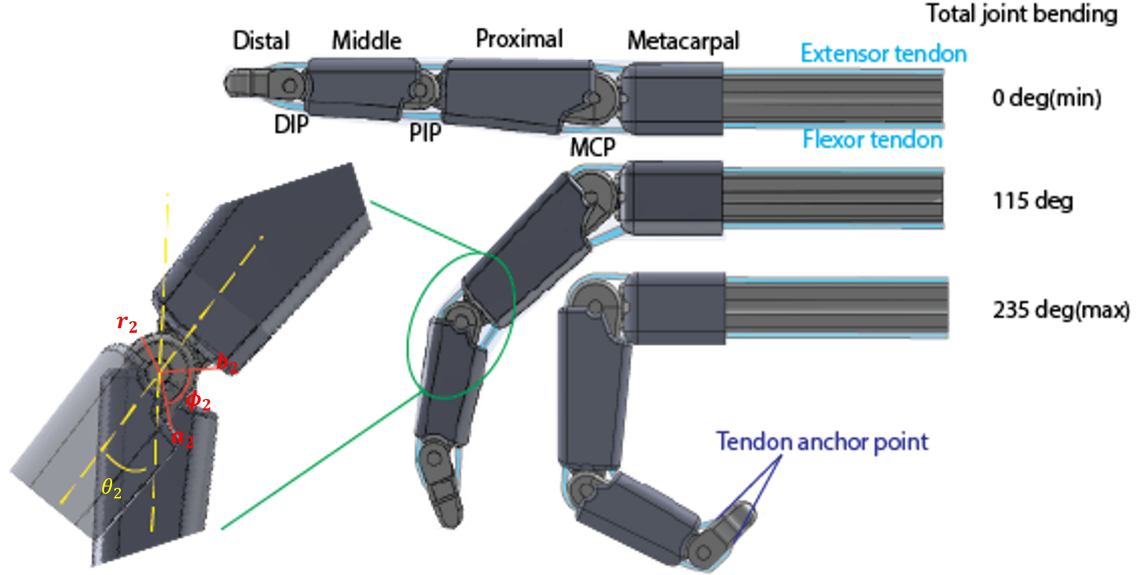
Figure 41. Finger 3D design from SolidWorks. On the left inset, the proximal-interphalangeal (PIP) joint geometry is illustrated as an example. r_i describes each joint radius to calculate extensor side displacement and a_i, b_i, ϕ_i are adjacent side lengths and the initial state angle between the two sides to compute the flexor tendon displacement.

data varies according to its motion. As such, this section describes from the actuator side to joint angle, which is able to determine the whole pose of the finger since the full forward kinematics also can be given by the design.

2.1 Actuator-Tendon Relationship

The fiber tendon is continued beyond the optical sensor and light source with a thin stainless steel cable (0.2 mm diameter) to prevent deformation of the sensor caused by winding it around pulleys. Through the connector between the stainless cable and the optical fiber boards, it moves as an one body to transmit the force directly from the motor to the tendon of finger. Thus, it is assumed that the displacement from the motor to stainless cable transfers fully to the optical fiber tendons. In the meantime, the motors used in this system are controllable by angle directly. Since the pulleys are connected to these motors with radius $r_m = 8$ mm, it is straightforward to compute the tendon-actuator relationship using the arc length calculation $\theta_m = l_i/r_m$, where

l_i is the tendon displacement which must be released or taken up to open or close the finger joints.

2.2 Tendon-Joint Space Kinematics and Dynamics

There are two motors to actuate the finger's flexion and extension motion, which are closing and opening movement respectively. The extensor tendon (l_e) is associated with releasing the fiber along the tendon path assuming that the path follows an arc shape. As opposed to the extensor, we assume that during pulling motions the flexor tendon (l_f) acquires the shortest path line based on the cosine law. Each calculation can be described in terms of the final design dimensions:

$$l_e = l_0 + (r_1\theta_1 + r_2\theta_2 + r_3\theta_3) \tag{30}$$

$$
\begin{aligned}
l_f = l_0 - (&\sqrt{a_1^2 + b_1^2 - 2a_1b_1cos(\phi_1 - \theta_1)} \\
+ &\sqrt{a_2^2 + b_2^2 - 2a_2b_2cos(\phi_2 - \theta_2)} \\
+ &\sqrt{a_3^2 + b_3^2 - 2a_3b_3cos(\phi_3 - \theta_3)})
\end{aligned}
\tag{31}
$$

where l_0 is the initial length of the tendon, θ_i presents each joint angle, which are distal-interphalangeal(DIP) θ_1, proximal-interphalangeal(PIP) θ_2, metacarpophalangeal(MCP) θ_3 joint in order, and a_i, b_i, ϕ_i, and r_i are each phalange's geometric dimension as shown in Table 6.

With the given kinematics, this system is unlikely to addresss each joint input separately due to the inherent nature of underactuated systems. Since the tendon displacement is calculated, the relationship between the tendon force (f) and joint torque (τ) is given by the law of energy conservation [160]. Let $s = l(\theta) = \begin{bmatrix} l_e \\ l_f \end{bmatrix}$ describe the vector of tendon extension and flexion, then the geometry of tendon and joint angle

can be modified by the force and torque relationship as follows:

$$\dot{s} = \frac{\partial l}{\partial \theta} \dot{\theta}$$
$$\tau = \frac{\partial l}{\partial \theta}^{T} f$$

(32)

where $\frac{\partial l}{\partial \theta} \in \mathbb{R}^{2X3}$. As far as the joint angle is concerned, it can be assumed that the left side of the torque equation 32 equals zero because of the equilibrium condition. Then, the θ can be determined according the net force of the tendon. However, the exact solutions might not be possible due to the nonlinearity of the Jacobian matrix and the net force calculation. In that case, optimization or other numerical methods can be considered. Thus, in this project, it is assumed that the initial tendon force is fixed and without external forces to produce the uniform joint angle motion. The repeatability of the hardware is shown during the multiple data training in the implementation section.

i	$a_i(mm)$	$b_i(mm)$	$\phi_i(deg)$	$r_i(mm)$
1	5.80	5.68	107.71	3.40
2	6.62	6.70	97.83	4.20
3	9.44	9.17	100.55	6.90

Table 6. Kinematic dimensions of the prototype design

3 Optical Fiber as a Measurement

As for the optics, the higher the refractive index, the more the light will be confined to the waveguide at bends and at interfaces. Therefore, it is found that the transparent polyurethane (MatterHackers, TPU, clear, diameter 1.8mm) is a good option with its refractive index near 1.5 (air refractive index, 1.0). As the sensor, this optical fiber of the system transmits the light power from the LED (IF-E91A, peak wavelength 930nm) source to an amplified photodiode (IF-91B, max sensitivity wavelength 920nm) detector. These components allow one to measure the transmitted light intensity as an analog voltage (0-5V) to analyze the fiber's physical deformation or

loading force. For shape sensing, transmission can be described by light loss (dB) as follows:

$$L = 10log_{10}(\frac{I}{I_0}) \tag{33}$$

where the initial power is I_0 and the current power is I. However, because transmission loss is an integrated measurement along the deformed fiber, which undergoes pressure, stretching, and multipoint bending, the relationship between light loss and the joint angle vector is complex. A forward model based on bending loss can be constructed [161], but the inverse problem is likely to have multiple solutions. As shown in Figure 42, the light transmittance through a single bending joint decreases with angle. The variation is small because Figure 42 only considers fiber bending according to a finger closing motion from 0 to 70 degree on the single MCP joint, while the other joints are held at 0 and 50 degrees respectively. However, when it comes to real measurements like those in Figure 43, which account for not only bending but surface contacts and other deformations, the transmission loss through the optical fiber sensor is considerable. Given those data, while the light power does decrease according to the lumped joint bending angle, a one-to-one regression is difficult due to the system's other uncertainties such as friction, tendon elongation, viscoelastic properties of the tendons, and micro-bending. Therefore, even though the idea of shape sensing stems from the relationship between the bending angle and light loss, this study finds an aggregated function using a machine learning technique in order to make a data-based model of the sensor system.

In the meantime, as a tendon, the fiber has some advantages. It is lightweight, is smooth enough to be guided by sheaths and over pulley-like joints. Since the fiber is soft and flexible, it conforms easily as the finger joints are bent, but it can still be firmly attached to the end of the finger. This material is also functional in water and with electrical or magnetic interference. Thus, it can be utilized as the device of the force transmission. However, due to the elasticity of the TPU material, some extent
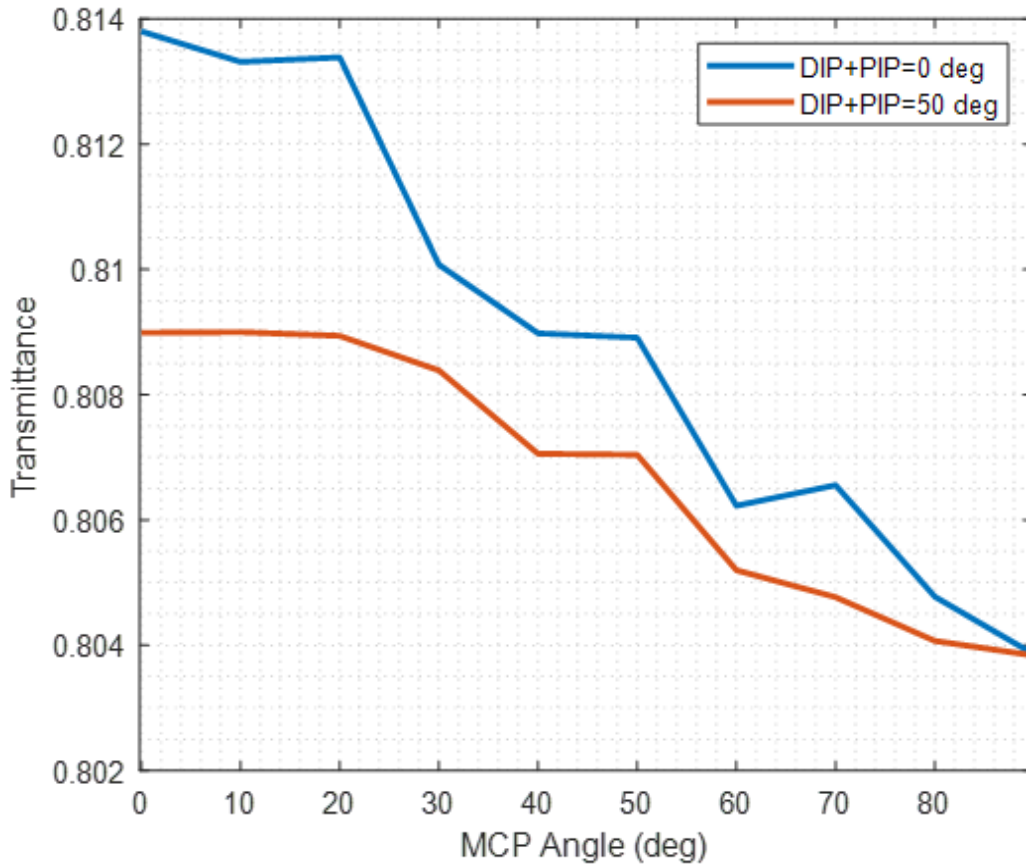
Figure 42. Transmittance simulation (COMSOL) giving the ratio between initial power at the fiber inlet and current power detected at the fiber outlet during MCP joint angle change.

of elongation is inherent in the fiber. In order to overcome the problems led by this feature, in the fixed range of tendon force, the system motion is observed without applied external forces. Since the Young's modulus (168.52-109.90 MPa, 0-5N) is obtained by tensile testing, we can estimate how much displacement is involved in the elongation at a given force. As mentioned earlier, although it is assumed that the external force is not considered in this system, friction can be considered to compensate the elongation displacement. Through experiments it is observed that the 1 N tendon force is associated with generating around 0.35 mm displacement elongation.
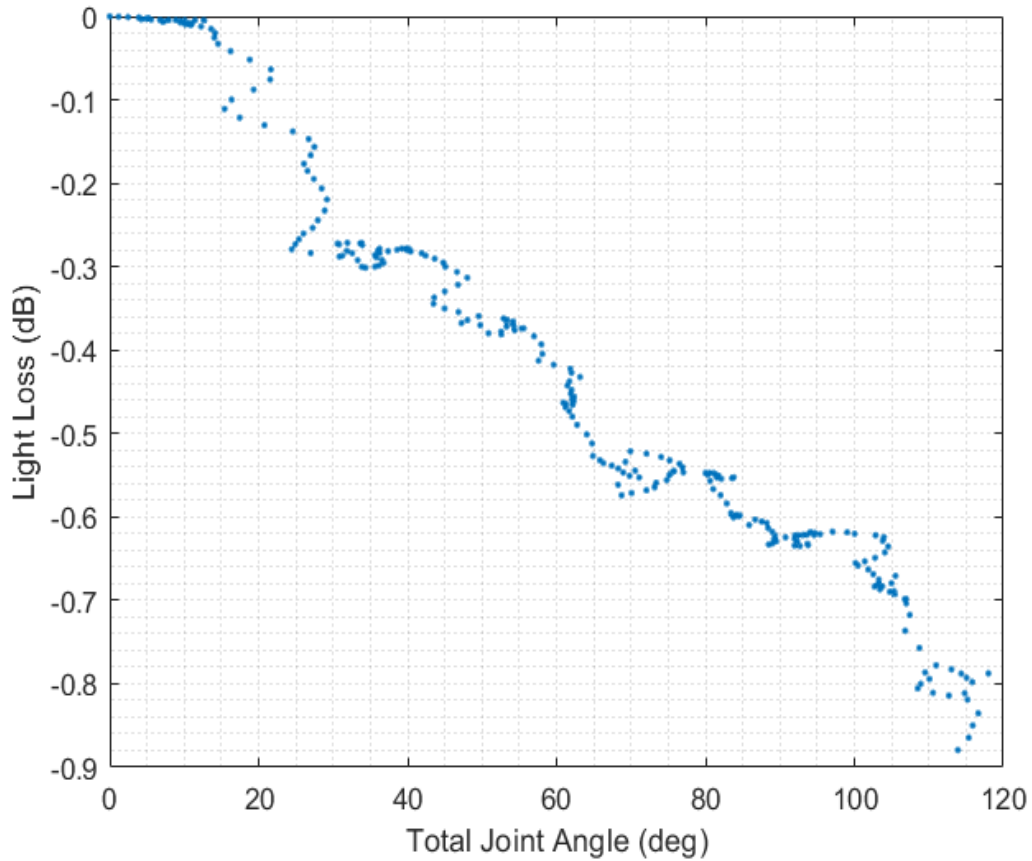
Figure 43. Measured light intensity loss as a function of total joint angle

4 Implementation

In this section, the technical details of the prototype setup are introduced. The goal of this experimental testbed is to observe the motion of the finger and evaluate the feasibility of the sensor through a machine learning calibration process. The whole process is composed of 1) tendon displacement calculation, 2) creating finger motion, 3) taking image data from a camera, 4) training the extracted actual angle data (ground truth) against the light intensity data, and 5) comparing trained and measured data. This is also illustrated in Figure 44.

Based on equations 30 and 31, the two tendon displacements are computed once the desired joint angle is decided. By taking image data from Azure Kinect (Microsoft),

the actual angle can also be extracted. Through neural network training (Matlab), we show the light intensity data is fitted to the sum of actual bending angle.

4.1 Hardware Setup

Each component of the finger is 3D-printed using Form 3+(Formlabs Inc.) except for the tendons. The rigid bone structures and joint pins are based on a resin material (Formlabs Grey Resin) and the sheaths as the finger pulleys and hoods are made with a flexible clear resin (Formlabs Flexible 50A). The total weight and length are 28 g and 165 mm respectively, and the three pin joints have maximum range of motion 80/65/90 degree (DIP/PIP/MCP). The design is inspired by the actual human finger size. The tendons are installed and free to move inside the sheath guided by the top path of the bone.

As shown in Figure 45 and 46, there are 2 motors (Dynamixel 430, Robotis Inc.), which communicate with a PC directly, to actuate the flexor and extensor tendons. Also, LED emitter and photodiode amplifier boards [162] are connected to the Arduino Uno to send the measurement data to the processor. One thing to note here is that the flexor and extensor tendons are actuated independently even though they are one body of fiber. Because the light sensing relies on a source and detector in the same fiber, the fiber tendon passes through the distal bone and is fixed on both sides to make it controlled separately. In the meantime, additional sensors are needed to collect training data and validate the results, which consist of a loadcell (HT Sensor Co. 5kg capacity) to measure the tendon forces and a camera to extract the current joint angles of the finger.

4.2 Shape Sensing

As mentioned earlier, shape sensing is associated with the total bending angle of the finger from 3 joints since the fiber makes curvature following their motion. While
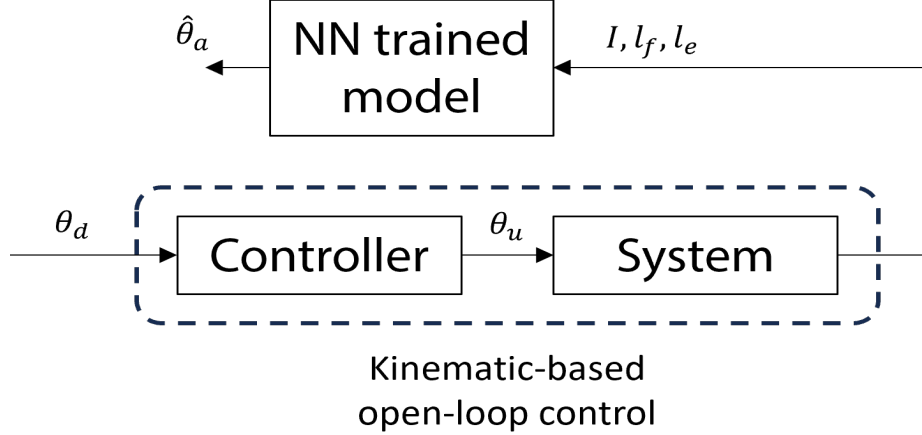
Figure 44. Flowchart of the finger system control. $\hat{\theta}_a$, θ_u are the estimated angle and the motor actuator input respectively.

there are not enough degrees of freedom to control 3 joints independently with two tendons, it can be expected that the finger motion will stay uniform under the same initial tendon force and without disturbances. Therefore, when collecting data for training, it is important to keep the consistency of the setup, particularly the initial tendon force. Now, based on the desired configuration, the actual joint angles can be computed through color recognition algorithm (cv2, pyk4a library in Python), which captures each point on the links of finger so that each joint angle can be extracted through a vector dot product calculation. Then, those actual data are analyzed to get the relationship between the total bending angle and light intensity loss. The training process is conducted by a neural network algorithm (15 hidden layers, Bayesian regularization backpropagation) in Matlab as the post-processing. So, the function output is the total joint angles and inputs are tendon displacement and intensity ratio (I/I_0) between current power and the initial value.

5   Results

Once the basic setup is arranged, the finger is actuated by motor-tendon-joint calculation. The total angle input increases from 0 degree to 120 degree. Starting from
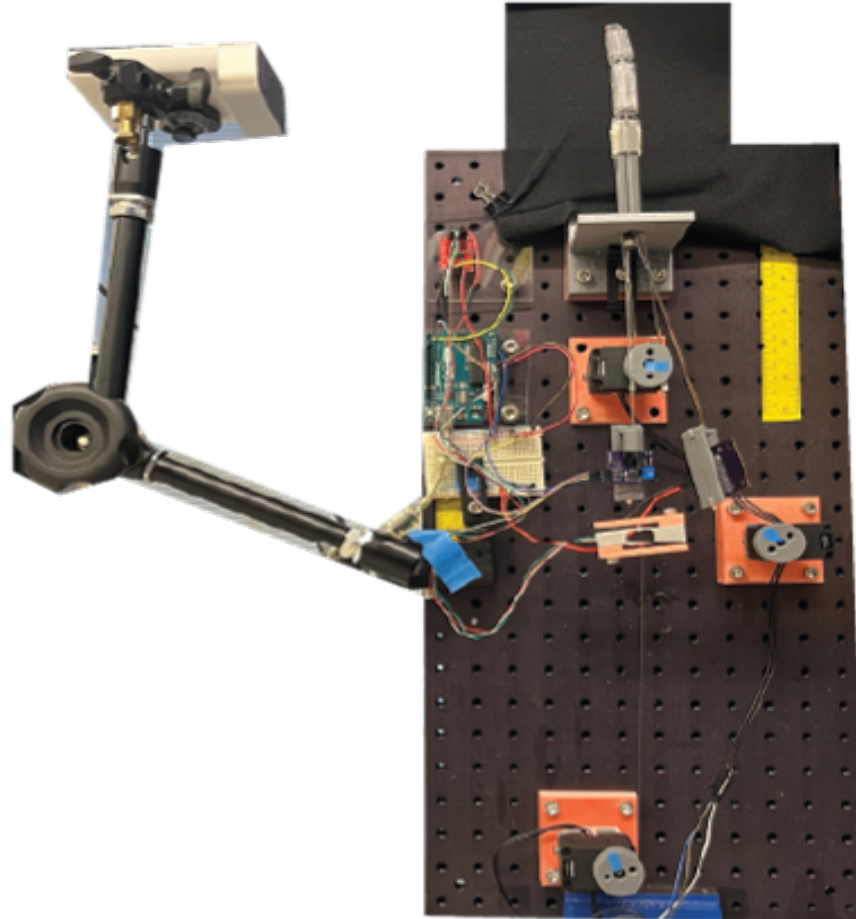
Figure 45. Experimental setup for actuating and sensing of the robotic finger

the small set of data, the output angle can be trained with 3 inputs of flexor, extensor displacement, and light intensity ratio. The training division setup is 70% of total data for training, and 30% for the testing. The test performance gives RMSE (Root Mean Square Error) 1.1705 degrees and the regression correlation number R is 0.99926. Then, for identifying system repeatability and gathering more data sets, Figure 47 shows the same motion of the finger in the different testing. While the data set gets bigger and has a certain range of initial tendon force (1-1.5N), the RMSE (2.3593 degrees) becomes slightly higher than the previous. The R value is still close to 1, which is 0.99762 for the total data set. So, based on the last trained regression function from 3 training sets, another test set data can be verified to see how well the function estimates the output angle. In Figure 48, although the estimation is not
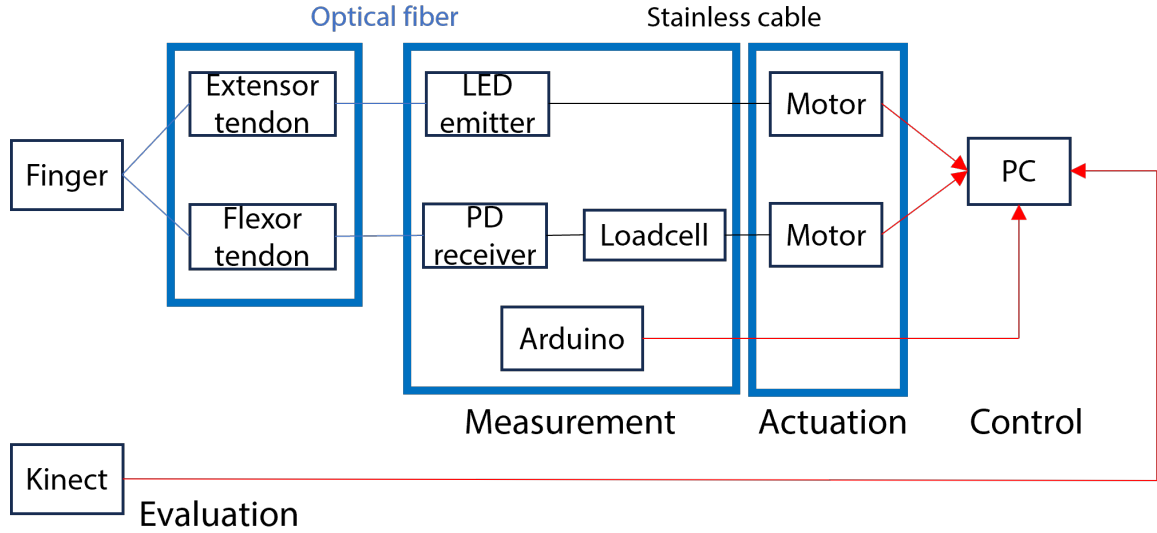
Figure 46. Diagram of hardware integration

as close as the training test sets, it still shows that the estimation result follows the real value in a certain range of error, which has 5.6861 degree RMSE.

6 Discussion

In this project, we developed a novel design of a robotic finger system that draws inspiration from the structure of the human finger. This design offers several compelling advantages. Firstly, our finger is capable of self-estimating its motion, measuring total joint bending through the use of soft and flexible optical fiber tendons. These tendons not only facilitate force transmission but also serve as a means of tracking finger motion. Secondly, our approach relies on readily available off-the-shelf materials and utilizes only a single sensor fiber to enable total three-joint motion within a finger. This not only enhances cost-efficiency but also makes the system easily implementable. Thirdly, with an initial calibration process, the finger can be controlled with minimal processing load, further enhancing its usability.

However, it is essential to acknowledge that while our system design excels in terms of simplicity and compactness, there is still room for improvement. One aspect is
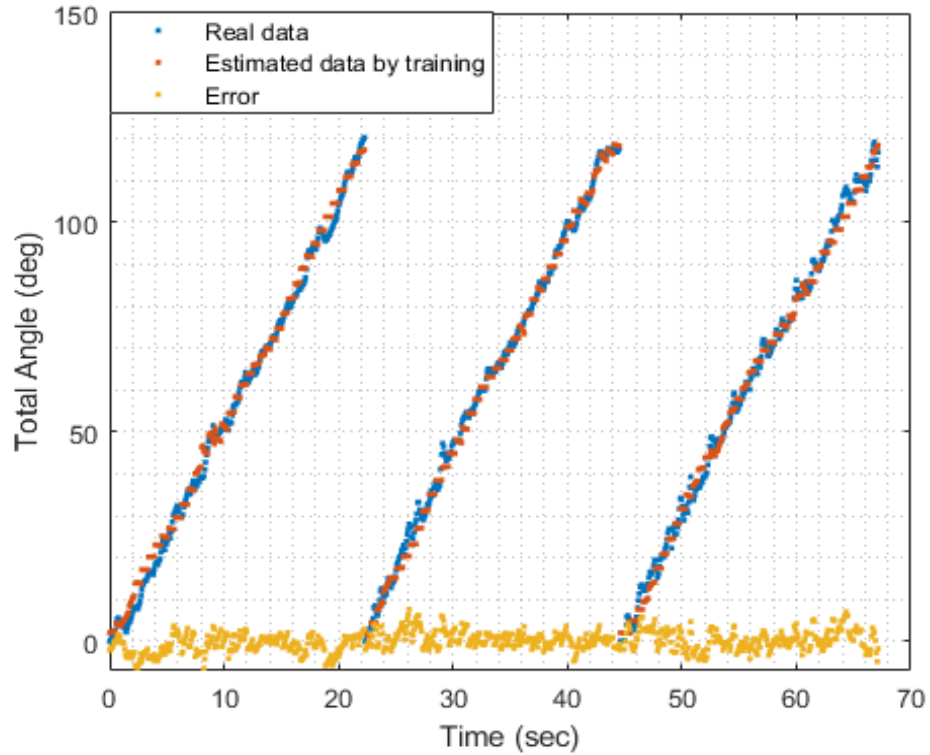
Figure 47. Test training data results in specific initial tendon force region of 1-1.5N

that the reliance on pre-trained sensor data based on specific initial configurations may limit its adaptability. To address this, future work should focus on gathering a more extensive and diverse dataset to enhance the system's flexibility. Additionally, considering that our project primarily operated in a static state without external forces, future research should prioritize integrating force dynamics to not only mimic human-like motion but also facilitate interactions with external inputs.

In conclusion, our robotic finger system represents a significant step forward in the field of robotic manipulation. Its innovative blend of soft and rigid materials, cost-efficiency, and ease of control make it a promising platform for future applications. As we continue to refine and expand our research, we aim to bridge the remaining gaps, ensuring that our system remains adaptable and robust in various scenarios.
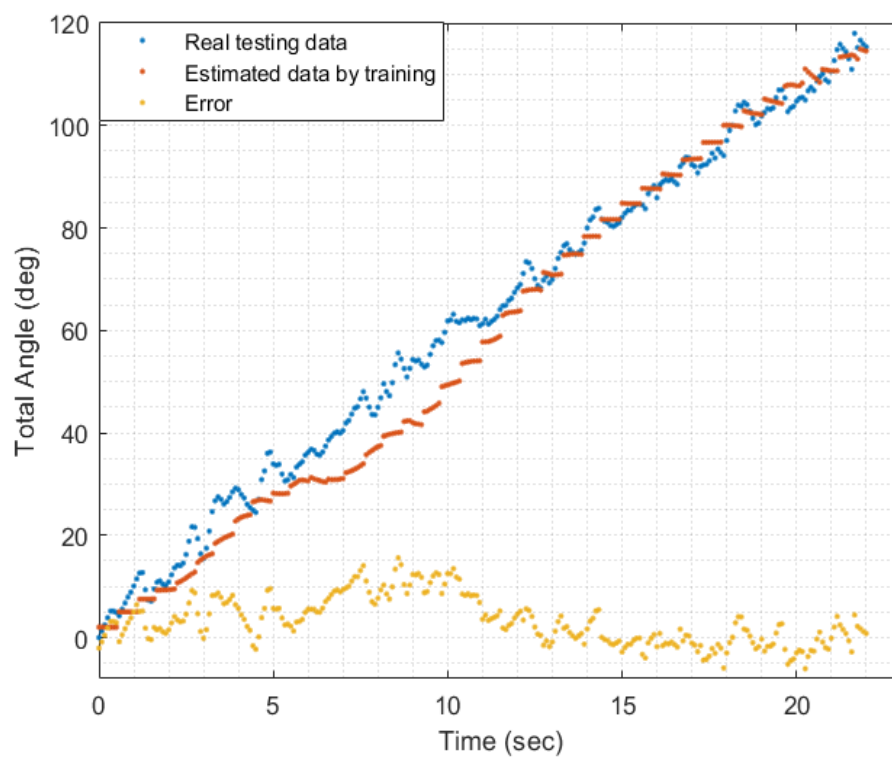
Figure 48. Estimation of the bending angle from the previously trained net function

CHAPTER VI

INTEGRATION OF TOUCH SENSING
WITH THE ROBOTIC FINGER

1 Motivation

Previous chapters have delved into the analysis of finger motion both mathematically and empirically. Additionally, manipulator posture has been examined using vision camera sensors and mapped using neural network techniques based on image data and optical sensing results.

Given the demonstrated potential of utilizing optical fiber for posture measurement by observing its bending effect, exploring other forms of physical deformation to gauge the fiber's sensing capability within the manipulator becomes pertinent. As emphasized earlier, tactile information plays a crucial role in navigating peripheral situations. Therefore, it is natural to contemplate how integrating optical fiber-embedded fingers can facilitate touch information observation. Thus, the central idea of this work revolves around integrating tendon measurement with manipulator motion to not only overcome spatial limitations but also enhance system control convenience.

This chapter undertakes a geometrical analysis of ray optics under various deforming shapes. Furthermore, it explores how these shapes are influenced by applied forces depending on the fiber's physical properties. To assess sensing reliability, a soft tip-integrated manipulator is utilized, presenting data observations across several postures with varying degrees of contact softness. Finally, a simple application example is demonstrated, showcasing the maintenance of constant contact force.

2 Geometrical Optics

Due to the innervated optical fiber tendon, the finger manipulator can detect its motion change that causes physical deformation of the fiber. Although mathematical and physics backgrounds of light attenuation are already stated in many optics theories [161, 163], it is too complicated to use its exact model in the system. However, we can estimate its approximate value according to the geometrical variations of the waveguide through the Finite Element Analysis(FEA) tool. Basically, given some possible scenarios especially for the developed finger manipulator system, it is able to see how the light transmittance rate changes depending on the manipulator motion or applied force.

2.1 Bending Property

In the developed manipulator, the fiber is affected by its motion directly. In that manner, bending is the most dominant deformation in this system. Generally, light loss caused by bending effect is increased as the radius of curvature is decreased [161]. Therefore, the results from the simulation in Figure 49 and 50 shows reasonable transmittance rate from input to output. Each bending position is each joint position of the manipulator. Also the maximum bending angles follow the designed manipulator dimension, which are 80°(MCP), 70°(PIP) and, 70°(DIP), respectively. Then, we can easily calculate the bending radius based on the arc length formula as follows:

$$r = \frac{180 l_A}{\pi \theta_A} \tag{34}$$

where l_A and θ_A are the fixed arc length at each joint position and angle degree of the curvature.
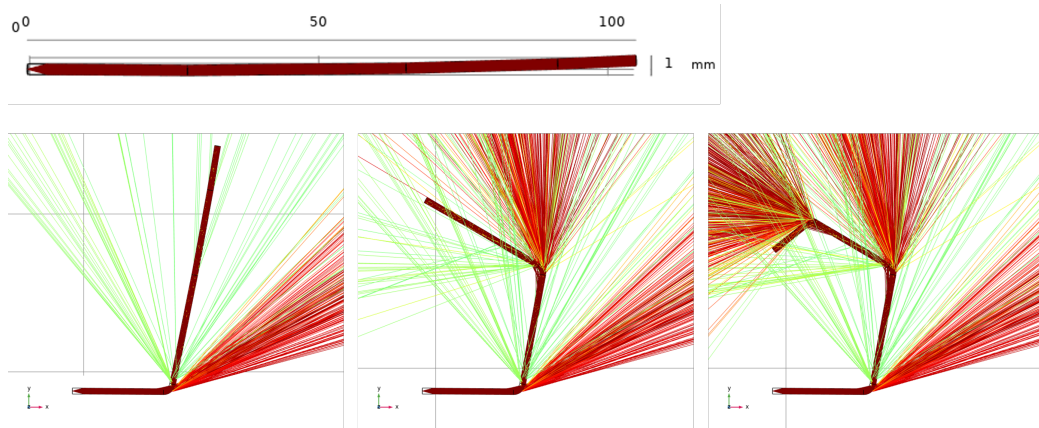
Figure 49. Bending ray scattering at different local positions in one fiber body.
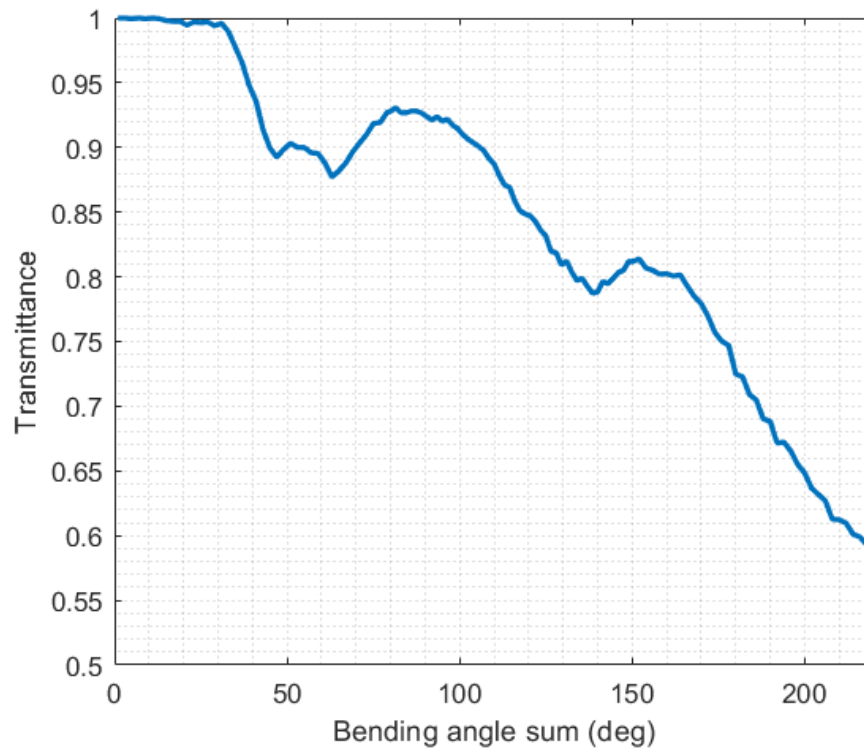
Figure 50. Light transmittance according to the total bending angle of the fiber. Maximum angles of MCP, PIP, DIP are 80°, 70° and, 70° respectively.

2.2 Elongation

Since the fiber is flexible and somewhat stretchable, the elongation property also can be considered. Although our manipulator is unlikely to be subjected to excessive tensile force, it can be estimated how much elongation affects to the light attenuation

numerically. Based on the physical tensile testing, it is found that the fiber material has around 168.5 MPa Young's Modulus. Furthermore, if we take the Poisson's ratio(ν) of Polyurethane material($\cong 0.4$) [164], transverse direction strain is able to be calculated according to the axial strain as well.

$$\nu = -\frac{d\varepsilon_{trans}}{d\varepsilon_{axial}} \tag{35}$$

Figure 52 shows that 2 mm elongation is associated with almost 30% light loss from the source. The amount 2 mm can be generated from more than 28 N, however, the manipulator's tendon force lies under 5 N at most. So, that being said the elongation is more likely to affect to the light transmittance by less than 15% loss assuming less than 1 mm elongation.
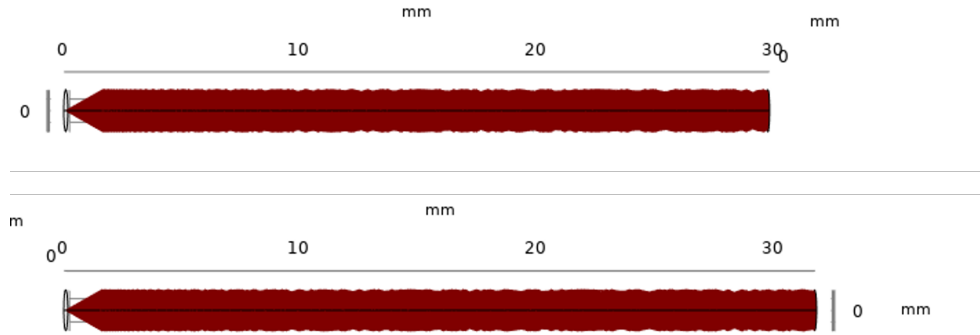
Figure 51. Illustration of fiber elongation ray transmission.

2.3   Pinching Property

The tendon fiber covers up the finger back side and inner side in this manipulator. Also, because it is required to have inlet and outlet for receiving and sending light source, the fiber makes the u-turn at the finger tip position. The reason to examine the pinching property is to figure out if contact touching on the tip can be discerned. So, the hard plastic tip of the previous chapter is substituted with a soft silicone material which includes a small indenter at the fiber-turning position to amplify
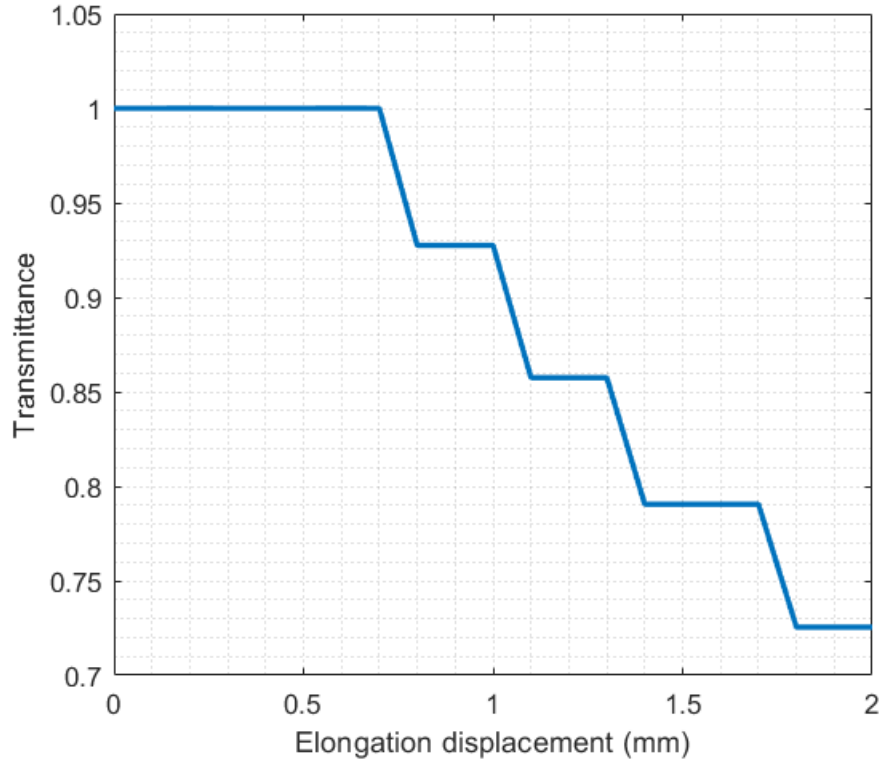
Figure 52. Light transmittance rate vs. elongation length. Initial length of the fiber is 30 mm. It is assumed that when the tensile force is around 28 N, it is stretched by around 2 mm based on the mechanical testing results(Young's Modulus, 168.5 MPa).

physical deformation of the fiber. The fiber path and indenter on the finger tip is shown in Figure 53, 54. Thus, it is expected that the indenter presses the fiber when the contact force affects directly to the silicone by suppressing. In that case, how much displacement would happen under certain range of pressing force can be presumed through the simulation. Figure 55 presents that 0.01 mm displacement in z-axis when the loading force on the both side 0.1 N. However, what eventually we want to identify is how the light attenuation will be with respect to this mechanical deformation. Thereby simplifying the physical deformation, optical ray tracing is able to be observed numerically. Like Figure 54, it is assumed that the loading force is applied on the arrow points and leads to elliptical cross-sectional shape from the circle. Then the simulation result shows around 10% loss for 0.1 mm change in the

fiber radius.
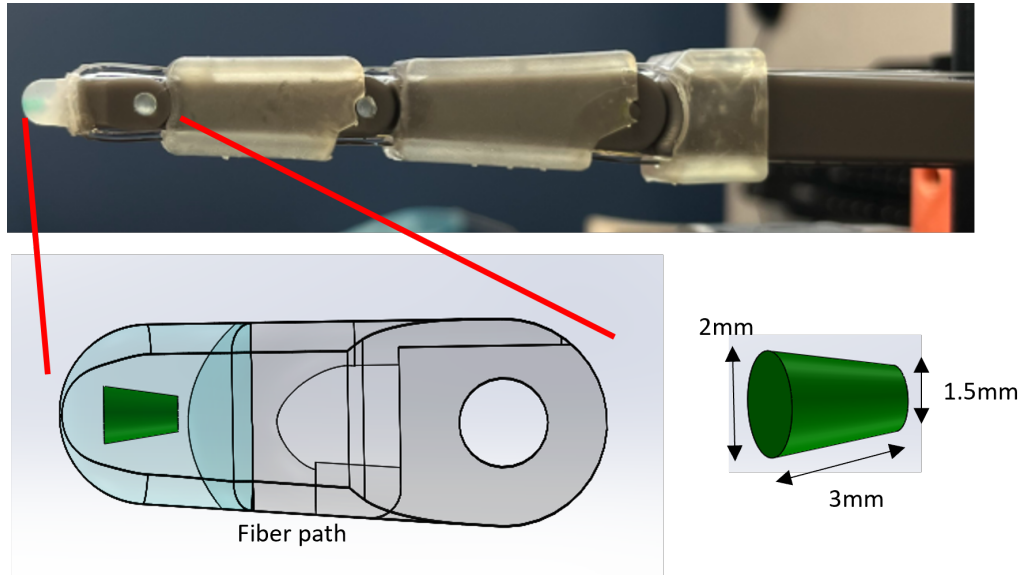
Figure 53. Distal silicon pad(DragonSkin, SmoothOn Inc.) tip design for detecting contact force. The left bottom figure shows cross-sectional view of the distal link.
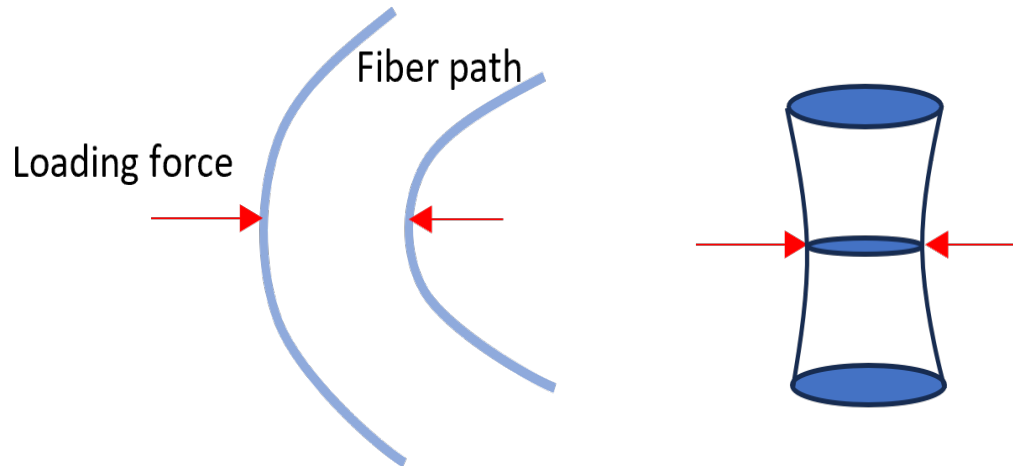
Figure 54. Illustrations of force loading on the fiber path in the distal tip. The right figure represents a speculation of fiber shape deformation on infinitesimal length with transverse loading force.

3 Hardware Implementation

As shown in Figure 60, the test bed consists of three motors (Dynamixel XL430, Robotis Inc.) for driving the manipulator and linear stage to measure the contact
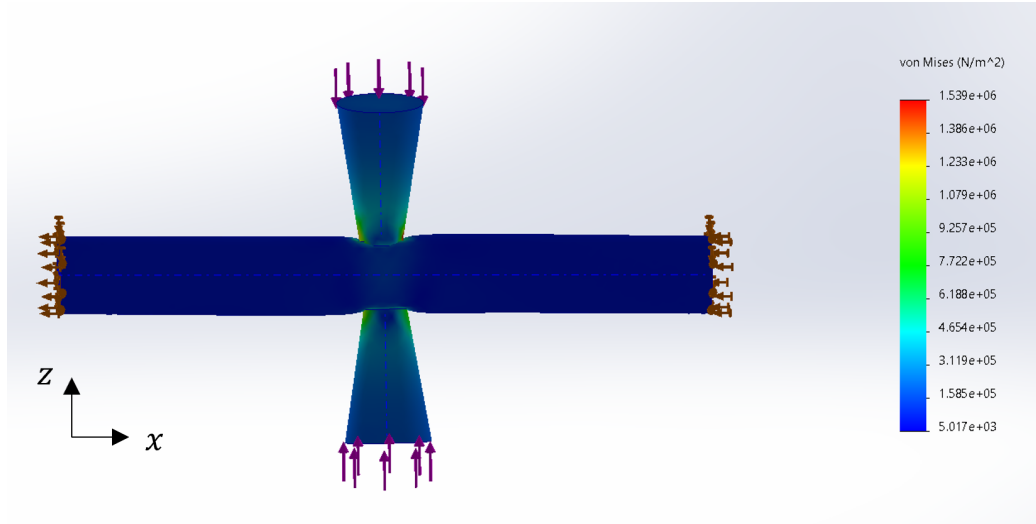
Figure 55. Transverse force loading simulation(SolidWorks). The indenter's diameter is 1 mm and presses the fiber from both sides with 0.1 N.
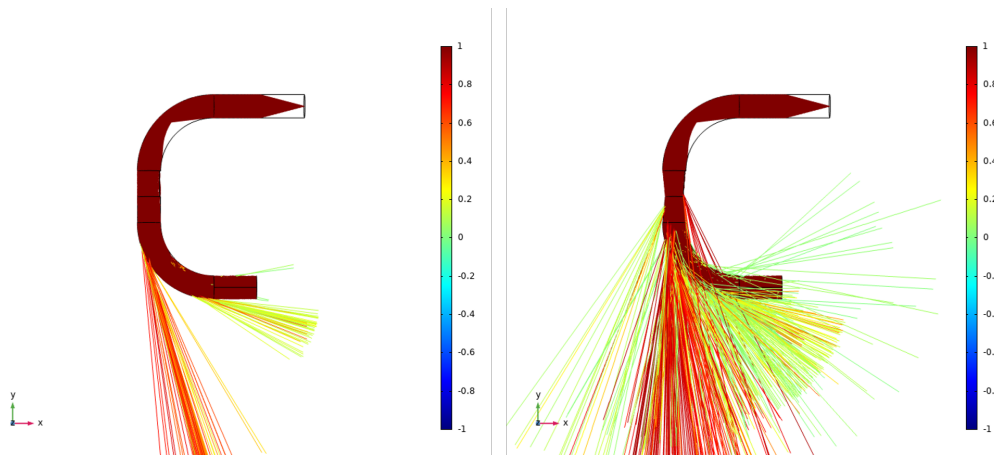
Figure 56. Pinching on the bending fiber.

force. Two loadcells are located on the backside of the touching surface and connected to the loadcell amplifier. Light sensor components are emitter(LED) and receiver(Photodiode) board directly connected to the each fiber end to measure the light traveling in it. Every sensor signal comes to Arduino Uno board. Then, the arduino board and the motor connnector directly come into the main processor PC and are synchronized through the serial communication. Based on the setup of the test bed, in this section, different cases of hardware implementation are shown to verify sensor reliability.
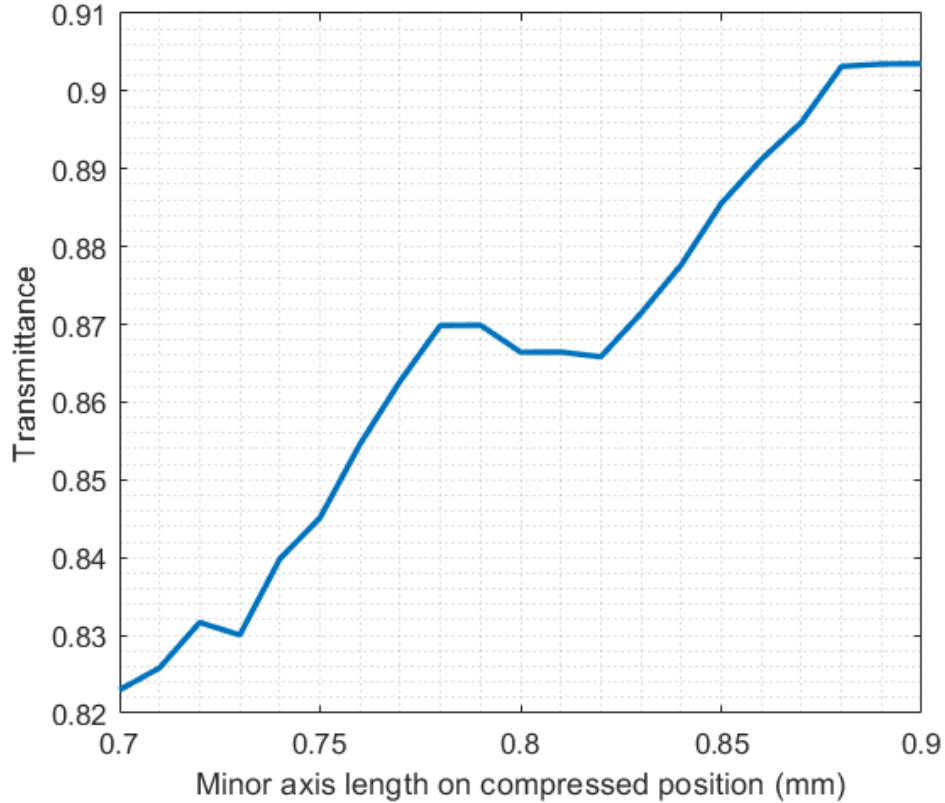
Figure 57. It is assumed that the pinching part by transverse loading force generates elliptical shape of the fiber in the cross-sectional view.

3.1 Sensor Verification

In the previous section, the physical effects of the optical fiber are presented numerically. The next task is identifying how well those results match with the real hardware implementation. Starting from the simple pressing example, contact force is applied directly to the finger tip and the light intensity variation is observed as a function of loading force.

The curved surface is designed from workspace of the manipulator to make proper contact points on the surface. The loading force is composed of 2 different axis and it is normalized taking 2-norm to see the magnitude of the total force. In this case, it is assumed that there are only 2 directional forces to consider, z and x axis (finger longitudinal axis and closing motion axis) because the lateral motion of the finger

is constrained. Then, when the linear stage approaches to the finger tip side, the contact force increases from the two loadcells since it causes a pressing motion. During the experiment, although the finger is subjected to the force, it does not affect the finger motion change. In other words, it is assumed that the force is applied to the finger tip only without impact on the finger joints. So, like the pinching effect in the previous section, one is able to see how the contact pressing force influences the tendon fiber. As shown in Figure 59, the hard surface can be more influential with less applied force than the soft surface because it has less force-dissipating buffer components between the contact surfaces. Furthermore, it also presents more steep slope in the hard surface case with respect to the relationship between the force and light intensity.

When the bending effect is added up with the tip pressing, the result becomes slightly different. As one can see in Figures 60, 61 and 62, with more applied force, there is an approximately proportional light attenuation. In the meantime, in accordance with the joint bending angles, the initial level of the light intensity is discerned. This result also agrees with the bending loss effect from the simulation results.

Lastly, by observing the loading and unloading on the finger tip the sensitivity of the tendon measurement can be identified. During each cycle, the displacement of the moving stage is from 0 to 4 mm starting from barely contacting on the finger. While the same displacement is applied on the pressing process, the maximum loss level is slightly different. This discrepancy is caused by soft material's physical property of viscoelasticity which leads to hysteresis. Therefore, if the finger tip's silicone and the surface contact material is changed, the intensity-vs-force curve is expected to show different appearance similar to Figure 59.

3.2 Contact Force Control

Since it is identified that the finger tip press leads to indenting fiber, which directly affects light travel path and makes intensity variation mostly attenuation, the transmitted intensity may be an input for a control system that maintains a certain contact force range. So, the simple P controller is implemented to reach the target level of light attenuation. Figures 64 and 65 show that when each target attenuation is different, the resultant force also varies. The higher light loss ratio is set, the more contact force is caused which is the same results with the pinching effect and simple pressing experiments.

4 Discussion

In this chapter, the possibility is shown for the fiber sensor to measure physical deformation through numerical analysis. Especially, bending, elongation and, pinching properties are examined as plausible deformation shapes for the fiber in the manipulator developed in this thesis. According to the deformation, the attenuation presents from 10 % to 40 % loss of the light.

As far as tactile sensing is concerned, the pinching effect is most likely to happen at the tip of the finger manipulator because of the distal link and the soft tip design. Thus, the hardware implementation focuses on demonstrating touch sensing performance. When the force is applied to the different hardness of the surface, the fiber sensor is able to detect intensity of the pressure with the dissimilar value of the slope. The frequency test is also conducted to see sensor reliability by loading and unloading a certain level of force. Moreover, while the finger is subjected to the pressing force, the bending can be considered another influence by driving the finger with different joint angles. Lastly, since it is able to measure light intensity according to the exerted force, maintaining touching force of the finger could be one of the application examples. Thus retaining contact force is presented by making the system follow the

set point of the light attenuation based on the fiber sensor feedback.

Most of the experiments in this chapter are concerned with static state and segregated from different effects. So, it is necessary to verify sensor performance in more complex situations to be utilized in the real world applications. Although we can acknowledge that the fiber sensor detects the finger motion and the applied force, it still remains to identify mathematical or numerical mapping between the fiber sensing feedback and the motion that we want to sense. Therefore, in future works, dynamical situations and finding the intuitive relationship function should be considered to make the system more practical.
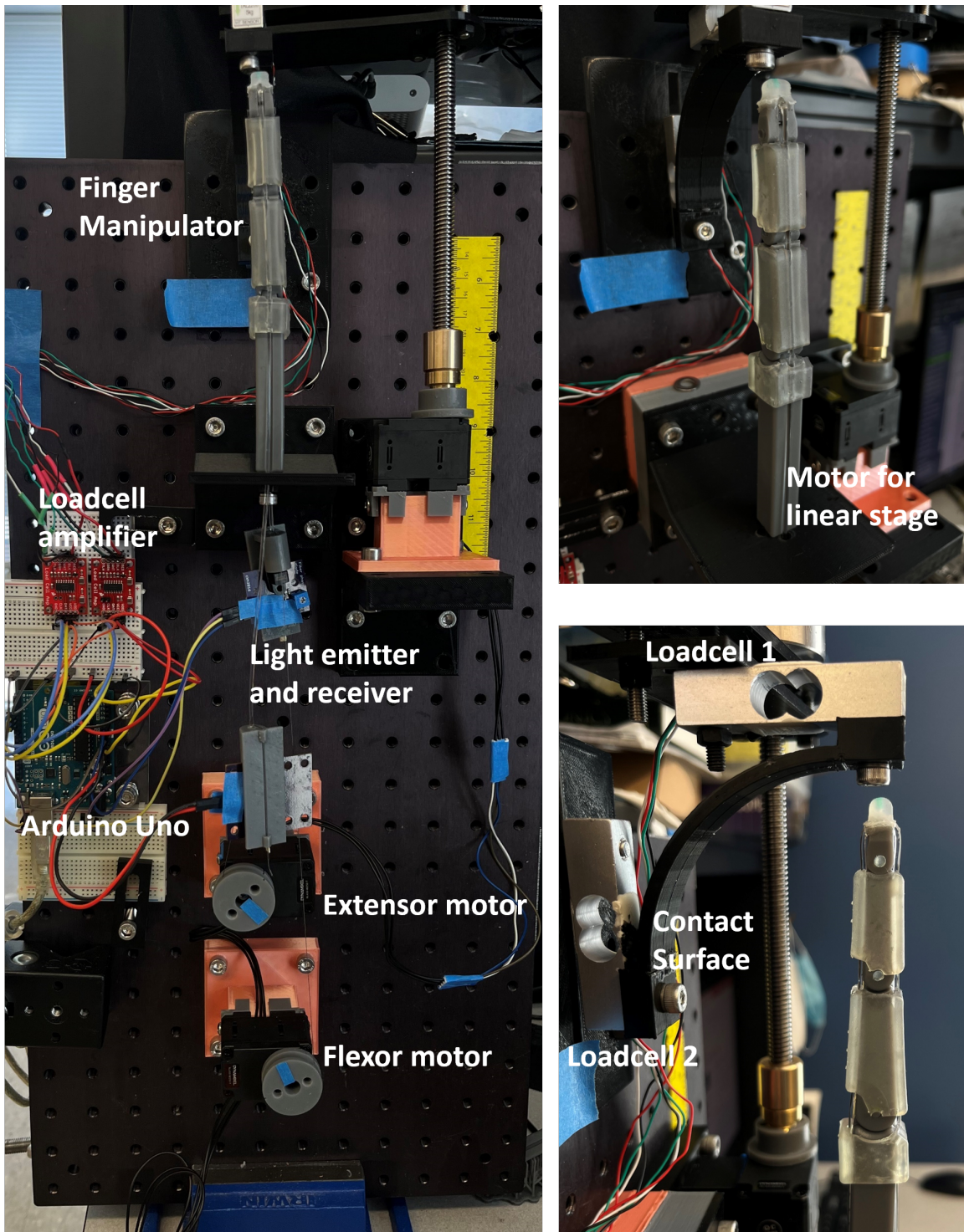
Figure 58. Testbed setup : The index finger manipulator is demonstrated to show tactile sensing performance.
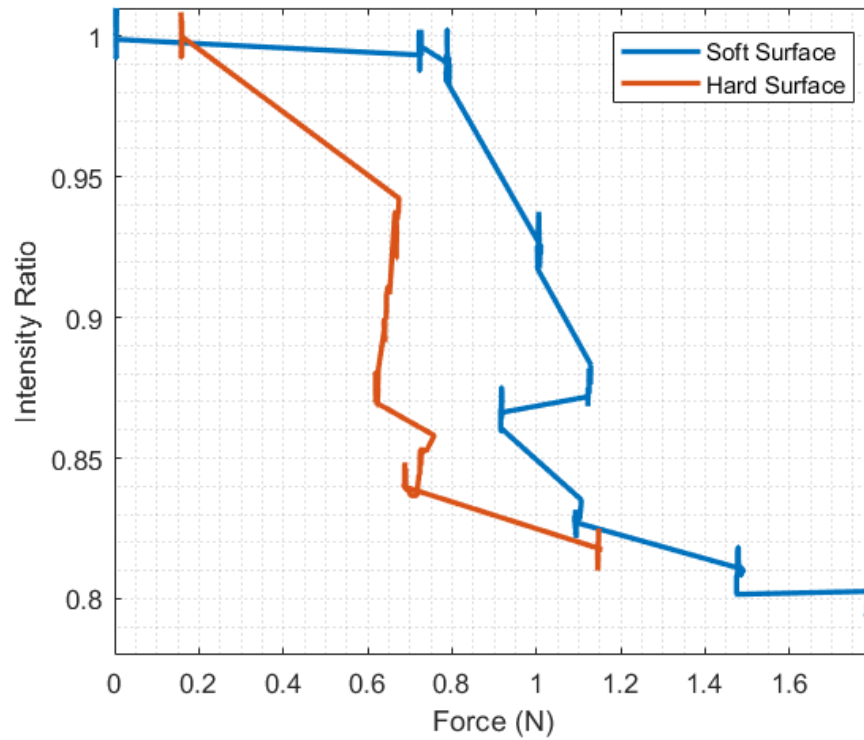
Figure 59. Contact pressing motion on soft(SkinTite, silicone) and hard(PLA) material surface.
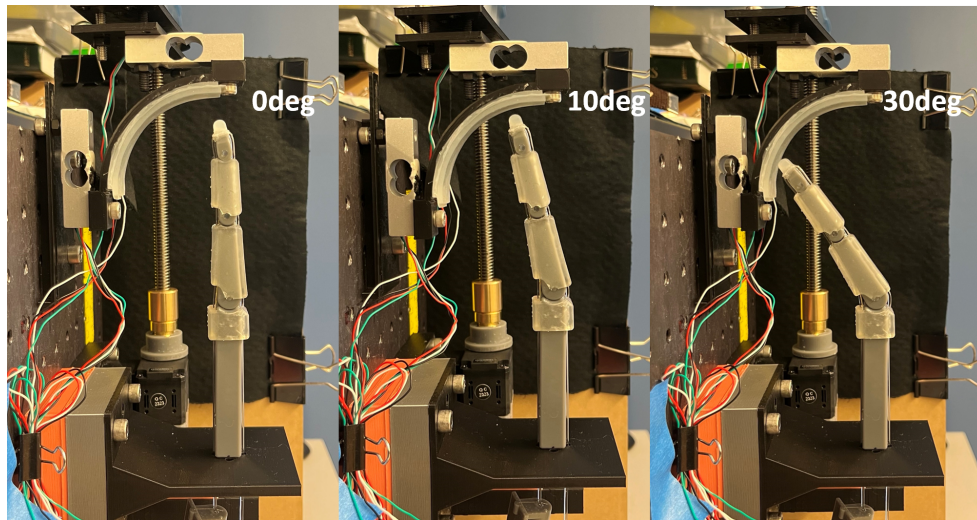
Figure 60. Contact surface experiment with the soft pad on the surface. Different postures (MCP 0°, 10°, 30°) are tested.
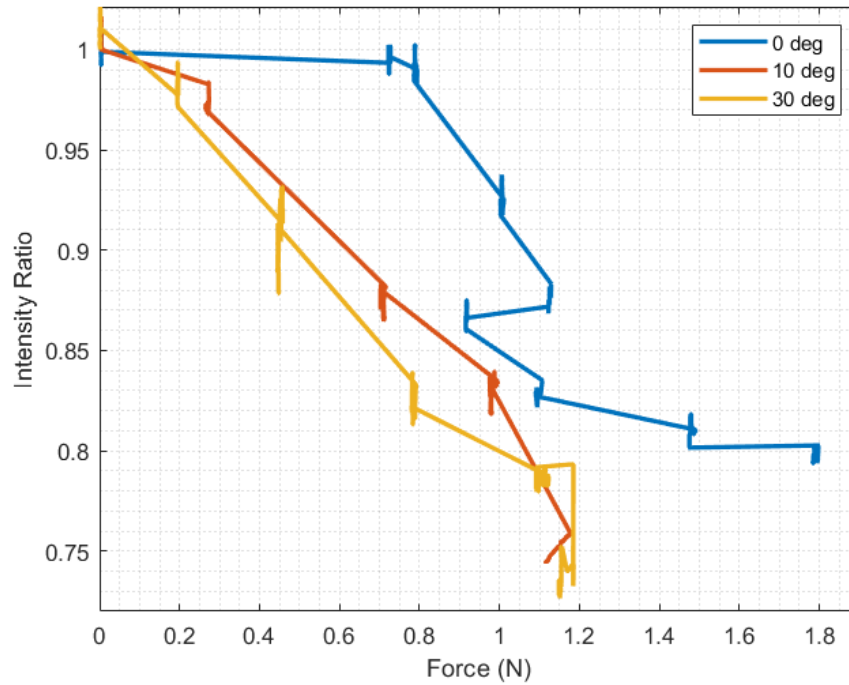
Figure 61. Force vs. light transmittance rate in different postures with the soft material surface.
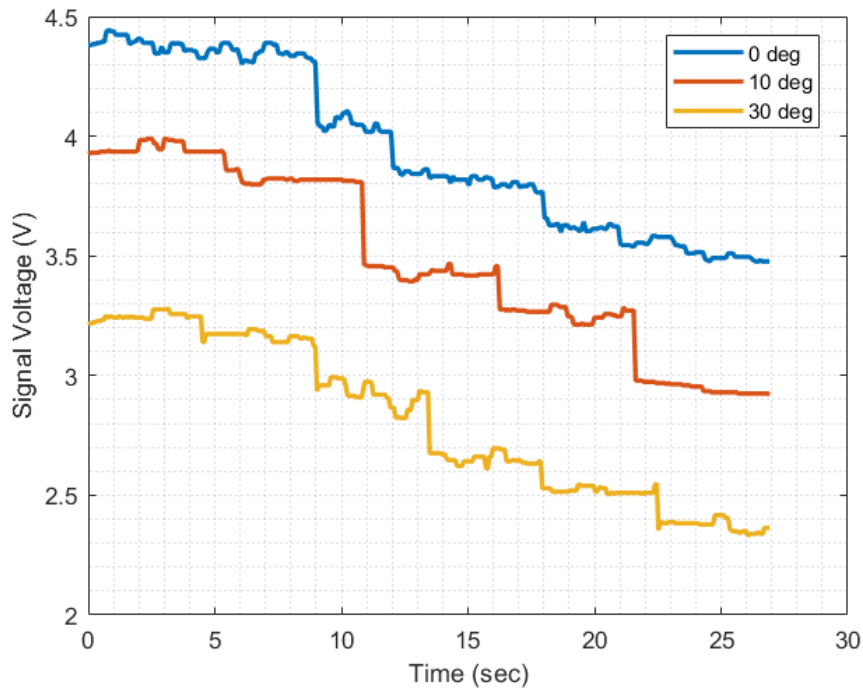
Figure 62. Analog voltage level according to different postures.
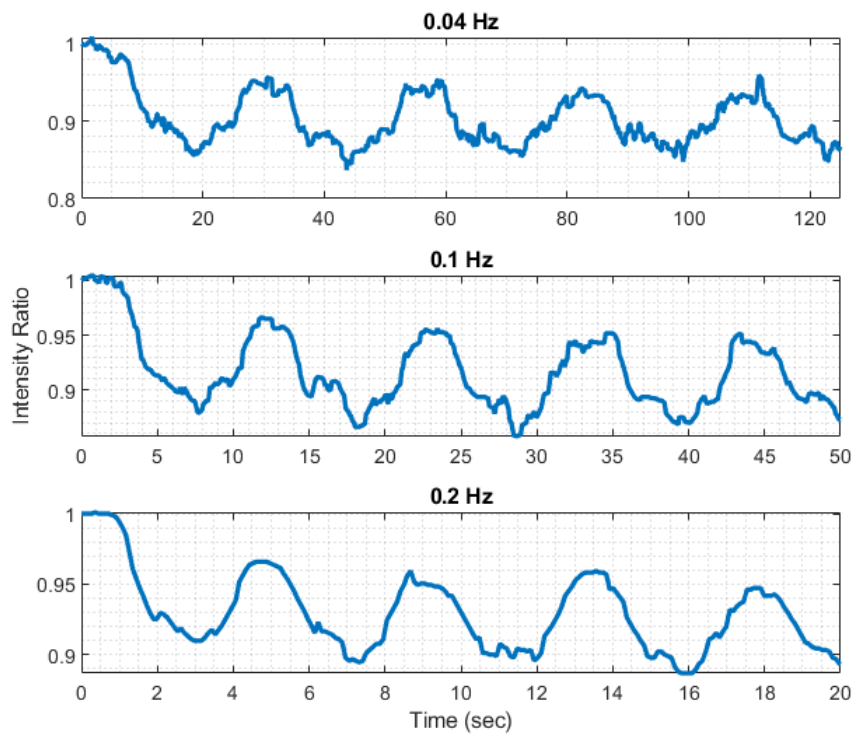
Figure 63. Loading and unloading cycle in the same posture of the finger with the different frequencies of 0.04 Hz, 0.1 Hz and, 0.2 Hz.
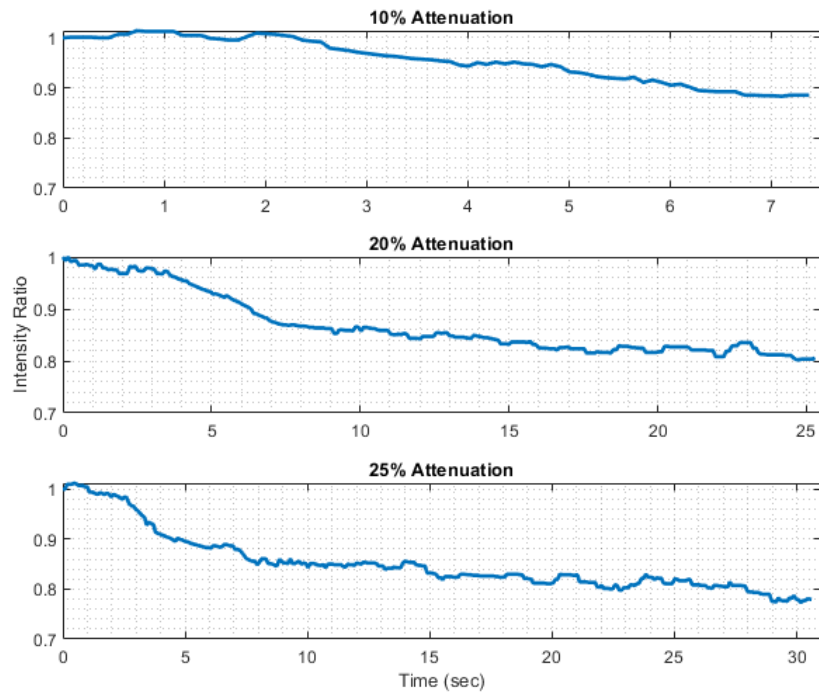
Figure 64. Application experiment for maintaining contact force. Each target attenuation is 10%, 20%, 25%.
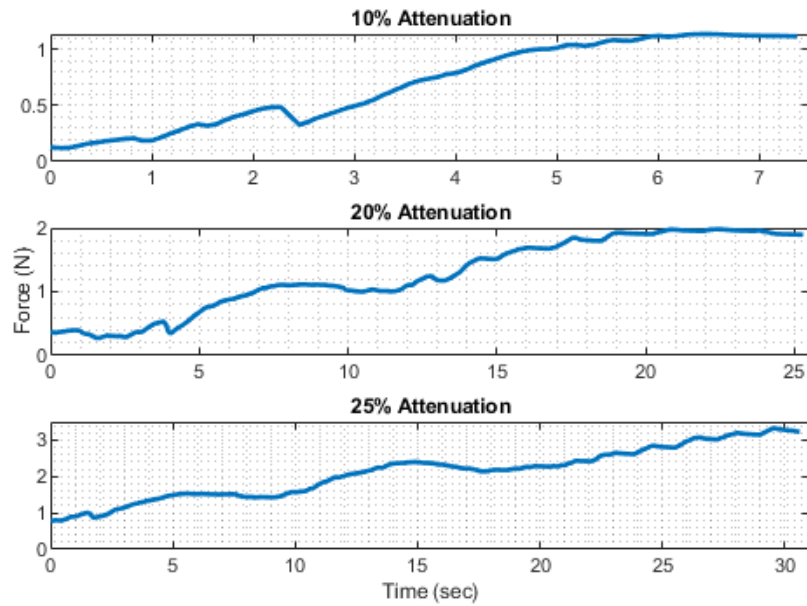
Figure 65. Force measurement result according to maintaining the target intensity level.

91

CHAPTER VII

CONCLUSION AND FUTURE WORKS

This dissertation encompasses significant contributions and objectives across 6 chapters.

In Chapter 1, it highlights the development of a novel bristle-based sensor capable of measuring normal and lateral forces during stick-slip motion. The sensor demonstrates promising physical performance across different experiments like normal force exerting, sensitivity, hysteresis tests etc. suggesting its viability for applications in robot grasping.

Based on the development of sensor in Chapter 1, Chapter 2 introduces an adaptive grasping control system. The system exhibits robust performance in simulation and hardware experiments, though there is room for future exploration in handling diverse grasping objects.

On the other hand, Chapter 3 shows a broader context, discussing advancements in biomimetic hands and the ongoing challenges in design, fabrication, and control. Thereby providing a comprehensive overview of anthropomorphic manipulators, it is able to lay the groundwork for the future developments. While progress has been made, there still remains a need for integrated approaches that leverage emerging technologies to enhance robotic manipulators.

In Chapter 4, we delved into the development of a robotic manipulator emphasizing the importance of understanding its mechanisms and dynamics. By exploring the mathematical simulations, the background of the finger manipulator control system is provided.

Chapter 5 presents a novel robotic finger system design capable of self-estimating its joint bending angle based on the optical tendon fibers. While the system offers simplicity and cost-efficiency, there are opportunities for improvements, particularly in adaptability and dynamics interactions.

With Chapter 3's overview, Chapter 4's foundation, and Chapter 5's novel design, in Chapter 6, the potential of the tendon fiber sensor for measuring physical deformation and tactile sensing is explored further. It shows promising results in different static situations especially pressing and bending. However, further research is needed to validate sensor performance in real-world applications and establish intuitive mapping between sensor feedback and desired motion.

In conclusion, this work's findings emphasize the ongoing evolution and potential of robotic manipulation and tactile sensing. Especially, by utilizing the optical fibers' sensing technique, it has streamlined system complexity and enhanced design flexibility.While this work presents innovative and straightforward systems, the future research efforts should focus on addressing remaining challenges, such as adaptability, dynamic interactions, and real-world applicability. Specifically, the physical limitations of optical fibers may impact sensing performance due to factors like light degradation or material fatigue. Additionally, it's crucial to examine the physical properties of other components, such as sheaths and bones. On the design front, certain aspects of human finger anatomy have been sacrificed in the realization of robotic finger manipulators to simplify the system. Addressing these issues will propel the field forward and facilitate practical implementations.

REFERENCES

[1]   V. G. Macefield, I. Birznieks, M. D. Binder, N. Hirokawa, and U. Windhorst, "Cutaneous mechanoreceptors, functional behaviour," Encyclopedia of neuroscience (2009).

[2]   B. A. Carlson, The human body: linking structure and function (Academic Press, 2018).

[3]   G. Li, S. Liu, L. Wang, and R. Zhu, "Skin-inspired quadruple tactile sensors integrated on a robot hand enable object recognition," Science Robotics **5**, eabc8134 (2020).

[4]   B. C.-K. Tee, A. Chortos, A. Berndt, A. K. Nguyen, A. Tom, A. McGuire, Z. C. Lin, K. Tien, W.-G. Bae, H. Wang et al., "A skin-inspired organic digital mechanoreceptor," Science **350**, 313–316 (2015).

[5]   P. Roberts, M. Zadan, and C. Majidi, "Soft tactile sensing skins for robotics," Current Robotics Reports **2**, 343–354 (2021).

[6]   Y. Wan, Y. Wang, and C. F. Guo, "Recent progresses on flexible tactile sensors," Materials Today Physics **1**, 61–73 (2017).

[7]   M. M. Iskarous and N. V. Thakor, "E-Skins: Biomimetic sensing and encoding for upper limb prostheses," Proc. IEEE **107**, 2052–2064 (2019).

[8]   B. Ward-Cherrier, N. Pestell, L. Cramphorn, B. Winstone, M. E. Giannaccini, J. Rossiter, and N. F. Lepora, "The TacTip family: Soft optical tactile sensors with 3D-Printed biomimetic morphologies," Soft Robot **5**, 216–227 (2018).

[9]   J. W. James, N. Pestell, and N. F. Lepora, "Slip detection with a biomimetic tactile sensor," IEEE Robotics and Automation Letters **3**, 3340–3346 (2018).

[10]   C. M. Boutry, M. Negre, M. Jorda, O. Vardoulis, A. Chortos, O. Khatib, and Z. Bao, "A hierarchically patterned, bioinspired e-skin able to detect the direction of applied pressure for robotics," Science Robotics **3**, eaau6914 (2018).

[11]   M. S. Han and C. K. Harnett, "Soft, all-polymer optoelectronic tactile sensor for stick-slip detection," Advanced Materials Technologies **7**, 2200406 (2022).

[12]   R. Zhang, J.-T. Lin, O. O. Olowo, B. P. Goulet, B. Harris, and D. O. Popa, "Skincell: A modular tactile sensor patch for physical human–robot interaction," IEEE Sensors Journal **23**, 2833–2846 (2022).

[13] Z. Shen, X. Zhu, C. Majidi, and G. Gu, "Cutaneous ionogel mechanoreceptors for soft machines, physiological sensing, and amputee prostheses," Advanced Materials **33**, 2102069 (2021).

[14] Y. Liu, S. Cui, J. Wei, H. Li, J. Hu, S. Chen, Y. Chen, Y. Ma, S. Wang, and X. Feng, "Centrosymmetric-and axisymmetric-patterned flexible tactile sensor for roughness and slip intelligent recognition," Advanced Intelligent Systems **4**, 2100072 (2022).

[15] C.-A. Bunge, M. Beckers, and B. Lustermann, "Basic principles of optical fibres," in "Polymer Optical Fibres," (Elsevier, 2017), pp. 47–118.

[16] B. Ward-Cherrier, N. Pestell, L. Cramphorn, B. Winstone, M. E. Giannaccini, J. Rossiter, and N. F. Lepora, "The tactip family: Soft optical tactile sensors with 3d-printed biomimetic morphologies," Soft robotics **5**, 216–227 (2018).

[17] W. Yuan, S. Dong, and E. H. Adelson, "Gelsight: High-resolution robot tactile sensors for estimating geometry and force," Sensors **17**, 2762 (2017).

[18] M. Lambeta, P.-W. Chou, S. Tian, B. Yang, B. Maloon, V. R. Most, D. Stroud, R. Santos, A. Byagowi, G. Kammerer et al., "Digit: A novel design for a low-cost compact high-resolution tactile sensor with application to in-hand manipulation," IEEE Robotics and Automation Letters **5**, 3838–3845 (2020).

[19] R. Bhirangi, T. Hellebrekers, C. Majidi, and A. Gupta, "Reskin: versatile, replaceable, lasting tactile skins," arXiv preprint arXiv:2111.00071 (2021).

[20] A. Pal, V. Restrepo, D. Goswami, and R. V. Martinez, "Exploiting mechanical instabilities in soft robotics: control, sensing, and actuation," Advanced Materials **33**, 2006939 (2021).

[21] C. Jiang, Z. Zhang, J. Pan, Y. Wang, L. Zhang, and L. Tong, "Finger-skin-inspired flexible optical sensor for force sensing and slip detection in robotic grasping," Advanced Materials Technologies **6**, 2100285 (2021).

[22] H. Zhao, K. O'Brien, S. Li, and R. F. Shepherd, "Optoelectronically innervated soft prosthetic hand via stretchable optical waveguides," Science Robotics **1** (2016).

[23] P. A. Xu, A. K. Mishra, H. Bai, C. A. Aubin, L. Zullo, and R. F. Shepherd, "Optical lace for synthetic afferent neural networks," Sci Robot **4** (2019).

[24] C. Jiang, Z. Zhang, J. Pan, Y. Wang, L. Zhang, and L. Tong, "Finger-skin-inspired flexible optical sensor for force sensing and slip detection in robotic grasping," Adv. Mater. Technol. p. 2100285 (2021).

[25] H. Bai, S. Li, J. Barreiros, Y. Tu, C. R. Pollock, and R. F. Shepherd, "Stretchable distributed fiber-optic sensors," Science **370**, 848–852 (2020).

[26] L. Massari, E. Schena, C. Massaroni, P. Saccomandi, A. Menciassi, E. Sinibaldi, and C. M. Oddo, "A Machine-Learning-Based approach to solve both contact location and force in soft material tactile sensors," Soft Robot **7**, 409–420 (2020).

[27] J.-T. Lin and C. Harnett, "Absolute length sensor based on time of flight in stretchable optical fibers," IEEE Sensors Letters pp. 1–1 (2020).

[28] S. Li, Y. Zhang, Y. Wang, K. Xia, Z. Yin, H. Wang, M. Zhang, X. Liang, H. Lu, M. Zhu, H. Wang, X. Shen, and Y. Zhang, "Physical sensors for skin-inspired electronics," InfoMat **2**, 184–211 (2020).

[29] J. Guo, X. Liu, N. Jiang, A. K. Yetisen, H. Yuk, C. Yang, A. Khademhosseini, X. Zhao, and S.-H. Yun, "Highly stretchable, strain sensing hydrogel optical fibers," Adv. Mater. **28**, 10244–10249 (2016).

[30] C. K. Harnett, H. Zhao, and R. F. Shepherd, "Stretchable optical fibers: Threads for Strain-Sensitive textiles," Adv. Mater. Tech. (2017).

[31] A. Leber, B. Cholst, J. Sandt, N. Vogel, and others, "Stretchable thermoplastic elastomer optical fibers for sensing of extreme deformations," Adv. Funct. Mater. (2019).

[32] J. Guo, B. Zhou, C. Yang, Q. Dai, and L. Kong, "Stretchable and Temperature-Sensitive polymer optical fibers for wearable health monitoring," Adv. Funct. Mater. **29**, 1902898 (2019).

[33] E. Nseowo Udofia and W. Zhou, "3D printed optics with a soft and stretchable optical material," Additive Manufacturing **31**, 100912 (2020).

[34] B. Jamil, G. Yoo, Y. Choi, and H. Rodrigue, "Proprioceptive soft pneumatic gripper for extreme environments using hybrid optical fibers," IEEE Robotics and Automation Letters pp. 1–1 (2021).

[35] J. Guo, C. Yang, Q. Dai, and L. Kong, "Soft and stretchable polymeric optical Waveguide-Based sensors for wearable and biomedical applications," Sensors **19** (2019).

[36] W. Chen, H. Khamis, I. Birznieks, N. F. Lepora, and S. J. Redmond, "Tactile sensors for friction estimation and incipient slip Detection—Toward dexterous robotic manipulation: A review," IEEE Sens. J. **18**, 9049–9064 (2018).

[37] H. Oh, G.-C. Yi, M. Yip, and S. A. Dayeh, "Scalable tactile sensor arrays on flexible substrates with high spatiotemporal resolution enabling slip and grip for closed-loop robotics," Sci. Adv. **6**, eabd7795 (2020).

[38] Y. Liu, S. Cui, J. Wei, H. Li, J. Hu, S. Chen, Y. Chen, Y. Ma, S. Wang, and X. Feng, "Centrosymmetric- and axisymmetric-patterned flexible tactile sensor for roughness and slip intelligent recognition," Advanced Intelligent Systems p. 2100072 (2021).

[39] B. Ward-Cherrier, N. Pestell, L. Cramphorn, B. Winstone, M. E. Giannaccini, J. Rossiter, and N. F. Lepora, "The TacTip family: Soft optical tactile sensors with 3D-Printed biomimetic morphologies," Soft Robot **5**, 216–227 (2018).

[40] M. Ohka, J. Takata, H. Kobayashi, H. Suzuki, N. Morisawa, and H. Yussof, "Optical three-axis tactile sensor for robotic fingers," Sensors: Focus Tactile Force Stress Sensing; InTech: Rijeka, Croatia pp. 103–122 (2008).

[41] Y. Ito, Y. Kim, and G. Obinata, "Robust slippage degree estimation based on reference update of Vision-Based tactile sensor," IEEE Sens. J. **11**, 2037–2047 (2011).

[42] B. W. McInroe, C. L. Chen, K. Y. Goldberg, K. Y. Goldberg, R. Bajcsy, and R. S. Fearing, "Towards a soft fingertip with integrated sensing and actuation," in "2018 IEEE/RSJ International Conference on Intelligent Robots and Systems (IROS)," (ieeexplore.ieee.org, 2018), pp. 6437–6444.

[43] M. K. Johnson and E. H. Adelson, "Retrographic sensing for the measurement of surface texture and shape," in "2009 IEEE Conference on Computer Vision and Pattern Recognition," (ieeexplore.ieee.org, 2009), pp. 1070–1077.

[44] S. Dong, W. Yuan, and E. H. Adelson, "Improved GelSight tactile sensor for measuring geometry and slip," in "2017 IEEE/RSJ International Conference on Intelligent Robots and Systems (IROS)," (ieeexplore.ieee.org, 2017), pp. 137–144.

[45] V. N. Dubey and R. M. Crowder, "A dynamic tactile sensor on photoelastic effect," Sens. Actuators A Phys. **128**, 217–224 (2006).

[46] C. Canudas de Wit, H. Olsson, K. J. Astrom, and P. Lischinsky, "A new model for control of systems with friction," IEEE Trans. Automat. Contr. **40**, 419–425 (1995).

[47] F. Marques, P. Flores, J. C. Pimenta Claro, and H. M. Lankarani, "A survey and comparison of several friction force models for dynamic analysis of multibody mechanical systems," Nonlinear Dyn. **86**, 1407–1443 (2016).

[48] F. Marques, Ł. Woliński, M. Wojtyra, P. Flores, and H. M. Lankarani, "An investigation of a novel LuGre-based friction force model," Mechanism and Machine Theory **166**, 104493 (2021).

[49] J.-T. Lin, C. Newquist, and C. K. Harnett, "Multitouch pressure sensing with soft optical time-of-flight sensors," IEEE Trans. Instrum. Meas. pp. 1–8 (2022).

[50] I. Van Meerbeek, C. De Sa, and R. Shepherd, "Soft optoelectronic sensory foams with proprioception," Science Robotics **3**, eaau2489 (2018).

[51] H. Oh, G.-C. Yi, M. Yip, and S. A. Dayeh, "Scalable tactile sensor arrays on flexible substrates with high spatiotemporal resolution enabling slip and grip for closed-loop robotics," Science advances **6**, eabd7795 (2020).

[52] C. M. Boutry, M. Negre, M. Jorda, O. Vardoulis, A. Chortos, O. Khatib, and Z. Bao, "A hierarchically patterned, bioinspired e-skin able to detect the direction of applied pressure for robotics," Sci Robot **3** (2018).

[53] T. Hellebrekers, N. Chang, K. Chin, M. J. Ford, O. Kroemer, and C. Majidi, "Soft magnetic tactile skin for continuous force and location estimation using neural networks," IEEE Robotics and Automation Letters **5**, 3892–3898 (2020).

[54] Y. Yan, Z. Hu, Z. Yang, W. Yuan, C. Song, J. Pan, and Y. Shen, "Soft magnetic skin for super-resolution tactile sensing with force self-decoupling," Science Robotics **6**, eabc8801 (2021).

[55] N. F. Lepora, "Soft biomimetic optical tactile sensing with the tactip: A review," IEEE Sensors Journal **21**, 21131–21143 (2021).

[56] C. Majidi, "Soft robotics: a perspective—current trends and prospects for the future," Soft robotics **1**, 5–11 (2014).

[57] J.-T. Lin, C. A. Newquist, and C. K. Harnett, "Multitouch pressure sensing with soft optical time-of-flight sensors," IEEE Transactions on Instrumentation and Measurement **71**, 1–8 (2022).

[58] M. S. Han and C. K. Harnett, "Soft, all-polymer optoelectronic tactile sensor for stick-slip detection," Adv. Mater. Technol. p. 2200406 (2022).

[59] G. De Maria, C. Natale, and S. Pirozzi, "Tactile data modeling and interpretation for stable grasping and manipulation," Rob. Auton. Syst. **61**, 1008–1020 (2013).

[60] A. Cavallo, G. De Maria, C. Natale, and S. Pirozzi, "Slipping detection and avoidance based on kalman filter," Mechatronics **24**, 489–499 (2014).

[61] M. N. Saadatzi, S. K. Das, I. B. Wijayasinghe, D. O. Popa, and J. R. Baptist, "Precision grasp control with a pneumatic gripper and a novel fingertip force sensor," in "2018 IEEE 14th International Conference on Automation Science and Engineering (CASE)," (2018), pp. 1454–1459.

[62] Z. Ding, N. Paperno, K. Prakash, and A. Behal, "An adaptive Control-Based approach for 1-click gripping of novel objects using a robotic manipulator," IEEE Trans. Control Syst. Technol. **27**, 1805–1812 (2019).

[63] M. Al-Mohammed, Z. Ding, P. Liu, and A. Behal, "An adaptive control based approach for gripping novel objects with minimal grasping force," in "2018 IEEE 14th International Conference on Control and Automation (ICCA)," (2018), pp. 1040–1045.

[64] M. Stachowsky, T. Hummel, M. Moussa, and H. A. Abdullah, "A slip detection and correction strategy for precision robot grasping," IEEE/ASME Transactions on Mechatronics **21**, 2214–2226 (2016).

[65] G. De Maria, C. Natale, and S. Pirozzi, "Slipping control through tactile sensing feedback," in "2013 IEEE International Conference on Robotics and Automation," (IEEE, 2013), pp. 3523–3528.

[66] K. M. Misovec and A. M. Annaswamy, "Friction compensation using adaptive nonlinear control with persistent excitation," in "Proceedings of the 1998 American Control Conference. ACC (IEEE Cat. No.98CH36207)," , vol. 3 (1998), vol. 3, pp. 1483–1487 vol.3.

[67] B. E. Farber, "Adaptive control and parameter-dependent anti-windup compensation for inertia varying quadcopters," Ph.D. thesis, University of Louisville (2021).

[68] C. Canudas de Wit, H. Olsson, K. J. Astrom, and P. Lischinsky, "A new model for control of systems with friction," IEEE Trans. Automat. Contr. **40**, 419–425 (1995).

[69] K. Johanastrom and C. Canudas-de Wit, "Revisiting the LuGre friction model," IEEE Control Syst. Mag. **28**, 101–114 (2008).

[70] E. Lavretsky and K. A. Wise, <u>Robust and Adaptive Control</u> (Springer London).

[71] H. Khalil, <u>Nonlinear Systems</u>, Pearson Education (Prentice Hall, 2002).

[72] K. J. Zuo and J. L. Olson, "The evolution of functional hand replacement: From iron prostheses to hand transplantation," Plastic Surgery **22**, 44–51 (2014).

[73] R. Tomovic and G. Boni, "An adaptive artificial hand," IRE Transactions on Automatic Control **7**, 3–10 (1962).

[74] J. K. Salisbury and J. J. Craig, "Articulated hands: Force control and kinematic issues," The International journal of Robotics research **1**, 4–17 (1982).

[75] S. C. Jacobsen, J. E. Wood, D. Knutti, and K. B. Biggers, "The utah/mit dextrous hand: Work in progress," The International Journal of Robotics Research **3**, 21–50 (1984).

[76] J. Butterfass, G. Hirzinger, S. Knoch, and H. Liu, "Dlr's multisensory articulated hand. i. hard-and software architecture," in "Proceedings. 1998 IEEE International Conference on Robotics and Automation (Cat. No. 98CH36146)," , vol. 3 (IEEE, 1998), vol. 3, pp. 2081–2086.

[77] J. D. Crisman, C. Kanojia, and I. Zeid, "Graspar: A flexible, easily controllable robotic hand," IEEE Robotics & Automation Magazine **3**, 32–38 (1996).

[78] C. Lovchik and M. A. Diftler, "The robonaut hand: A dexterous robot hand for space," in "Proceedings 1999 IEEE international conference on robotics and automation (Cat. No. 99CH36288C)," , vol. 2 (IEEE, 1999), vol. 2, pp. 907–912.

[79] T. H. Speeter, "Primitive based control of the utah/mit dextrous hand," in "Proceedings. 1991 IEEE International Conference on Robotics and Automation," (IEEE Computer Society, 1991), pp. 866–867.

[80] D. D. Wilkinson, M. V. Weghe, and Y. Matsuoka, "An extensor mechanism for an anatomical robotic hand," in "2003 IEEE international conference on robotics and automation (Cat. No. 03CH37422)," , vol. 1 (IEEE, 2003), vol. 1, pp. 238–243.

[81] A. M. Dollar and R. D. Howe, "The highly adaptive sdm hand: Design and performance evaluation," The international journal of robotics research **29**, 585–597 (2010).

[82] A. D. Deshpande, Z. Xu, M. J. V. Weghe, B. H. Brown, J. Ko, L. Y. Chang, D. D. Wilkinson, S. M. Bidic, and Y. Matsuoka, "Mechanisms of the anatomically correct testbed hand," IEEE/ASME Transactions on mechatronics **18**, 238–250 (2011).

[83] C. Melchiorri, G. Palli, G. Berselli, and G. Vassura, "Development of the ub hand iv: Overview of design solutions and enabling technologies," IEEE Robotics & Automation Magazine **20**, 72–81 (2013).

[84] R. Deimel and O. Brock, "A novel type of compliant and underactuated robotic hand for dexterous grasping," The International Journal of Robotics Research **35**, 161–185 (2016).

[85] L. Wu, M. J. de Andrade, L. K. Saharan, R. S. Rome, R. H. Baughman, and Y. Tadesse, "Compact and low-cost humanoid hand powered by nylon artificial muscles," Bioinspiration & biomimetics **12**, 026004 (2017).

[86] Y. Li, P. Wang, R. Li, M. Tao, Z. Liu, and H. Qiao, "A survey of multifingered robotic manipulation: Biological results, structural evolvements and learning methods," Frontiers in Neurorobotics p. 53 (2022).

[87] R. J. Schwarz and C. Taylor, "The anatomy and mechanics of the human hand," Artificial limbs **2**, 22–35 (1955).

[88] J. Napier, "The evolution of the hand," Scientific American **207**, 56–65 (1962).

[89] T. J. Armstrong and D. B. Chaffin, "An investigation of the relationship between displacements of the finger and wrist joints and the extrinsic finger flexor tendons," Journal of Biomechanics **11**, 119–128 (1978).

[90] W. Spalteholz, <u>Atlas of human anatomy</u> (Butterworth-Heinemann, 2013).

[91] W. Culligan, "The big picture: gross anatomy," The Yale Journal of Biology and Medicine **86**, 285 (2013).

[92] K.-N. An, Y. Ueba, E. Chao, W. Cooney, and R. Linscheid, "Tendon excursion and moment arm of index finger muscles," Journal of biomechanics **16**, 419–425 (1983).

[93] M. U. Kurse, H. Lipson, and F. J. Valero-Cuevas, "Extrapolatable analytical functions for tendon excursions and moment arms from sparse datasets," IEEE transactions on biomedical engineering **59**, 1572–1582 (2012).

[94] F. W. Francis-Pester, R. Thomas, D. Sforzin, and D. C. Ackland, "The moment arms and leverage of the human finger muscles," Journal of Biomechanics **116**, 110180 (2021).

[95] H. R. Screen and K. E. Tanner, "Structure and biomechanics of biological composites," Wiley Encyclopedia of Composites pp. 1–12 (2011).

[96] J. D. Nguyen and H. Duong, "Anatomy, shoulder and upper limb, veins," in "StatPearls [Internet]," (StatPearls Publishing, 2021).

[97] M. Clarke, "Muscle sliding filaments," Nature Reviews Molecular Cell Biology **9**, s7–s7 (2010).

[98] L. Burbaum, J. Schneider, S. Scholze, R. T. Böttcher, W. Baumeister, P. Schwille, J. M. Plitzko, and M. Jasnin, "Molecular-scale visualization of sarcomere contraction within native cardiomyocytes," Nature Communications **12**, 4086 (2021).

[99] C. L. MacKenzie and T. Iberall, The grasping hand (Elsevier, 1994).

[100] M. R. Cutkosky and R. D. Howe, "Human grasp choice and robotic grasp analysis," Dextrous robot hands pp. 5–31 (1990).

[101] J. R. Napier, "The prehensile movements of the human hand," The Journal of bone and joint surgery. British volume **38**, 902–913 (1956).

[102] R. Ozawa and K. Tahara, "Grasp and dexterous manipulation of multi-fingered robotic hands: a review from a control view point," Advanced Robotics **31**, 1030–1050 (2017).

[103] M. Manti, T. Hassan, G. Passetti, N. D'Elia, C. Laschi, and M. Cianchetti, "A bioinspired soft robotic gripper for adaptable and effective grasping," Soft Robotics **2**, 107–116 (2015).

[104] H. Yang, G. Wei, L. Ren, Z. Qian, K. Wang, H. Xiu, and W. Liang, "A low-cost linkage-spring-tendon-integrated compliant anthropomorphic robotic hand: Mcr-hand iii," Mechanism and Machine Theory **158**, 104210 (2021).

[105] R. Konda, D. Bombara, S. Swanbeck, and J. Zhang, "Anthropomorphic twisted string-actuated soft robotic gripper with tendon-based stiffening," IEEE Transactions on Robotics (2022).

[106] Z. Xu and E. Todorov, "Design of a highly biomimetic anthropomorphic robotic hand towards artificial limb regeneration," in "2016 IEEE International Conference on Robotics and Automation (ICRA)," (IEEE, 2016), pp. 3485–3492.

[107] F. Negrello, H. S. Stuart, and M. G. Catalano, "Hands in the real world," Frontiers in Robotics and AI **6**, 147 (2020).

[108] B. Jumet, M. D. Bell, V. Sanchez, and D. J. Preston, "A data-driven review of soft robotics," Advanced Intelligent Systems **4**, 2100163 (2022).

[109] X. Chen, X. Zhang, Y. Huang, L. Cao, and J. Liu, "A review of soft manipulator research, applications, and opportunities," Journal of Field Robotics **39**, 281–311 (2022).

[110] F. E. Crossley and F. Umholtz, "Design for a three-fingered hand," Mechanism and Machine Theory **12**, 85–93 (1977).

[111] C. Loucks, V. Johnson, P. Boissiere, G. Starr, and J. Steele, "Modeling and control of the stanford/jpl hand," in "Proceedings. 1987 IEEE International Conference on Robotics and Automation," , vol. 4 (IEEE, 1987), vol. 4, pp. 573–578.

[112] Y.-T. Lee, H.-R. Choi, W.-K. Chung, and Y. Youm, "Stiffness control of a coupled tendon-driven robot hand," IEEE Control Systems Magazine **14**, 10–19 (1994).

[113] R. A. S. I. Subad, L. B. Cross, and K. Park, "Soft robotic hands and tactile sensors for underwater robotics," Applied Mechanics **2**, 356–382 (2021).

[114] S. Abondance, C. B. Teeple, and R. J. Wood, "A dexterous soft robotic hand for delicate in-hand manipulation," IEEE Robotics and Automation Letters **5**, 5502–5509 (2020).

[115] Y. She, C. Li, J. Cleary, and H.-J. Su, "Design and fabrication of a soft robotic hand with embedded actuators and sensors," Journal of Mechanisms and Robotics **7** (2015).

[116] J. Zhou, X. Chen, U. Chang, J.-T. Lu, C. C. Y. Leung, Y. Chen, Y. Hu, and Z. Wang, "A soft-robotic approach to anthropomorphic robotic hand dexterity," Ieee Access **7**, 101483–101495 (2019).

[117] K. Gilday, J. Hughes, and F. Iida, "Sensing, actuating, and interacting through passive body dynamics: A framework for soft robotic hand design," Soft Robotics **10**, 159–173 (2023).

[118] U. Kim, D. Jung, H. Jeong, J. Park, H.-M. Jung, J. Cheong, H. R. Choi, H. Do, and C. Park, "Integrated linkage-driven dexterous anthropomorphic robotic hand," Nature communications **12**, 7177 (2021).

[119] M. Laffranchi, N. Boccardo, S. Traverso, L. Lombardi, M. Canepa, A. Lince, M. Semprini, J. A. Saglia, A. Naceri, R. Sacchetti, and others IIT-INAIL Rehab Technologies Lab, "The hannes hand prosthesis replicates the key biological properties of the human hand," Science robotics **5**, eabb0467 (2020).

[120] P. Weiner, J. Starke, F. Hundhausen, J. Beil, and T. Asfour, "The kit prosthetic hand: design and control," in "2018 IEEE/RSJ International Conference on Intelligent Robots and Systems (IROS)," (IEEE, 2018), pp. 3328–3334.

[121] J. Vertongen, D. G. Kamper, G. Smit, and H. Vallery, "Mechanical aspects of robot hands, active hand orthoses, and prostheses: A comparative review," IEEE/ASME Transactions on Mechatronics **26**, 955–965 (2020).

[122] G. Gu, N. Zhang, H. Xu, S. Lin, Y. Yu, G. Chai, L. Ge, H. Yang, Q. Shao, X. Sheng et al., "A soft neuroprosthetic hand providing simultaneous myoelectric control and tactile feedback," Nature biomedical engineering **7**, 589–598 (2023).

[123] A. Mohammadi, J. Lavranos, H. Zhou, R. Mutlu, G. Alici, Y. Tan, P. Choong, and D. Oetomo, "A practical 3d-printed soft robotic prosthetic hand with multi-articulating capabilities," PloS one **15**, e0232766 (2020).

[124] S. Puhlmann, J. Harris, and O. Brock, "Rbo hand 3: A platform for soft dexterous manipulation," IEEE Transactions on Robotics **38**, 3434–3449 (2022).

[125] Y. Yang, Y. Chen, Y. Li, M. Z. Chen, and Y. Wei, "Bioinspired robotic fingers based on pneumatic actuator and 3d printing of smart material," Soft robotics **4**, 147–162 (2017).

[126] H. Zhao, K. O'brien, S. Li, and R. F. Shepherd, "Optoelectronically innervated soft prosthetic hand via stretchable optical waveguides," Science robotics **1**, eaai7529 (2016).

[127] H. Lee, J. Park, B. B. Kang, and K.-J. Cho, "Single-step 3d printing of bio-inspired printable joints applied to a prosthetic hand," 3D Printing and Additive Manufacturing **10**, 917–929 (2023).

[128] J. Hughes, P. Maiolino, and F. Iida, "An anthropomorphic soft skeleton hand exploiting conditional models for piano playing," Science Robotics **3**, eaau3098 (2018).

[129] J. Zhang, J. Sheng, C. T. O'Neill, C. J. Walsh, R. J. Wood, J.-H. Ryu, J. P. Desai, and M. C. Yip, "Robotic artificial muscles: Current progress and future perspectives," IEEE transactions on robotics **35**, 761–781 (2019).

[130] X. Zhou, Y. Zhu, S. Qian, H. Ge, S. Cai, and G. Bao, "Design of full-drive multi-finger dexterous hand," in "2022 International Conference on Advanced Robotics and Mechatronics (ICARM)," (IEEE, 2022), pp. 51–56.

[131] H. Yin, L. Tian, and G. Yang, "Design of fibre array muscle for soft finger with variable stiffness based on nylon and shape memory alloy," Advanced Robotics **34**, 599–609 (2020).

[132] I. H. Kim, S. Choi, J. Lee, J. Jung, J. Yeo, J. T. Kim, S. Ryu, S.-k. Ahn, J. Kang, P. Poulin et al., "Human-muscle-inspired single fibre actuator with reversible percolation," Nature Nanotechnology **17**, 1198–1205 (2022).

[133] A. Kotikian, J. M. Morales, A. Lu, J. Mueller, Z. S. Davidson, J. W. Boley, and J. A. Lewis, "Innervated, self-sensing liquid crystal elastomer actuators with closed loop control," Advanced Materials **33**, 2101814 (2021).

[134] A. Nilles, S. Ceron, N. Napp, and K. Petersen, "Strain-based consensus in soft, inflatable robots," in "2022 IEEE 5th International Conference on Soft Robotics (RoboSoft)," (IEEE, 2022), pp. 789–794.

[135] S. Jacobsen, E. Iversen, D. Knutti, R. Johnson, and K. Biggers, "Design of the utah/mit dextrous hand," in "Proceedings. 1986 IEEE International Conference on Robotics and Automation," , vol. 3 (IEEE, 1986), vol. 3, pp. 1520–1532.

[136] M. G. Catalano, G. Grioli, E. Farnioli, A. Serio, C. Piazza, and A. Bicchi, "Adaptive synergies for the design and control of the pisa/iit softhand," The International Journal of Robotics Research **33**, 768–782 (2014).

[137] T. Laliberte, L. Birglen, and C. Gosselin, "Underactuation in robotic grasping hands," Machine Intelligence & Robotic Control **4**, 1–11 (2002).

[138] N. Z. Azlan and H. Yamaura, "Anthropomorphic finger with optimized geometric parameters for pinching and grasping tasks," Mechanism and machine theory **49**, 52–66 (2012).

[139] D. Yoon and Y. Choi, "Underactuated finger mechanism using contractible slider-cranks and stackable four-bar linkages," IEEE/ASME Transactions on Mechatronics **22**, 2046–2057 (2017).

[140] X.-L. Li, L.-C. Wu, and T.-Y. Lan, "A 3d-printed robot hand with three linkage-driven underactuated fingers," International Journal of Automation and Computing **15**, 593–602 (2018).

[141] S. R. Kashef, S. Amini, and A. Akbarzadeh, "Robotic hand: A review on linkage-driven finger mechanisms of prosthetic hands and evaluation of the performance criteria," Mechanism and Machine Theory **145**, 103677 (2020).

[142] W.-Y. Li, H. Nabae, G. Endo, and K. Suzumori, "New soft robot hand configuration with combined biotensegrity and thin artificial muscle," IEEE Robotics and Automation Letters **5**, 4345–4351 (2020).

[143] H.-I. Kim, M.-W. Han, S.-H. Song, and S.-H. Ahn, "Soft morphing hand driven by sma tendon wire," Composites Part B: Engineering **105**, 138–148 (2016).

[144] J. Li, M. Sun, Z. Wu, and H. Yin, "Design, analysis, and grasping experiments of a novel soft hand: hybrid actuator using shape memory alloy actuators, motors, and electromagnets," Soft Robotics **7**, 396–407 (2020).

[145] M. Liu, L. Hao, W. Zhang, and Z. Zhao, "A novel design of shape-memory alloy-based soft robotic gripper with variable stiffness," International journal of advanced robotic systems **17**, 1729881420907813 (2020).

[146] M. T. Mason and J. K. Salisbury Jr, "Robot hands and the mechanics of manipulation," (1985).

[147] Z. Li, P. Hsu, and S. Sastry, "Grasping and coordinated manipulation by a multifingered robot hand," The International Journal of Robotics Research **8**, 33–50 (1989).

[148] M. Ciocarlie and P. Allen, "Data-driven optimization for underactuated robotic hands," in "2010 IEEE International Conference on Robotics and Automation," (IEEE, 2010), pp. 1292–1299.

[149] J. Bohg, A. Morales, T. Asfour, and D. Kragic, "Data-driven grasp synthesis—a survey," IEEE Transactions on robotics **30**, 289–309 (2013).

[150] C. Armanini, F. Boyer, A. T. Mathew, C. Duriez, and F. Renda, "Soft robots modeling: A structured overview," IEEE Transactions on Robotics (2023).

[151] A. Billard and D. Kragic, "Trends and challenges in robot manipulation," Science **364**, eaat8414 (2019).

[152] C. Della Santina, V. Arapi, G. Averta, F. Damiani, G. Fiore, A. Settimi, M. G. Catalano, D. Bacciu, A. Bicchi, and M. Bianchi, "Learning from humans how to grasp: a data-driven architecture for autonomous grasping with anthropomorphic soft hands," IEEE Robotics and Automation Letters **4**, 1533–1540 (2019).

[153] Q. Liu, J. Zhang, X. Li, J. Zhou, X. Hu, W. Jin, and A. Song, "A rigid and flexible structures coupled underactuated hand," in "2022 IEEE/ASME International Conference on Advanced Intelligent Mechatronics (AIM)," (IEEE, 2022), pp. 1587–1592.

[154] N. Zhang, L. Ge, H. Xu, X. Zhu, and G. Gu, "3d printed, modularized rigid-flexible integrated soft finger actuators for anthropomorphic hands," Sensors and Actuators A: Physical **312**, 112090 (2020).

[155] N. Zhang, Y. Zhao, G. Gu, and X. Zhu, "Synergistic control of soft robotic hands for human-like grasp postures," Science China Technological Sciences **65**, 553–568 (2022).

[156] M. Gabiccini, A. Bicchi, D. Prattichizzo, and M. Malvezzi, "On the role of hand synergies in the optimal choice of grasping forces," Autonomous Robots **31**, 235–252 (2011).

[157] R. M. Murray, Z. Li, S. S. Sastry, and S. S. Sastry, <u>A mathematical introduction to robotic manipulation</u> (CRC press, 1994).

[158] J. Yi, B.-c. Kim, K.-J. Cho, and Y.-L. Park, "Underactuated robotic gripper with fiber-optic force sensing tendons," IEEE Robotics and Automation Letters (2023).

[159] T. L. T. Lun, K. Wang, J. D. Ho, K.-H. Lee, K. Y. Sze, and K.-W. Kwok, "Real-time surface shape sensing for soft and flexible structures using fiber bragg gratings," IEEE Robotics and Automation Letters **4**, 1454–1461 (2019).

[160] R. M. Murray, Z. Li, and S. S. Sastry, <u>A mathematical introduction to robotic manipulation</u> (CRC press, 2017).

[161] C. R. Pollock, <u>Fundamentals of optoelectronics</u> (Irwin, 1995).

[162] C. K. Harnett, H. Zhao, and R. F. Shepherd, "Stretchable optical fibers: Threads for strain-sensitive textiles," Advanced Materials Technologies **2**, 1700087 (2017).

[163] H. G. Pfeiffer and H. A. Liebhafsky, "The origins of beer's law," Journal of Chemical Education **28**, 123 (1951).

[164] D. M. Haid, O. Duncan, J. Hart, and L. Foster, "Characterisation of thermoplastic polyurethane (tpu) for additive manufacturing," .

APPENDIX A: DYNAMICS OF FINGER MANIPULATOR

In Chapter 4, the equation of motion for the finger manipulator is used. The derivation is described in this Appendix based on the kinematics formulation and the Lagrangian [157]. When a general open-chain manipulator is considered with joint angles $\theta \in \mathbb{R}^n$, the Lagrangian is formulated

$$L(\theta, \dot{\theta}) = \frac{1}{2}\dot{\theta}^T M(\theta)\dot{\theta} - V(\theta) \tag{36}$$

where the matrix $M(\theta) \in \mathbb{R}^{n \times n}$ is the manipulator inertia matrix and the total potential energy is $V(\theta) = \sum_{i=1}^{n} m_i g h_i$ with the mass of the ith link and gravitational constant g. In the meantime, the kinetic energy term can be rewritten as the sum of ith link's kinetic energy,

$$\frac{1}{2}\dot{\theta}^T M(\theta)\dot{\theta} = \sum_{i=1}^{n} T_i(\theta, \dot{\theta}) \tag{37}$$

where

$$\begin{aligned} T_i(\theta, \dot{\theta}) &= \frac{1}{2}(V_i^b)^T \bar{M}_i V_i^b \\ &= \frac{1}{2}\dot{\theta}^T J_i^{bT}(\theta)\bar{M}_i J_i^b(\theta)\dot{\theta}. \end{aligned} \tag{38}$$

$\bar{M}_i$ is the generalized inertia matrix of the ith link and the body velocity of the center of mass is given by $V_i^b = J_i^b(\theta)\dot{\theta}$, which is relative to the base frame of the manipulator. Also, the body Jacobian of the ith link can be described based on the finger kinematics as below

$$J_i^b(\theta) = [\xi_1^\dagger \cdots \xi_i^\dagger \quad 0 \cdots 0], \tag{39}$$

where

$$\xi_j^\dagger = Ad^{-1}_{(e^{\hat{\xi}_j \theta_j} \cdots e^{\hat{\xi}_i \theta_i} g_i(0))}\xi_j \quad j \leq i \tag{40}$$

when the transformation matrix of the ith link from the base frame is $g_i(\theta) = e^{\hat{\xi}_1 \theta_1} \cdots e^{\hat{\xi}_i \theta_i} g_i(0)$. Then we can fully describe the Lagrangian of the manipulator. Now we can derive the system equation of motion given by substituting into Lagrange's equations,

$$\frac{d}{dt}\frac{\partial L}{\partial \dot{\theta}_i} - \frac{\partial L}{\partial \theta_i} = \Upsilon_i, \tag{41}$$

where Υ_i represents the applied torque with other generalized forces on the ith joint. Based on equations 36 and 38, we can have

$$\sum_{j=1}^{n}(M_{ij}\ddot{\theta}_j + \dot{M}_{ij}\dot{\theta}_j) - (\frac{1}{2}\sum_{j,k=1}^{n}\frac{\partial M_{kj}}{\partial \theta_i}\dot{\theta}_k\dot{\theta}_j - \frac{\partial V}{\partial \theta_i}) = \Upsilon_i \quad i = 1, \cdots, n \tag{42}$$

107

where M_{ij} is the element in the manipulator inertia matrix $M(\theta)$. Eventually, the equation 42 can be rearranged as the form that we are familiar

$$M(\theta)\ddot{\theta} + C(\theta, \dot{\theta})\dot{\theta} + N(\theta, \dot{\theta}) = \tau \tag{43}$$

where

$$M_i(\theta) = \sum_{j=1}^{n} M_{ij}$$

$$C_{ij}(\theta, \dot{\theta}) = \frac{1}{2} \sum_{k=1}^{n} \left(\frac{\partial M_{ij}}{\partial \theta_k} + \frac{\partial M_{ik}}{\partial \theta_j} - \frac{\partial M_{kj}}{\partial \theta_i} \right) \dot{\theta}_k \tag{44}$$

$$N_i(\theta, \dot{\theta}) = \frac{\partial V}{\partial \theta_i}(\theta).$$

The equation 43 and 44represents the finger manipulator dynamics with respect to the joint configuration. Like Figure 25, when it is considered to manipulate an object we can derive the new system dynamics by combining finger manipulator and object dynamics. Since we already explained the equation of motion, to avoid confusion the notation for the finger manipulator dynamics is able to be slightly changed.

$$M_f(\theta)\ddot{\theta} + C_f(\theta, \dot{\theta})\dot{\theta} + N_f(\theta, \dot{\theta}) = \tau \tag{45}$$

Also, the equation of motion for the object is given by

$$M_o(x)\ddot{x} + C_o(x, \dot{x})\dot{x} + N_o(x, \dot{x}) = 0. \tag{46}$$

In the meantime, the finger and object can be connected by the constraint like equation 24 in Chapter 4. Then, we can rewrite the overall system dynamics through the Lagrange-d'Alembert equation. When the composite system configuration is $q = (\theta, x)$, the new Lagrangian is described by

$$L = \frac{1}{2}\dot{\theta}^T M_f \dot{\theta} + \frac{1}{2}\dot{x} M_o \dot{x} - V_f(\theta) - V_o(x). \tag{47}$$

The velocity constraint in equation 24 can also derive a constraint on the virtual displacement such as $\partial\theta = J^{-1}G^T\partial x$. Based on this, thus, the Lagrange-d'Alembert equation can be written as below

$$\left(\frac{d}{dt}\frac{\partial L}{\partial \dot{q}} - \frac{\partial L}{\partial q} - \begin{bmatrix} \tau \\ 0 \end{bmatrix} \right) \cdot \partial q = GJ^{-T}\left(\frac{d}{dt}\frac{\partial L}{\partial \dot{\theta}} - \frac{\partial L}{\partial \theta} - \tau \right) \cdot \partial x + \left(\frac{d}{dt}\frac{\partial L}{\partial \dot{x}} - \frac{\partial L}{\partial x} \cdot \partial x \right) \tag{48}$$

$$\left(\frac{d}{dt}\frac{\partial L}{\partial \dot{x}} - \frac{\partial L}{\partial x} \right) + GJ^{-T}\left(\frac{d}{dt}\frac{\partial L}{\partial \dot{\theta}} - \frac{\partial L}{\partial \theta} \right) = GJ^{-T}\tau. \tag{49}$$

Eliminating $\dot{\theta}$ and $\ddot{\theta}$ through the velocity constraint, the overall system equation of motion become like equation 25 where

$$
\begin{aligned}
\tilde{M} &= M_o + GJ^{-T}M_f J^{-1}G^T \\
\tilde{C} &= C_o + GJ^{-T}\left(C_f J^{-1}G^T + M_f \frac{d}{dt}(J^{-1}G^T)\right) \\
\tilde{N} &= N_o + GJ^{-T}N_f \\
F &= GJ^{-T}\tau
\end{aligned}
\tag{50}
$$

CURRICULUM VITAE

Seokyoung Han

Education

Ph.D., University of Louisville, Louisville, KY, USA, 2024

M.S., Gwangju Institute of Science and Technology(GIST), Gwangju, Korea, 2015

B.S., Kookmin University, Seoul, Korea, 2013

Publications

Michael S. Han, Cindy K. Harnett, "Journey from Human Hands to Robot Hands : Biological Inspiration of Anthropomorphic Robotic Manipulators", Bioinspiration & Biomimetics, 2024

Michael S. Han, Cindy K. Harnett, "Soft, All-Polymer Optoelectronic Tactile Sensor for Stick-Slip Detection", Advanced Materials Technologies, 2022

Michael S. Han, J-T. Lin, Cindy K. Harnett, "A Bio-Inspired Robotic Finger Driven and Shape-Sensed by Soft Optical Tendons", RoboSoft IEEE, 2024, San Diego

Michael S. Han, Dan O. Popa, Cindy K. Harnett, "Anti-Slipping Adaptive Grasping Control with a Novel Optoelectronic Soft Sensor", RoboSoft IEEE, 2023, Singapore

Seokyoung Han, "Development of a Tensegrity Robot and Feedforward Control via Iterative Learning Algorithm", Master's Thesis, 2015

Seokyoung Han, K. Jeong, H. Ahn, "Iterative Learning Control for Trajectory Tracking of Tensegrity Robot", Control Automation Robotics & Vision on IEEE, 2014